HUNGARIAN GROUP OF *fib*

# CONCRETE STRUCTURES

ANNUAL TECHNICAL JOURNAL



2026

Vol. 27

HYDRA STAT

STRUCTURAL ENGINEERING DESIGN

# PRECISE DESIGN.
## RELIABLE FOUNDATIONS.
## LASTING VALUE.

NAGYERDEI STADIUM, DEBRECEN

DEBRECEN PUBLIC BATH

HUNGEXPO CONFERENCIA CENTER

MOL CAMPUS, BUDAPEST

## ENGINEERING SOLUTIONS THAT BUILD THE FUTURE.

- EXPERTISE
- BUILDINGS
- INDUSTRIAL STRUCTURES
- 3D MODELING & CALCULATIONS

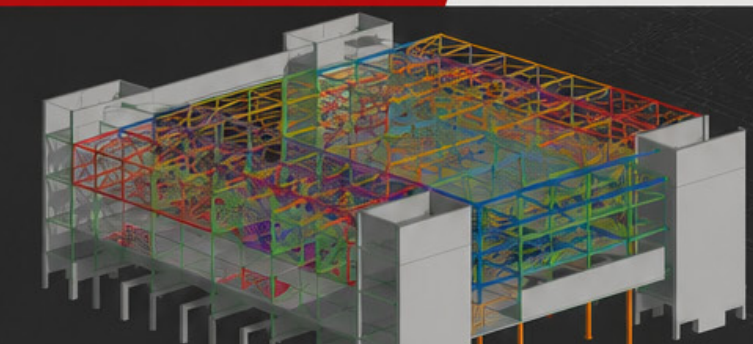

WWW.HYDRASTAT.HU

**CONCRETE STRUCTURES**
Journal of the Hungarian Group of ***fib***



Founded by: Hungarian Group of ***fib***
Publisher: Hungarian Group of ***fib***
(***fib*** = International Federation for Structural Concrete)

**Editorial office:**
Budapest University of Technology and Economics (BME)
Department of Construction Materials and Technoligies
Műegyetem rkp. 3., H-1111 Budapest
Phone: +36-1-463 4068
Fax: +36-1-463 3450
WEB http://www.fib.bme.hu
WEB editor: András Bíró

Layout and print: Csaba Halmai, Navigar Ltd.

Printed in 100 copies and web.


HU ISSN 2062-7904
online ISSN: 1586-0361

Cover photo:

1500 m$^3$ storage capacity
Water Tower,
Bük, Hungary

# CONTENT



Sponsors:

Railway Bridges Foundation, ÉMI Nonprofit Ltd., HÍDÉPÍTŐ Co., Holcim Hungary Co., MÁV Co., MSC Consulting Co., Lábatlani Vasbetonipari Co., Pont-*TERV* Co., UVATERV Co., MÉLYÉPTERV KOMPLEX Engineering Co., SW Umwelttechnik Hungary Ltd., Betonmix Consulting Ltd., BVM Épelem Ltd., CAEC Ltd., Pannon Freyssinet Ltd., STABIL PLAN Ltd., BME Dept. of Structural Engineering, BME Dept. of Construction Materials and Technologies

# PREFABRICATED WATER TOWERS WITH PRESTRESSED MAST OF INCREASED STORAGE CAPACITY



Béla Csíki – Bence Kólya – Gábor Szilágyi

https://doi.org/10.32970/CS.2026.1.1

*Several almost fully prefabricated reinforced concrete water towers to storage capacities of 100 to 500 m³ have been built in the past decade, in Hungary. The increasing residential and industrial water demands in some areas have made necessary to build water towers with higher storage capacities. The paper summarizes mainly the design aspects of developing the prefabricated type towers up to 1000-1500 m³ storage capacity. Two recently commissioned water towers in the country, each with a storage capacity of 1,500 m³ are also presented. The prefabricated type water towers have proved to be economic and market-competitive due to the short time of in-situ building works and also to the (for long time) existing high quality prefabrication capacity.*

**Keywords:** water tower, prefabrication, prestressing, post tensioning, mast, tank, foundation cone.

## 1. INTRODUCTION

Several examples can be found for reinforced concrete water towers built by using prefabricated elements. In most cases, the prefabrication extends only to the tank, or its shuttering. The prefab elements are usually assembled on the land-surface before lifting up to the final position (Koperniczky, 1969; Kiss and Tóth, 1973). Until recently there were much fewer instances for prefabrication extending also to the mast of the water tower. The set of uniform 200 m³ water towers of such a kind in Italy is often referred to (Márkus, 1984).

The prefabrication capacity of reinforced concrete wall elements to water-reservoirs, and also of circular pipe elements for underground conduits exists for long time in Hungary. Possibility of using together the prefab pipe- and wall elements in order to shape the superstructure (the mast and the tank) of a water tower was raised by AGM Beton Co., the manufacturer of such elements itself (Szilágyi, 2022). The company is playing an increasing role in the civil engineering execution market in Hungary and abroad (https://www.agmbeton.hu).

Based on the manufacturer's building concept the first prefabricated water towers with prestressed mast composed of prefab pipe elements were constructed in Hungary during the 2010s for relatively lower (100-500 m³) storage capacities (Csíki, et al., 2017; Csíki and Kőszeghy, 2019).

Besides, the steadily increasing residential and industrial water demand in some regions has made it necessary to further develop the prefabricated type towers up to storage capacity of 1000-1500 m³. As a result two water towers were designed and also commissioned in the past few years, first in Komárom and an other in Bük, each with storage capacity of 1500 m³. The design process of the third high-capacity tower of 1000 m³ storage capacity to Paks is completed, and the construction is expected to start in the near future.

The detailed structural design of the higher-capacity water towers was carried out by E&H Ltd. (https://www.eundh.hu). As part of the development, standard structural designs to be adopted for 1000 m³ and 1500 m³ water tower types were prepared by DCB Ltd.

## 2. STRUCTURAL ARRENGEMENT OF THE WATER TOWERS

### 2.1 In general

The basic structural arrangement of the more recent 1000-1500 m³ capacity prefabricated reinforced concrete water towers is essentially similar to that of the smaller towers with storage capacities of 200–500 m³ (Csíki, et al., 2017, Csíki and Kőszeghy, 2019). The main differences are reflected in the structural dimensions and geometrical measures.

The mast of the larger capacity water towers is also made of vertically post-tensioned prefabricated reinforced concrete pipe elements. The storage tanks above the mast are fully prefabricated with watertight connections, as well. The vertical section of a 1500 m³ storage capacity water tower is presented in *Fig. 1*.

The only main structural part of the building made of in-situ reinforced concrete is the founding of the water towers.

### 2.2 Substructure and foundation

The substructure of the towers consists of a foundation slab and of a founding cone made of in-situ (monolithic) reinforced concrete.

Depending on the soil conditions of the site plane- or piled foundation may be applied. The foundation method determines the necessary layout measure of the applied (circular or polygonal) foundation slab. The two latest water towers of

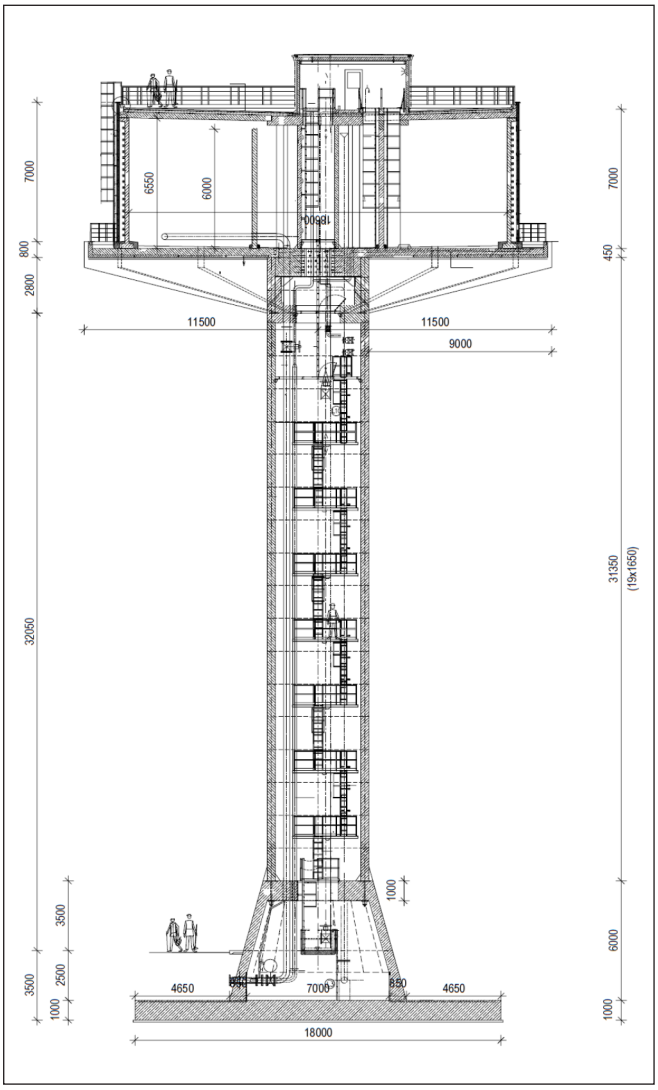


**Fig. 1:** Vertical section of a water tower of 1500 m³ storage capacity

1500 m³ were built on a flat (polygonal) slab foundation with an inner diameter of 18.0 m and a thickness of 1.0 m.

The founding cone stiffening the substructure on the one hand secures the entrance of the tower, on the other hand serves as anchoring space for the prestressing bars of the mast. The height of the cone is 6.00 m, the outer diameter is changing from 5.40 m to 8.70 m. The thickness of the roof slab of the cone where the mast prestressing bars are fixed to is 1.00 m.

The applied grade of structural concrete for the substructure is C35/45-XC4-XF1-XA1, with a reinforcing steel category of B500B.

## 2.3 Prestressed mast

The mast consists of prefabricated reinforced concrete pipe elements of 5.0 m outer diameter and of 400 mm wall thickness. The height of the pipe rings is 1.65 m. The number of the mast elements can be about 15 to 19 pieces depending on the required tower height. The last element is special to allow for anchoring radial cantilever beams directly supporting the tank.

The mast elements are gradually post-tensioned in two steps through the pipe-walls in vertical direction by prestressing bars anchored at the bottom of the thick roof of the founding cone. In the realized cases Dywidag prestressing bars (DSI 950/1050) of 40 mm diameter were used.

The applied grade of structural concrete for the mast elements is C50/60-XC4-XF1, with reinforcing bars of B500B.

## 2.4 Tank supporting

The direct supporting of the large diameter tank at the top of the slender mast requires special structural engineering solutions, as well.

Radially located, reinforced concrete cantilever beams are used for supporting the tank. The bottom plate of the tank is made of in-situ reinforced concrete casting on prefabricated shallow shutter slabs after they have been lifted up on the cantilevers. Fixing and anchoring of the radial prefabricated cantilevers to the specially arranged, final mast element has been one of the most challenging questions to be solved during the design (*Fig. 2*).

## 2.5 Tank

The storage space in the tank is divided into two parts by an internal cylindrical wall constructed from prefabricated segments. The outer tank-wall is polygonal in layout, and consists of vertical plain prefabricated reinforced concrete panels with watertight connections, *Fig.3*.

In the center of the tank there is a circular pipe-element with a steel ladder inside to connect the mast area with the tank-roof to secure free access. This central pipe acts as an inner support of the tank-roof, as well.

**Fig. 3:** Tank structural arrangement (without roof)

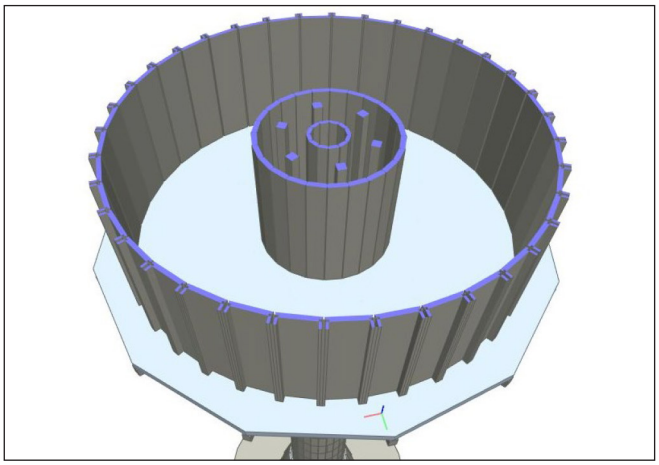

**Fig. 2:** Cantilevers and anchoring to the final mast element and reinforcement of bottom plate

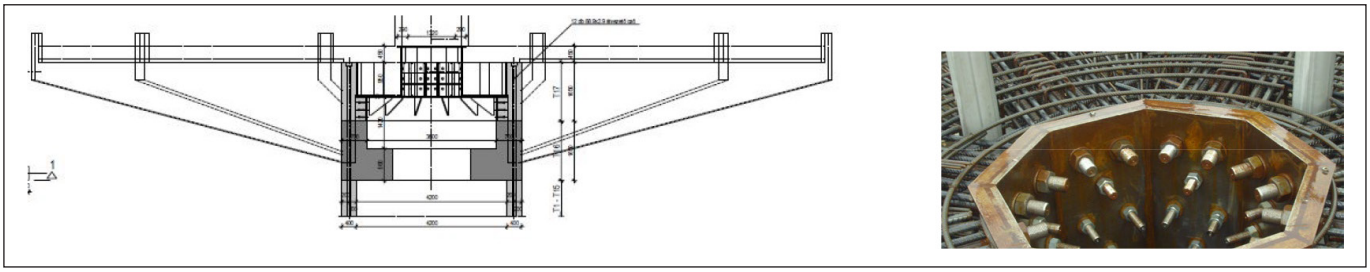

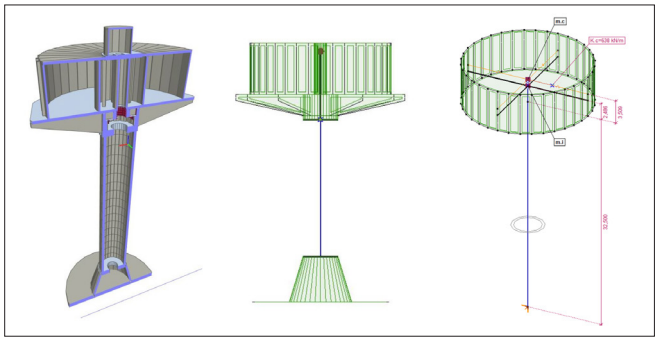

**Fig. 4:** FEM model of structure, and static and dynamic models to earthquake load

The outer polygonal tank-wall consists of prefabricated vertical plain panels with horizontal and vertical stiffening ribs at the panel-edges. The panels are connected to each other by bolts along the vertical ribs, while their bottom is welded to steel continuous profiles concreted in the bottom plate. The water-tightness at each junction is secured by cement-slurry injection of the designed gaps.

Regarding a 1500 m$^3$ storage capacity tank, 36 wall-panels of ca. 1.65 m width are used, arranged around a 18.60 m diameter inner circle of the 36 sides polygon. The height of the panels is 6.55 m, with lowest thickness of 200 mm. Tanks of similar arrangement with several measures have been widely used to build underground water reservoirs (Szilágyi, 2022).

The grade of structural concrete to the prefab elements of the water tanks is C40/50-XV2(H)-XC2-XD2. The category of the applied reinforcing steel is B500B.

### 2.6 Mast and tank element joints

The circular horizontal joints of the mast elements are formed by smooth surfaces (without any notches) compacted by sticking and – obviously – by the prestressing itself.

The watertight joints of tank elements at the bottom slab are formed by mixing of in-situ welding and concreting. The vertical joints along the wall elements are bolted and in-situ cement injected, forming so-called Aqua Seal connections (Szilágyi, 2022).

## 3. STRUCTURAL ANALYSIS METHODS

The following structural models, design principles and analysis methods were applied to the structural design of the water towers (Fig. 4.):

- *In general:*
  Three-dimensional combined structural model on elastic bedding or on discrete elastic springs examined by FEM.
- *To earthquake load* (Modal response spectrum analysis):
  1. Static model: Reduced at the mass centre (one mass) vertical cantilever. The water load (weight) is considered in the metacentre when determining the mass centre.
  2. Dynamic model: Two mass (M1, M2) vertical cantilever. M1 is the sum of the mass of the impulsive water part (moving together with the structure) acting in the mass centre. M2 is the mass of convective water part (moving separately from the structure) suspended in the metacentre.
- *To stability analysis:*
  Elastically supported (walled in) vertical cantilever. (The critical force based on *Föppl-Papkovics* principle.)
- *Prestressing of the mast:*
  The effective (applied in two steps) prestressing forces of the mast are increasing from top to bottom to eliminate tension stresses along the mast.

## 4. CONSTRUCTION AND FEASIBILITY

Two water towers with storage capacity of 1500 m$^3$ were built and put in operation recently, one in Komárom in 2023, and an other in Bük in 2025. The Komárom water tower during the mounting-like construction is shown in *Fig. 5*.

The prefabrication of the elements and the leading of the in situ construction works for the new towers were done by AGM Beton Co. (H-2200 Monor, Külterület, Hrsz.: 0100/8, Hungary), acting as general contractor of the projects.

The prefabricated type water towers have proved to be economic and market-competitive due to the short time of in-situ mounting-like building works and also to the (for long time) existing high quality prefabrication capacity.

## 5. CONCLUSIONS

The increasing residential and industrial water demands in some areas have made necessary to build water towers with higher storage capacities. The paper summarizes primarily the design aspects of developing the existing lower capacity prefabricated tower types up to 1000-1500 m$^3$ storage capacity.

The mast of the larger water towers is also made of vertically post-tensioned prefabricated reinforced concrete pipe elements. The storage tanks above the mast are fully prefabricated with watertight connections. The tank-wall of the water towers is polygonal in layout and consists of vertical plain panels. The only main structural parts made of in-situ reinforced concrete are the foundation and founding of the water-towers.

Two water towers of 1500 m$^3$ storage capacity were built and put in operation recently, one in Komárom in 2023, and an other in Bük in 2025. The experiences with the special civil engineering structures (*Fig. 6*) have been positive so far regarding the aspects of design, building and operation, respectively. Moreover, the new water towers as special kind of landmarks satisfy the aesthetic considerations, as well.

## 6. ACKNOWLEDGEMENTS

Thanks must be expressed to AGM Beton Co. (H-2200 Monor, Külterület, Hrsz.: 0100/8, Hungary), the general contractor of the towers for the possibility of taking part in the development. Also thanks for contribution of its employees, and also of Károly Kőszeghy to the detailing of the structural and architectural design.

Project no. 2020-1.1.2-PIACI-KFI-2021-00268 has been implemented with the support provided by the Ministry of Culture and Innovation of Hungary from the National Research, Development and Innovation Fund, financed under the 2020-1.1.2-PIACI KFI funding scheme.


## 7. REFERENCES

Csíki, B., Kőszeghy, K., Perczel, Z. (2017) "New type prefabricated water towers with prestressed mast", *Proceedings of CCC 2017*, Tokaj, Hungary, September 2017, pp. 15-22.

**Fig. 5:** The 1500 m³ water tower in Komárom during construction


Csíki, B., Kőszeghy, K. (2019) "Prefab water towers for lower storage capacities", J. *Concrete Structures*, 2019, pp. 14-19.

Kiss, G., Tóth, L. (1973), "Water tower of Balaton Youth-town", *Műszaki Tervezés,* March 1973, pp. 27-29. (in Hungarian)

Koperniczky, J. (1969), "Construction of small water towers", *Műszaki Tervezés*, March 1969, pp. 19-22. (in Hungarian)

Márkus, G. (1984), "Reinforced concrete reservoirs", *Mérnöki Kézikönyv, II.*, 1984, pp. 920-942. (in Hungarian)

Szilágyi, G. (2022), "Building of reinforced concrete water towers and reservoirs from precast elements", *MMK*, (in Hungarian), June 2022.
https://www.agmbeton.hu/kivitelezés/víztornyok



**Dr. Béla CSÍKI** (1957), MSc (1982), Doctorate (1993), Civil Eng., TU Budapest. MSc Real Estate (2002), NTU Nottingham. Employments: DCB Engineering Ltd., managing director (2003- ), E&H Ltd., technical director (2016- ). He is a member of the editorial board. His main field of interest is dealing with specific structural problems of and also the design of special civil engineering structures mainly in connection with water and waste water treatment or industrial fields. He has been author of several papers on his professional activity.

**Bence KÓLYA** (1977), MSc (2003), Civil Eng., TU Budapest. Employments: Hídépítő Co., CÉH Co., E&H Ltd (2014-). His professional work covers mainly the structural design of bridges, industrial and specific buildings. He participated in the design of several highway bridge made of prestressed concrete in Hungary. His main interest is the FEM analysis of complex civil engineering structures.

**Gábor Szilágyi** (1943), MSc (1967), Mechanical Engineer, Budapest University of Technology and Economics, Faculty of Fluid Mechanics (TU Budapest). Postgraduate Specialist Engineer in Water Supply, Sewerage and Sanitary Engineering (1973). He worked for Budapest Waterworks (Fővárosi Vízművek), (1967–1997), as Head of the Northern Water Supply Operations Unit (1971), than as Director of the ROCLA Pipe Factory (1973–1997), Presently he is Chief Executive Officer of AGM Beton Plc. (1997–).
Fields of activity: water supply, sewerage systems, and wastewater treatment. Within these fields: manufacturing, development, and construction of reinforced concrete pipes and prefabricated reinforced concrete structures; development and implementation of water abstraction technologies (21 registered patents).


**Fig. 6:** Views of the recently built water towers of 1500 m³ storage capacity (Komárom left, Bük right)

# PÁL TOMORI DANUBE BRIDGE AT KALOCSA AND PAKS – DESIGN OF THE MAIN RIVER BRIDGE



Dr. Sándor Kisbán - Pál Pusztai - Rudolf Kiss

https://doi.org/10.32970/CS.2026.1.2

*The new Tomori Pál Bridge, located in the vicinity of Kalocsa and Paks, the 20th bridge on the Hungarian section of the Danube, was opened to traffic in June 2024. The construction work on the bridge was carried out by Duna Aszfalt Zrt. The bridge design tasks were undertaken by CÉH zRt., as the lead designer of the bridge, and Pont-TERV Zrt.*

*In this article, we describe the design process and experiences gained during construction of the extradosed river bridge spanning the Danube, which is part of a structure comprising three bridges with a total length of 946 m.*

*In this article, we present the main load-bearing structural elements of the river bridge. The descriptions detail the design conditions that influenced the configuration of the structural elements.*

**Keywords:** extradosed structure, trapezoidal sheet, hybrid cross-section, cable element, construction methodology, tensioning (cable systems)

## 1. BACKGROUND

In January 2020, NIF Zrt. (National Infrastructure Development Company) launched a public procurement procedure for the design and construction of the new Danube bridge at Kalocsa-Paks and the adjoining road network. Duna Aszfalt Zrt. was selected as the winner of the public procurement procedure, and construction work commenced in January 2021. The design was carried out by a consortium comprising CÉH zRt. and UTIBER Kft., the main designer was CÉH zRt.

The design task consisted of two parts (Figure 1): one was the design of the new secondary main road No. 512 between main road No. 51 and the M6 motorway, of which the new Danube bridge forms a part, and the design of the new north-south link road No. 5124 between Paks and Gerjen.

**Fig 1:** General site plan

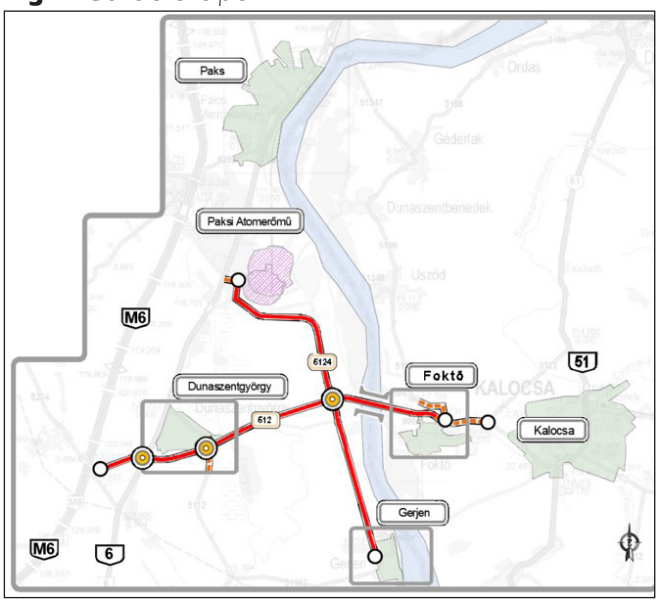


## 2. GENERAL DESCRIPTION OF THE STRUCTURES

The new Danube bridge is a single structure comprising various components. Structurally, it consists of three bridges: the left-bank floodplain bridge, the river bridge and the right-bank floodplain bridge.

On the bridge, aligned with the cross-section of Main Road No. 512, two traffic lanes have been provided, with two-way cycle paths on both outer sides of the bridge. The total length of the nine-span bridge is 946 m; we provided a 180 m wide navigation channel in the central span of the river bridge, resulting in a maximum span of 200 m. (Figure 2)

The 440 m long river bridge is a three-span, extradosed bridge with a hybrid cross-section, featuring a two-cell box girder parabolically haunched above the river piers, with spans of 119.0+200.0+119.0 m (Figure 3). The main girder of the bridge is a dual cell box structure, the inclined outer webs and the central web are formed by trapezoidal steel sheets. The bottom slab and the cantilevered deck slab of the box section are made of reinforced concrete.

The superstructure was designed with reinforced concrete deck and bottom slabs prestressed with longitudinal post-tensioning cables to meet construction and permanent load requirements. To meet the design criteria due to live loads it was designed with external (free-sliding) post-tensioning cables within the boxes.

The height of the box girder, measured in the centreline of the road on the sections of constant height, is 3.50 m. From

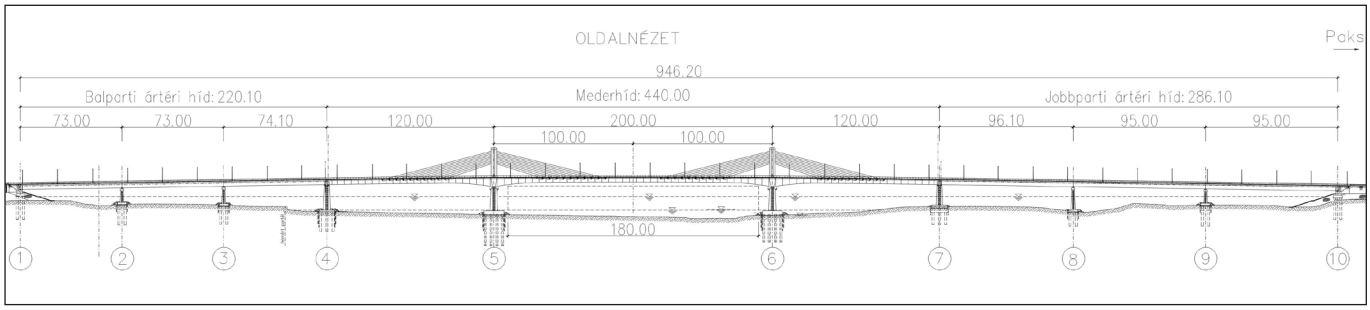


**Fig 2:** *Full-length elevation of the bridge*

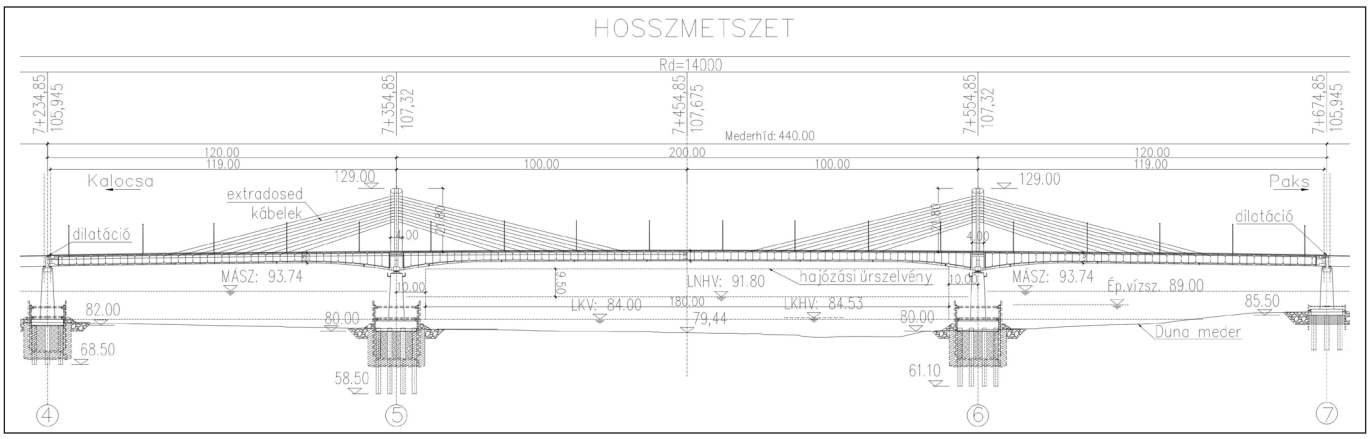


**Fig 3:** *Longitudinal section of the river bridge*

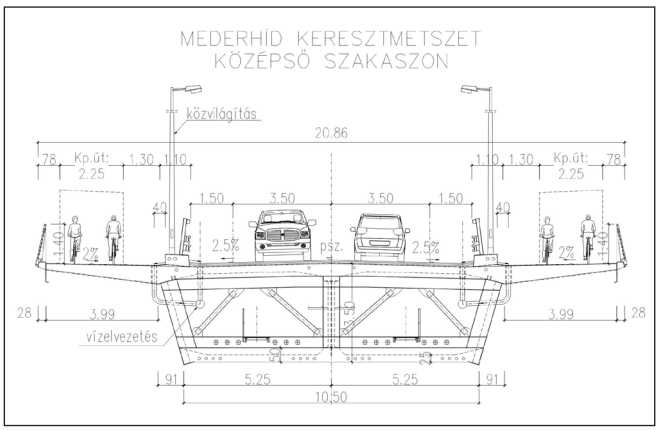


**Fig 4:** *Cross-section of the river bridge at the central section*

piers 5 and 6 to the section of the extradosed cable anchorages, the height of the box girder varies, reaching 6.50 m above the piers.

The width of the superstructure (Figure 4) is not uniform along the length of the river bridge; it is 19.26 m at the connection to the floodplain bridges, and the maximum width at the pylons is 23.26 m.

Ten extradosed cables were installed on both sides of the pylons, anchored at 5 m intervals to the superstructure. The two-column pylons are solid monolithic reinforced concrete structures which were integrated with the superstructure's cross girders above the piers. The cables were anchored outside the pylon's shell using steel structures—so-called link elements—embedded in the concrete of the pylon.

# 3. STRUCTURE OF THE RIVER BRIDGE

## 3.1 FOUNDATIONS

The foundations of the piers were constructed identically on the four substructures using large diameter ϕ1.50 m bored reinforced concrete piles. At the shared piers 4 and 7, the piles are arranged in three rows, whilst at the riverbed piers 5 and 6, the piles are arranged in four rows.

The construction of the pile-cap beams and the substructures was adjusted to the topography of the Danube riverbed. At the shared piers 4 and 7, the foundation work was carried out from an artificial island constructed around the piers, within an excavation bounded by cofferdams. (Figure 5)

For pier 5 and 6, a box-shaped structure (precast shell element) was lowered from a barge to delineate the working area. Based on the required working space dimensions and taking into account the lifting weight, the precast shell element had to be cut into two sections vertically. The boxes were constructed with identical floor plans measuring 29.70 m x 15.00 m, with lifting weights of 153 t and 180 t.

**Fig 5:** *KP4 pier sheet pile cofferdam*

**Fig 6:** Drone photo

## 3.2 SUBSTRUCTURE

The piers have solid wall structure. In plan view, the pier walls are pointed at the front and rear; the surfaces of the piers exposed to ice flow are clad with granite coping stones. The walls were constructed with an upward slope of approximately 1:20; the top width of the piers is 3.50 m for the shared piers and 4.00 m for the river piers.

Plinths were constructed at the top of the piers; the superstructure rests on the piers via the bearings placed on the plinths.

## 3.3 PYLON

The pylons are solid monolithic reinforced concrete structures, which were constructed as an integrated unit with the superstructure's cross girders above the river piers. They have a two-column design, with the pylon axis positioned 7.10 m transversely from the bridge axis. Their cross section is elliptical with dimensions 4.00 x 2.00 m. Their height from the deck level is 21.80 m, and their upper, capping section is cut at an angle. (Figure 6)

For reasons of concrete pouring and steelwork, the total height of the pylon was constructed in 7 stages. The construction stages were on average 3.00 m in height. The reinforcement of the pylon base, using D25 mm and D28 mm reinforcing bars arranged in two rows, met the design requirements.

## 3.4 SUPERSTRUCTURE

The main girder is a dual-cell box girder, the inclined outer webs and the central web are formed by steel trapezoidal sheets. The bottom slab and the cantilevered deck slab of the box section are made of reinforced concrete. Compared to the conventional composite structure (steel girder and participating reinforced concrete deck), in this case the bottom RC slab is also included in the composite structure; this is the origin of the term 'hybrid' (Figure 7).

The workshop drawings of the 5-metre units of the steel

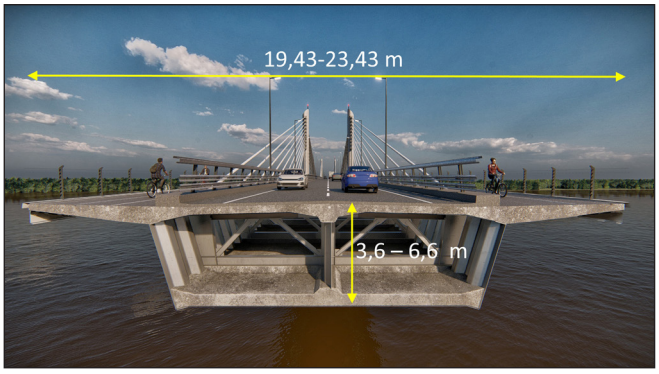


**Fig 7:** Cross-section taken from the visualization

stiffening girder were created in 3D using the TEKLA software. One structural unit consists of the outer inclined trapezoidal webs; an inner vertical trapezoidal web and a cross bracing made of 'I' sections.

When preparing the reinforcement plans for the bottom and deck sabs, the quantity of reinforcing steel required based on the structural analysis, the applicable reinforcement shapes, the shear connectors protruding from the steel structure, and the casing ducts of the bonded post tensioning cables presented significant challenges as obstacles.

## 3.5 EXTRADOSED CABLES

The stiffening girder is anchored by 10-10 extradosed cables in the side spans, by 10-10 extradosed cables in the main span per each pylon, totalling 80 cables with variable inclination. The applied tensioning cable system is the Freyssinet H2000 type. Cable type: parallel-wire strands consisting of 7 wire strands, with strand material grade Y1860S7. The 37-, 43- and 55-strand cables were anchored and tensioned at reinforced concrete anchor blocks formed beneath the deck cantilever. The upper passive anchoring of the cables took place in the outer part of the link element embedded into the reinforced concrete cross-section of the pylon. (Figure 8)

The angle of the cables enclosed by the deck measured in

**Fig 8:** Upper anchorage node of the extradosed bridge

the vertical plane varies between 13.9° and 18.3° , and their lengths vary between 34.5 and 80.3 m. In both the side and river spans, cables no. 9 and no. 10 were fitted with dampers.

The cables were tensioned in two stages using the Isotension method, with tensioning carried out strand by strand.

## 3.6 BEARINGS AND EXPANSION JOINTS

The superstructure is supported at each substructure by three MAURER-manufactured bearings corresponding to the three-web cross-section. The central bearings are fixed in the transverse direction. The two outer bearings are movable at piers 4, 6 and 7, and fixed in the longitudinal direction at pier 5. The

**Fig 10:** First segment and its auxiliary structure on the river pier

scale of the bridge is well illustrated by the fact that the vertical load-bearing capacity of the outer bearings on the river pier is 55,000 kN!

At the joints of the structures, MAURER DS 320/400 watertight expansion joints were installed above pier No. 4, and MAURER DS 640/800 watertight expansion joints above pier No. 7.

# 4. CONSTRUCTION METHODOLOGY

## 4.1. FREE-CANTILEVERING AND CONCRETE CASTING

The superstructure was constructed applying the free-cantilever method. (Figure 9) Free-cantilever assembly was necessary for the hoisting and fixing of the main steel girder structure, whilst free-cantilever concreting was required for the bottom and deck slabs to be cast onto the already fixed steel load bearing structure.

In the detailed schedule, the construction cycle time was

**Fig 9:** Free cantilevering in the main span

**Fig 11:** *Auxiliary structures on the Kalocsa side*

14–16 days. As an example, the most important stages relating to the construction of the P10/M10 segments are listed below:

- P10 / M10 segments: lifting and fixing of the steel main girder
- Tensioning of the extradosed cables for P08 / M08 construction segments in 4 stages
- P10 / M10 segments: concreting of the bottom slab
- P10 / M10 segments: concreting of the deck slab
- P10 / M10 segments: tensioning of the bonded post tensioning cables
- P10 / M10 segments: relocation of PERI formwork traveller for the construction of the next segment.

In each of the steps listed, the work pertaining to the construction segment was first carried out in the side span, and only then was the work moved to the segment in the main span.

Temporary structures are essential for free-cantilever construction. The free-cantilevering began with the construction of the segments P01-PM00-M01 on trestles (Figure 10). The PERI formwork travellers, each weighing approximately 112 tonnes, were hoisted onto this three-segment launching section, on both the bank and riverbed sides.

**Fig 12:** *SJ2 temporary support and scaffolding below the segments P24-P20, prior to the assembly of the closure segment*

The temporary bridge supports marked SJ1 and SJ2 were positioned 35 m and 85 m from the river piers towards the side spans. Because of their structural design, they not only operated under compression but due to the planned tension rods, were also able to withstand significant tensile forces. (Figure 11)

Due to construction methodology reasons, the nearly 20-metre-long section at the shared piers comprising segments P24–P20, was constructed not using free-cantilevering but on a full scaffolding system. (Figure 12)

## 4.2 POST-TENSIONING SYSTEMS

In case of structures built by free-cantilever method, the tensile stress generated in the reinforced concrete deck slab is counteracted using bonded post-tensioning cables. The cables were threaded into protection ducts installed simultaneously with the reinforcement during the phase following the concreting of the deck slab. Dywidag Y1860S7 type cables with a 150 mm$^2$ cross-section and 12 or 15 strands were installed as bonded cables. The cables were generally tensioned using a 15-strand large capacity stressing jack, except for the cables in the P24 section at the end of the side span, where a mono strand stressing jack was also used.

Due to the 3-web design of the main girder, we designed a minimum of 3 cables per cross-section in the deck slab, but in areas subject to varying loads, we also used 5 cables. (Figure 13)

The haunching of the deck slab ensured that sufficient concrete depth was available in most places for the installation of the cable anchor heads. For the cables required for closure, we designed additional anchor blocks protruding beyond the deck slab contour. (Figure 14)

In the bottom slab, based on the construction and final stage static calculations, we designed bonded cables in the range of segments P24-P12 in the side span, and between segments M15-M15’ in the main span. As the thickness of

**Fig 13:** Post-tensioned cable anchorage in the deck slab

**Fig 14:** RC anchorage block at the deck slab

**Fig 15:** RC anchorage block at the bottom slab

the bottom slab did not allow for the cables to be anchored, additional concrete blocks were incorporated at these points. (Figure 15)

In the final stage, to absorb the additional stresses arising from the live load, we designed a so-called free-sliding post-tensioning cable system inside the box, running outside the reinforced concrete structure. The planned strands are made of material grade Y1860S7, with a cross-sectional area of 150 mm². In terms of configuration, we used a system consisting of 4 straps, each containing 4 strands (4x4-150).

## 4.3 CLOSURE

In construction terminology, 'closure' refers to the connection of two separately constructed bridge sections using an intermediate 'closing element', thereby ensuring structural continuity. Based on the construction phases, this operation was carried out on the bridge in question at both the main span and the side span.

On the riverbank side, the P24–P20 segments were constructed on scaffolding. The cantilevered bridge section extended to the P18 segment, and the two structural sections were joined together with the installation of the intermediate P19 element.

For the main span, the two half-spans, each with a cantilever length of 97.5 m, were completed up to construction segment M19. To install the MM20 closure segment, an auxiliary bracing structure was anchored to the cantilevers of the deck slab. The closure of the completed structures can be carried out once the two cantilever ends are at the same height. The height adjustment of the cantilever ends was carried out by moving the formwork traveller on the Kalocsa side into position and by applying additional loads. The soft stiffness of the cantilever structure is well illustrated by the fact that, when dismantling the 42-tons bottom formwork of the formwork traveller, we calculated a vertical displacement of ~120 mm at the cantilever end.

# 5. CONCLUSIONS

The new Kalocsa-Paks Danube Bridge, the 20th bridge on the Hungarian section of the Danube, was opened to traffic in June 2024. The construction work on the bridge was carried out by Duna Aszfalt Zrt. The bridge design tasks were undertaken by CÉH zRt., as the lead designer of the bridge. In this article, we describe the design process and experiences gained during construction of the extradosed riverbed bridge spanning the Danube, which is part of a structure comprising three bridges with a total length of 946 m.

The 440 m long riverbed bridge is a three-span, extradosed bridge with a hybrid cross-section, featuring a two-cell box girder parabolically haunched above the riverbed piers, with spans of 119.0+200.0+119.0 m. The main girder of the bridge is a dual cell box structure, the inclined outer webs and the central web are formed by trapezoidal steel sheets. The bottom slab and the cantilevered deck slab of the box section are made of reinforced concrete. A total of 80 extradosed cables were installed on both sides of the pylons, anchored every 5 meters to the stiffening girder, with 10 cables on each side. The two-column pylons are solid monolithic reinforced concrete structures, which were integrated with the superstructure's cross girders above the river piers.

The unique design of the bridge superstructure, the combined use of reinforced concrete and steel structures, the simultaneous use of different tensioning systems, and the structural behaviour of the trapezoidal steel webs posed a serious challenge for both the contractor and the designer.

The anchoring of the extradosed cables at the pylon, combined with the bespoke design steel structure in accordance with the design codes, meant that the amount of cables required in the side and main spans could vary. Replacing the saddle support with a link element allowed for a more economical amount of cable that more effectively followed the force distribution.

From the design side, processing the construction phases and keeping the calculations up to date required significant

capacity. From the contractor's side, a major challenge was, for example, the scheduling of the steel, reinforced concrete and tensioning teams associated with the construction segments, ensuring they could carry out their work without hindering one another.

Over the long months of construction, the contractor and the designer worked closely together to successfully resolve these issues, united by the common goal of building a spectacular bridge of high technical quality.

**Dr. Sándor Kisbán** (1949)
Chartered structural engineer (BME, 1973). Chief Bridge Engineer at CÉH zRt. He began his career as a bridge designer in 1975 at Uvaterv, where he was involved in the design of long-span steel bridges (Szeged Northern Tisza Bridge, Tiszapalkonya Road Bridge, Yugoslavia – Novi Sad Cable-Stayed Danube Bridge). He obtained his doctoral degree in the field of cable-stayed bridges in 1986 (Technical University of Budapest – Department of Steel Structures). Since 2002, he has been working as a bridge designer at Céh zRt, where he has designed and supervised the design of numerous inland river and motorway bridges (M0, M31, M6 motorway and viaducts, Megyeri Bridge). He is the lead designer of the Tomori Pál Bridge. In recognition of his professional achievements, he received the Dénes Gábor Award (2008), the Széchenyi Award (2009) and the István Menyhárd Award (2023), and in 2024 he was honoured with the Bridge Engineer of the Year Award. He is a member of the Hungarian Section of ***fib***.

**Pál Pusztai** (1974)
Chartered Structural Engineer (BME, 1998). He began his career as a bridge designer at Hídépítő Zrt., where he was involved in the design of the Zalalövő–Bajánsenye railway prestressed concrete bridge. From 2001, as an employee of CÉH zRt., he has been involved in the design of the motorway bridges on the eastern sector of the M0 motorway, the design of the bridges on the M31 motorway as the lead designer of the section, the preparation of the approval and construction drawings for the Megyeri Bridge, the design of the viaduct no. 1693 on M6 motorway , and the design of the Hódmezővásárhely roundabout bridge. Lead designer of the Tomori Pál Bridge. Member of the Hungarian Section of ***fib***.

**Rudolf Kiss** (1972)
Chartered Structural Engineer (BME, 1996). Chief Bridge Engineer at CÉH zRt., employed by the company since 1997. As a designer and section lead designer, he was involved in the design of the Füzesabony–Polgár section of the M3 motorway, the M3–Miskolc section of the M30 motorway, the Northern, Eastern and Southern sectors of the M0 ring road, and the Bóly–Szentlőrinc section of the M60 motorway. He was involved in the design of the restoration of the Margit Bridge and the Széchenyi Chain Bridge in Budapest as listed monuments. He is the project manager for the design of the Pál Tomori Bridge.

# DYNAMIC LOAD TESTING OF A POST TENSIONED REINFORCED CONCRETE ARCH BRIDGE FOR EXPERIMENTAL REASONS USING A LEOPARD 2A7HU MAIN BATTLE TANK


Bence Hajós - Ákos Kővári

https://doi.org/10.32970/CS.2026.1.3

*When planning military operations, mobility is fundamentally influenced by the load capacity of bridges. Exact baseline data and parameters are needed to assess the load capacity of existing road bridges. Test loading can measure the actual behaviour of the bridge structure, which gives a more accurate response than numerical calculations based on hypothetical assumptions. This paper presents a test loading carried out in Hungary with military vehicles, a heavy logistics vehicle wheeled and a Leopard 2A7HU main battle tank, and its main results. The study contributes to reliable calculation of the dynamic effects of tracked vehicles.*

**Keywords:** critical military infrastructure, military mobility, road bridge, load capacity, load test

## 1. INTRODUCTION

Mobility has a critical impact on the success of military forces. When planning military operations, it is essential to identify routes suitable for transportation. (Kovács, 2004) This selection requires knowledge of the planned load effects and the resulting bridge load-bearing capacity requirements.

In Hungary, the military assessment of the load-bearing capacity of existing road bridges typically involves a conservative design verification based on the civilian bridge registry. Extreme conservatism benefits safety and enables quick and simple assessment, but it can restrict military mobility, particularly when moving heavy military equipment. (Lenner, 2014; Hajós, 2023; Hajós, 2024a; Hajós, 2024b)

A critical aspect of detailed structural analysis is the selection of relevant load factors, the most important of which are the safety (partial) factor and the dynamic impact factor. Several studies (Everitt, 2019; Pinkney et al., 2022; Everitt et al., 2019) have pointed out that the dynamic factors for tracked and wheeled vehicles are significantly different.

Experimental investigations of the loads exerted by military tracked vehicles on bridge structures have received relatively little attention to date. Bridge load tests for this purpose were conducted in Canada on a two-span steel-concrete composite bridge (Everitt et al., 2019) and a modular military steel bridge (Pinkney et al., 2022). In addition, tests specifically for tracked loads were conducted on two small-span polymer composite military bridge systems (Kosmatka, 2011; Robinson et al., 2011).

In the bridge load tests published to date, the static and dynamic values associated with each load were primarily determined by measuring steel stress using electrical strain gauges, from which the dynamic surplus was calculated.

The significance of experimental testing of tracked vehicles is confirmed by the fact that all previous studies have confirmed that for tracked vehicles, it is sufficient to calculate the dynamic surcharge used for wheeled vehicles at 50% (Everitt et al., 2023) due to the significantly more favourable bridge–vehicle dynamic interaction. The dynamic additional load on the bridge depends on the characteristics of the bridge and the vehicle traveling on it, as well as their interaction.

Further testing is needed to introduce the reduced dynamic factor for tracked vehicles on a general basis. It is justified to extend this testing to a larger range of bridges (span size, structural system, base material) and to various types of military vehicles.

The military load-bearing capacity assessment of existing road bridges is governed by the NATO standard (AEP-3.12.1.5 2024), which specifies the classification rules for both vehicles and bridges. According to the standard, if the vehicle's classification number (MLC – Military Load Classification) is lower than the bridge's classification number, the vehicle may safely cross the object. The technical standard does not specify exact values for the safety and dynamic factors to be applied in the structural analysis; it leaves the determination of these factors to the discretion of the implementing nation. This further confirms that the load-bearing capacity classification of bridges can be substantially improved using more precise factors determined through experimental load tests conducted with military vehicles.

The military load test which mentioned previously has been completed in November 2024 is related to the Canadian bridge load test. This experimental study examines a 36-meter-span post-tensioned reinforced concrete arch bridge. The deflection of bridge were measured under 37 different load conditions caused by wheeled and tracked military vehicle loads, as well as, for comparison, a civilian agricultural vehicle (Hajós, 2025a).

## 2. LOCATION OF TEST LOADING, SELECTED BRIDGE STRUCTURE

The road bridge selected for the test load is located near the village of Kecskéd, spanning the Által-ér, which is a medium stream. The bridge was built in 1965 after the previous bridge, which had a smaller span, collapsed during a summer flash flood.

The bridge has a clear span of 36 m and spans the watercourse without intermediate supports. Its structural system consists of a monolithic reinforced concrete lower-deck arch bridge with a post-tensioned reinforced concrete slab, which also carries the horizontal (tension) load of the arch structure. A unique feature of the bridge is that the two main reinforced concrete arch girders were constructed without an upper cross-brace above the roadway, thus there is no clearance height restriction on the bridge. *Fig. 2-3.* The bridge was designed for a Class B live load in accordance with the 1956 Hungarian Highway Bridge Code (KPM Sz. HI/I-56 R, 1956) in effect at the time of construction, consisting of a single two-axle vehicle with a total mass of 30 tons *Fig. 1*, applying a distributed load of 300 kg/m2 across the entire bridge deck simultaneously. The bridge structure's registered load-bearing capacity is 40 tons (Original plans 1964).

When selecting the bridge, one of the criteria was that it should ideally be a reinforced concrete structure, in contrast to the steel structures used in previous similar tests. From a measurement technology perspective, it is advantageous that this bridge has a larger span (36 m), so the movements to be tested are also larger; furthermore, the space under the bridge is easily accessible for installing the equipment needed for the test load, and civilian traffic on the bridge is negligible at night, which would otherwise inevitably interfere with the measurements.

**Fig. 1:** *The 30-ton Class B ideal load as defined by the 1956 Hungarian Bridge Code (edited by the authors)*

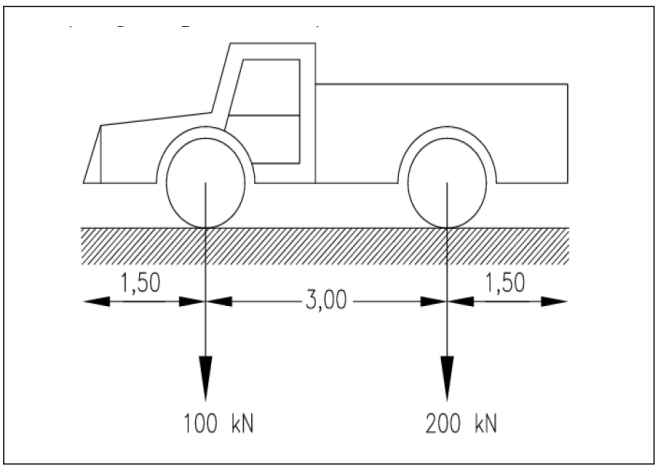


**Fig. 2:** *Longitudinal section, side view, and top view of the Által-ér Bridge at Kecskéd, showing the test load measurement points (edited by the authors)*

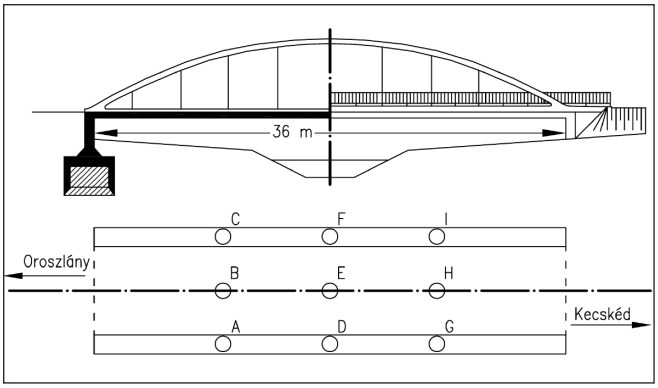


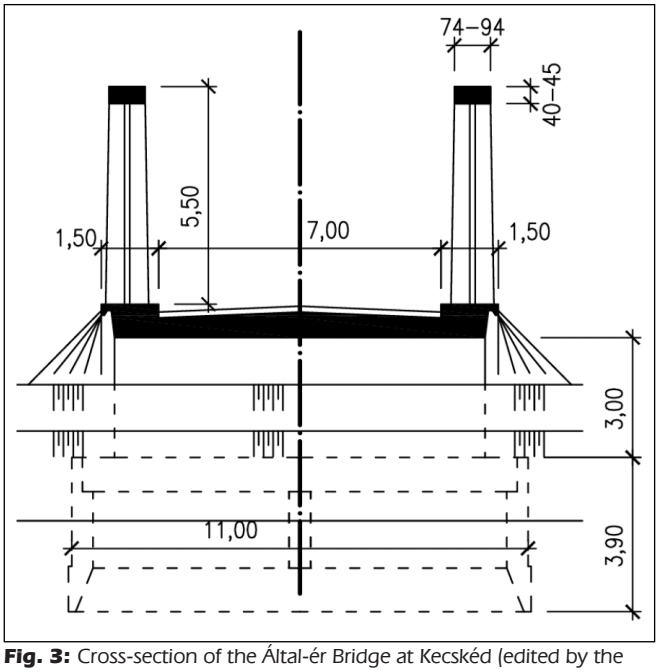


**Fig. 3:** *Cross-section of the Által-ér Bridge at Kecskéd (edited by the authors)*

The bridge was completely renewed in 2011. At that time, the old pavement and insulation were removed, and new insulation system and asphalt pavement were laid over a new levelling layer; in addition, the exposed reinforced concrete surfaces were repaired and treated with modern corrosion protection (Plan of renewing 2011).

Now, the bridge is in good condition; detailed visual inspections were conducted before and after the load test. No significant damage was observed.

## 3. APPLIED MEASUREMENT TECHNOLOGY

The deformations of the bridge were examined at a total of nine points. Vertical displacements were detected using an inductive transducer connected to a computerized measurement system. The designated measurement locations were the same as those used during the bridge's construction for the load test conducted in January 1966, to ensure comparability.

The measurement points were designated longitudinally at the quarter, half, and three-quarter points of the bridge, and transversely at the axes of the two main girders and at the center of the bridge.

The sensitivity of the calibrated measurement system was 0.06 mm. At the measurement locations, small steel plates were affixed to the underside of the reinforced concrete deck slab; their vertical displacement was transmitted via a magnetically secured wire to an electronic sensor fixed on the support scaffold under the bridge. In accordance with the previously calculated movements, displacement sensors were used with a 50 mm measurement range. The nine sensors were connected to a central data logger. The sampling rate used during the dynamic measurements was 60.1 Hz.

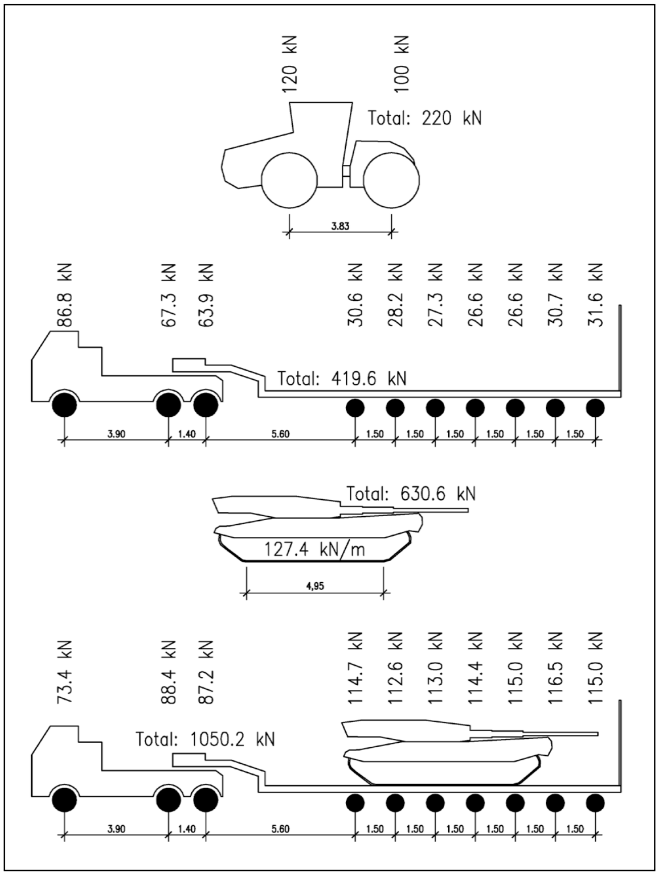


**Fig. 4:** Four types of vehicles used for the test load (edited by the authors)

## 4. TEST VEHICLES

Four different types of vehicles were used for the test load. To test and verify the installed measurement system and to ensure comparability with military vehicles, an agricultural tractor were used with a gross weight of 22 tons.

The military test load was conducted using three different types of vehicles. In order of total weight: a ten-axle, empty heavy-duty transport trailer (42 tons), a tracked main battle tank (63 tons), and the trailer loaded with the main battle tank (42 + 63 = 105 tons). *Figure 4* shows the schematic drawings and load data for the four test vehicles. The tracked main battle tank used for the test load was a Hungarian Leopard 2A7HU, which was transported with the gun turret in the transport position throughout the entire test. Its schematic drawing was provided accordingly.

Prior to the test load, Magyar Közút Nonprofit Zrt. (Hungarian National Roads - operator) used a mobile axle load scale vehicle to accurately weigh an empty trailer prepared for departure, followed by a loaded trailer, in Tata. The load data based on the measurement results were taken into the calculation.

## 5. PROGRAM OF THE LOAD TEST

According to the applicable regulations, a detailed plan for the load test had to be prepared, which included the planned loads, measurement methods, and expected deformations. Since the planned test loads (63 and 105 tons) significantly exceeded the bridge's registered load-bearing capacity (40 tons), detailed structural calculations were also prepared for the test loading based on two independent model calculations.

The bridge administrator issued its consent to the test loading plan, and the competent transportation construction authority granted its approval. Based on the test loading plan, the Ministry of Defence decided to ensure military participation. The 1st György Klapka Armoured Brigade received its mission orders from the Defence Staff, without which the experimental test could not have been carried out.

It was necessary to completely close the bridge for the duration of the measurements. Traffic on the national road crossing the bridge is moderate during the day and minimal at night; therefore, the full test was scheduled for the late-night hours to minimize disruption to residents. The measurements were synchronized so that the last scheduled public bus could cross the bridge before the closure. On a few occasions between individual measurements, passenger cars waiting in both directions were allowed to pass.

To install the planned monitoring system, a temporary

**Fig. 5:** Videos on running the load test (edited by the authors)

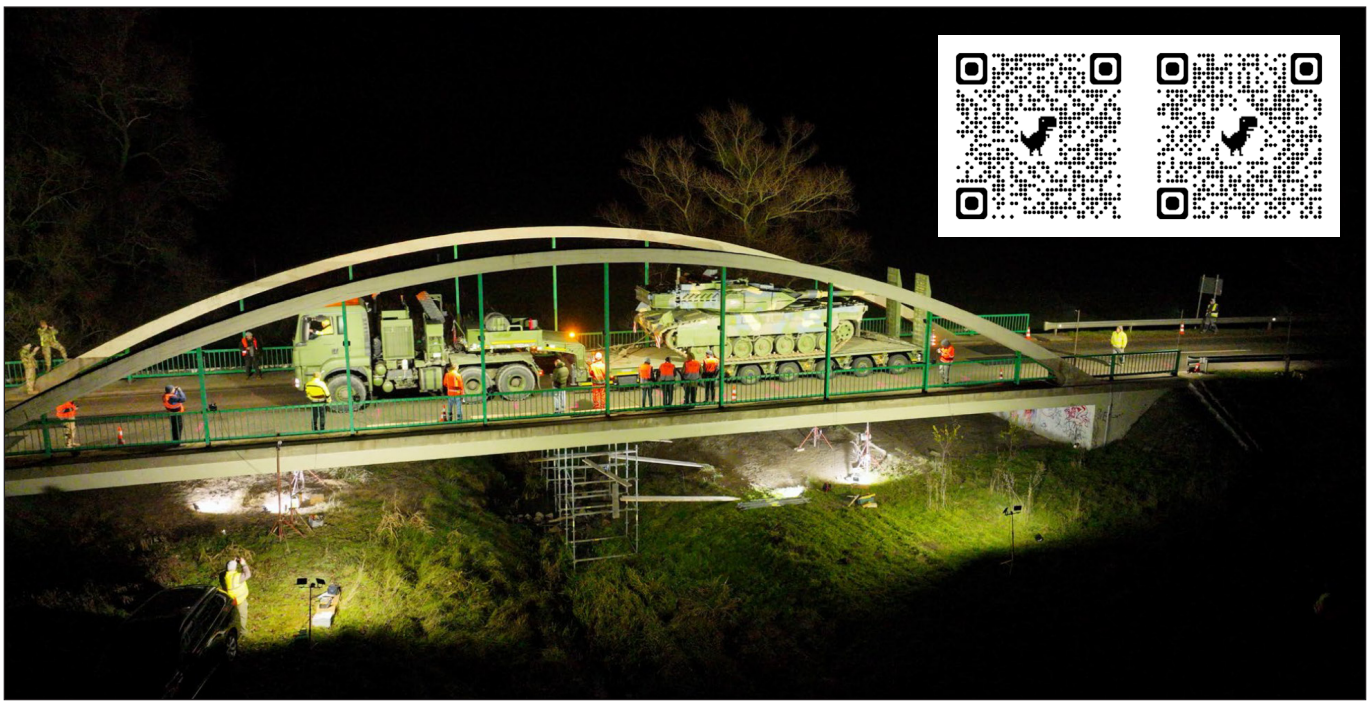

scaffolding was erected under the bridge for the measuring equipment. Spotlights were installed around and under the bridge to ensure safe working conditions and to document the test loading *Fig. 5*.

The preparatory work was completed while it was still daylight, before the military vehicles arrived, the measurement system was tested using an agricultural tractor with a total weight of 22 tons. This test also allowed for a comparison of civilian and military loads.

Total of 37 load positions were tested, excluding measurements of the unloaded (empty) bridge. The individual load positions were tested in order of increasing load magnitude. Static and dynamic measurements were performed with the first three vehicles (22, 42, and 63 tons), while only a single dynamic measurement was carried out with the fourth, heaviest test vehicle (105 tons).

The dynamic testing program for the first three vehicles included a test with plank obstacles simulating uneven road surfaces. Following the Canadian military test load methodology, five plank obstacles were placed on the asphalt pavement at the centre of the bridge, which significantly increased the dynamic load on the passing vehicles. Plank obstacles were used identical to those used in previous Canadian load tests. The planks were placed, which had a cross-section of 5x20 cm, symmetrically on the roadway in the centre of the bridge, with a spacing of 3 meters between each set of planks.

The test load was originally designed to allow us to perform dynamic measurements at various speeds using the tracked main battle tank, provided that the short approach distance before the bridge allowed for speeds of up to 40 km/h. Unfortunately, due to technical reasons at the time of measurement, the speed of the Leopard 2A7HU main battle tank was limited to 5 km/h regardless of the test load, so the tracked load tests planned at higher speeds were not carried out.

During the test loading, only the vertical deflections were measured at the nine points; the parameters of dynamic behaviour could also be calculated from the deflection. This differs from previous track-mounted military test loadings, where dynamic behaviour was examined using electrical strain gauges bonded to the steel structure. In this case, the use of strain gauges on a reinforced concrete structure would have been difficult.

## 6. RESULTS OF THE STATIC TEST LOAD

The preliminary raw measurement results from the test loading could be continuously monitored on-site via the data collector computer. This allowed for immediate verification of the measured and calculated deflections. The measured values remained below the preliminary calculations, in many cases by about 50%. The bridge behaved significantly stiffer than the previously calculated value. *Table 1* shows the measured static deflection values. *Figure 2* illustrates the locations of the nine measurement points.

The measured results are consistently lower than the calculated values, ranging from 56% to 82% of the calculated values at the mid-span. Significantly lower deflection is a typical phenomenon during test loading of reinforced concrete bridges. One of the most important reasons for this stems from the consideration of specific material properties. The levelling layers from the bridge's subsequent renovations may also have increased the bridge's stiffness.

The individual measurement values correlate well with one another, which confirms both the proper functioning of the measurement technique used and the good condition of the bridge structure. However, the bridge is symmetrical in both the longitudinal and transverse directions, minor differences can be observed between the individual pairs of values.

**Table 1:** Detailed deflection values ot the static load test

| Nr. | Load positions | Deflections [mm] | | | | | | | | |
|---|---|---|---|---|---|---|---|---|---|---|
| | | A | B | C | D | E | F | G | H | I |
| 2 | Tractor in axis, at 1/4 of span | **0.86** | **1.05** | **0.97** | 0.14 | 0.25 | 0.15 | -0.37 | -0.25 | -0.33 |
| 3 | Tractor in axis, at 1/2 of span | 0.61 | 0.7 | 0.61 | **1.15** | **1.49** | **1.09** | -0.05 | -0.09 | -0.05 |
| 4 | Tractor in axis, at 3/4 of span | -0.3 | -0.24 | -0.25 | 0.52 | 0.7 | 0.52 | **0.99** | **1.24** | **0.96** |
| | | | | | | | | | | |
| 14 | Empty trailer in axis, at 1/4 of span | 0.91 | 1.10 | 0.97 | 0.89 | 1.16 | 0.92 | -0.25 | -0.24 | -0.25 |
| 15 | Empty trailer in axis, at 1/2 of span | 0.33 | 0.59 | 0.33 | 1.13 | 1.47 | 1.16 | 0.73 | 0.97 | 0.73 |
| 16 | Empty trailer in axis, at 3/4 of span | -0.14 | 0.01 | -0.11 | 0.92 | 1.27 | 0.96 | 0.89 | 1.10 | 0.85 |
| | | | | | | | | | | |
| 25 | Leopard MBT in axis at 1/4 of span | **2.92** | **3.62** | **2.85** | 0.82 | 1.06 | 0.77 | -1.03 | -0.89 | -1.04 |
| 26 | Leopard MBT in axis at 1/2 of span | 0.95 | 1.34 | 0.87 | **3.46** | **4.39** | **3.32** | 0.66 | 1.01 | 0.61 |
| 27 | Leopard MBT in axis at 3/4 of span | -1.13 | -0.86 | -1.1 | 1.09 | 1.49 | 1.03 | **3.04** | **3.72** | **2.99** |
| | | | | | | | | | | |
| 30 | Leopard at left side and 1/4 of span | **3.57** | **3.32** | **2.20** | 0.86 | 0.95 | 0.52 | -1.18 | -0.8 | -0.94 |
| 29 | Leopard at left side and 1/2 of span | 1.11 | 1.10 | 0.59 | **4.27** | **4.25** | **2.48** | 0.81 | 1.08 | 0.44 |
| 31 | Leopard at left side and 3/4 of span | -1.35 | -1.08 | -1.05 | 1.29 | 1.35 | 0.71 | **3.90** | **3.78** | **2.25** |
| | | | | | | | | | | |
| 33 | Leopard at right side and 1/4 of span | **2.29** | **3.75** | **3.72** | 0.61 | 1.06 | 1.03 | -1.09 | -1.04 | -1.34 |
| 34 | Leopard at right side and 1/2 of span | 0.53 | 1.10 | 0.95 | **2.53** | **4.06** | **4.14** | 0.48 | 0.97 | 0.89 |
| 35 | Leopard at right side and 3/4 of span | -1.01 | -0.86 | -1.16 | 0.71 | 1.19 | 1.10 | **2.25** | **3.37** | **3.59** |

These are consistent with the findings of other load tests.

Initial expectations and structural calculations were contradicted by the fact that the sinusoidal deflection pattern typically observed in arch structures under one-sided loading was significantly less pronounced. It is characteristic of clear arches that the greatest vertical deflections do not occur at the centre of the span, but rather in the quarter-spans under half-side loading, which is also significant from a structural engineering perspective. According to preliminary structural calculations, the maximum centre-of-span deflection calculated for the load of a main battle tank standing at the edge of the track is 7.15 mm; whereas in the quarter-span it is 10.63 mm. In contrast, the measured value at the centre of the bridge span was 4.21 mm (59%), and in the quarter-span only 3.70 mm (35%). The smaller deflections in the quarter-spans indicate that the reinforced concrete deck slab (beam effect) significantly stiffens the main girder spans (arch effect). The superstructure behaves as a Langer girder, and the deck slab deflections are correspondingly smaller. The maximum deck deflection during the static test was 1.35 mm (under load position No. 31).

The rigid deck behaviour can also be observed in the calculated cross-beam deflections at the measurement cross-sections. Under a 63-ton main battle tank load, the transverse deflection between the two main girders, spaced 8.90 m apart, was 1.00 mm at the bridge's mid-span cross-section during static measurements and 0.95–1.01 mm during dynamic measurements. The maximum transverse deflection observed under the heaviest load (105 tons) was 1.12 mm.

## 7. RESULTS OF THE DYNAMIC TEST LOAD

When analysing unprocessed dynamic data, it is possible to clearly distinguish between the quasi-static component of deflection and the dynamic oscillation superimposed on it. It is standard practice to isolate small dynamic effects using a filter (e.g., a moving average). No such filtering was applied during the analysis of the data; thus, the extreme values of the measured deflection also include the additional value of the dynamic oscillation. If a filter had been used, the maximum deflections would have been smaller.

The oscillation superimposed on the quasi-static deflection depends on the vehicle's excitation parameters, the smoothness of the track surface, the vehicle's suspension system, the type of undercarriage (tracked or wheeled), the number of axles, the total mass, and the vehicle's speed.

In dynamic measurements performed with a Leopard main battle tank, the frequency of the deflection-induced oscillation was around 5 Hz (4.8–5.4 Hz) during passage in all load conditions. For the agricultural tractor a similar value of 5.2 Hz was calculated. When the trailer passed through, the additional oscillation did not have a significant calculable frequency.

*Fig. 7* shows an enlarged view of a small section of *Fig. 6.* The 2-second data set shows the oscillation of the deflection at two measurement points on the mid-span cross-section of the span. The amplitude of the dynamic oscillation at the mid-span cross-section of the main girder on the load-bearing side (measurement point D) was 0.12 mm. This small vibration causes an additional deflection of +1.87% on top of the quasi-static deflection.

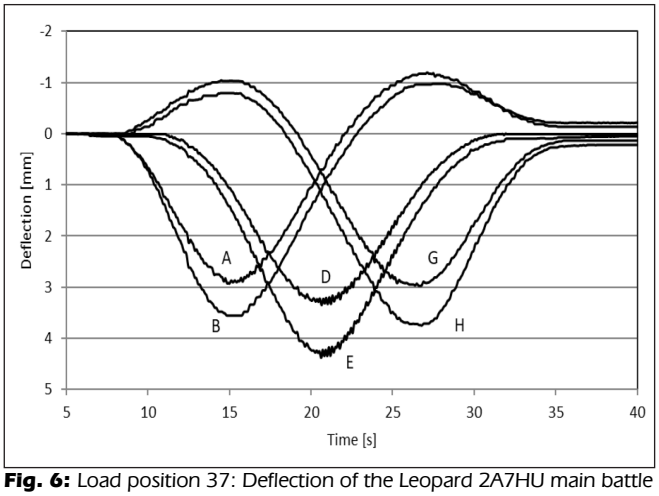


**Fig. 6:** Load position 37: Deflection of the Leopard 2A7HU main battle tank at a speed of 5 km/h (edited by the authors)

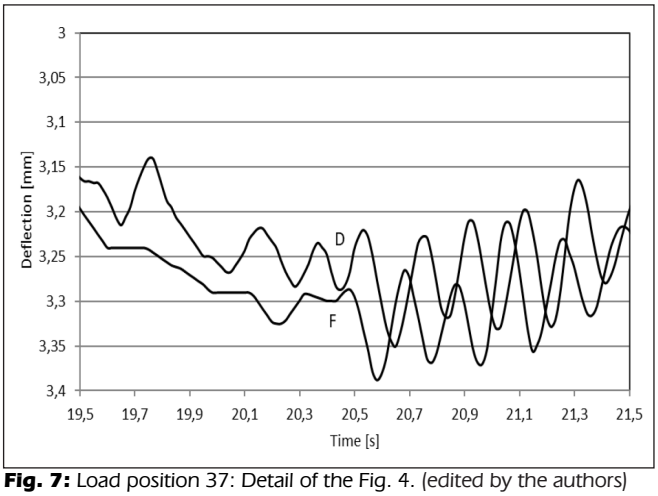


**Fig. 7:** Load position 37: Detail of the Fig. 4. (edited by the authors)

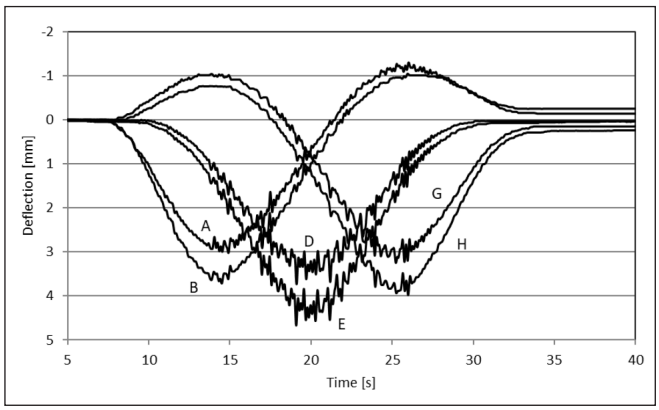


**Fig. 8:** Load position 41: Deflection of the Leopard 2A7HU main battle tank at a speed of 5 km/h with plank obstacles (edited by the authors)

It was observed that the tracked main battle tank excites the bridge more when moving in reverse, and larger oscillations can be measured than when moving forward.

The uneven track was modeled using plank obstacles *Fig. 8*. This resulted in an extraordinary additional dynamic load.

A comparison of measurements taken with and without the boards shows that the quasi-static deflection values remained unchanged, while the superimposed dynamic vibration increased nearly fivefold, resulting in an average increase of 7% in maximum deformations.

Among the measurements conducted with plank obstacles *Table 2*, the agricultural tractor exhibited the largest measured dynamic increase (+81%) compared to measurements without planks. At this load, the amplitude of its dynamic os-

**Table 2:** *The additional dynamic deflection of an uneven road surface (with a plank) at the center of the bridge*

| Nr. | Load positions | Measured point | |
|---|---|---|---|
| | | D [mm] | F [mm] |
| 5 | Tractor, 5 km/h in reverse | 1.22 | 1.15 |
| 10 | Tractor 5 km/h with PLANKS forward | 1.43 | 1.38 |
| | Dynamic surplus | +17% | +20% |
| 6 | Tractor 10 km/h forward | 1.17 | 1.13 |
| 11 | Tractor 10 km/h with PLANKS in reverse | 1.75 | 1.67 |
| | Dynamic surplus | +50% | +48% |
| 7 | Tractor 20 km/h in reverse | 1.22 | 1.11 |
| 12 | Tractor 20 km/h with PLANKS forward | 2.02 | 2.02 |
| | Dynamic surplus | +66% | +81% |
| | | | |
| 17 | Empty trailer 5 km/h in reverse | 1.16 | 1.09 |
| 23 | Empty trailer 5 km/h with PLANKS in reverse | 1.84 | 1.74 |
| | Dynamic surplus | +58% | +59% |
| | | | |
| 36 | Leopard MBT 5 km/h in reverse, backing up | 3.40 | 3.35 |
| 37 | Leopard MBT 5 km/h forward | 3.35 | 3.39 |
| 38 | Leopard MBT 5 km/h in reverse, backing up | 3.48 | 3.44 |
| 39 | Leopard MBT 5 km/h forward | 3.12 | 3.51 |
| | Average of Leopard MBT 5 km/h | 3.34 | 3.42 |
| 40 | Leopard MBT 5 km/h with PLANKS in reverse, backing up | 3.52 | 3.62 |
| 41 | Leopard MBT 5 km/h with PLANKS forward | 3.73 | 3.58 |
| | Average of Leopard MBT 5 km/h with PLANKS | 3.63 | 3.60 |
| | Average of dynamic surplus | +9% | +5% |

cillation exceeded 2 mm, with a maximum deflection of 2.5 mm. The same surplus was +58–59% for an empty trailer and only +9% for a tracked main battle tank (with an amplitude of 0.6 mm). In the case of the trailer, the large dynamic surplus was due to the fact that the planks simulating road defects, laid 3 m apart, corresponded to twice the trailer's rear wheelbase, so that the odd and even axles of the axle line alternately got stuck on the plank obstacles at the same time.

The greatest bridge vibrations were caused by load position 12, which involved an agricultural tractor traveling at 20 km/h over plank obstacles. *Figure 9* illustrates the vibration of the main girder of the oscillating bridge after unloading and its temporal damping. The frequency of the vibration, calculated from this longer reference sample, was 4.83 Hz, which can be considered the natural frequency of the bridge.

**Fig. 9:** *The damping phase of the mid-span vibration of the main girder on an unloaded bridge following the passage of an agricultural tractor at a speed of 20 km/h over an uneven road surface (edited by the authors)*

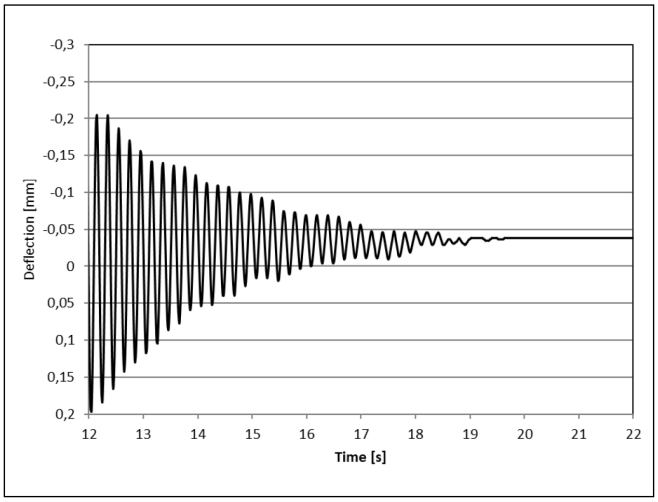


Based on the results of the test loading, it can also be concluded that the deformations of the bridge quadrants are slightly influenced by the direction of travel of the loading vehicle. In the direction of travel, the deflection of the span quadrant first subjected to the load is typically smaller than that of the quadrant subjected to the load a second time. The reason for this is that the cross-section of the second-affected quarter undergoes flexion before deflection, allowing for a greater deflection value to develop more easily.

For tracked load conditions, the surplus calculated as the ratio of the maximum dynamic deflections to the static load-bearing capacity is shown in Table 3. A detailed analysis of this is lacking due to the absence of tests at higher speeds, which, in the case described, were not carried out for technical reasons. At low speeds, the maximum measured value of the dynamic surplus was 1.08.

According to the original statical calculations (KPM Sz. HI/I-56 R, 1956) for the bridge and the current Hungarian technical regulations (e-UT 07.01.12:2011) define the dynamic factor as a function of the span length (L), consistent with the standard used in bridge design:

$$\mu = 1{,}05 + 5 / (L + 5) = 1{,}05 + 5 / (37 + 5) = 1{,}169$$

The dynamic factor measured during the test load was half

**Table 3:** *Measured dynamic factor of the crawler track at the mid-span cross-section of the bridge*

| Nr. | Load positions | | Speed | Dynamic surplus | |
|---|---|---|---|---|---|
| | | | | Average | max |
| 26 | Static | Leopard MBT in axis, in middle of span | 0 km/h | 100% | 100% |
| 36-39 | Dynamic | Leopard MBT 5 km/h (average) | 5 km/h | 101% | 108% |
| 40-41 | Dynamic | Leopard MBT 5 km/h with PLANKS (average) | 5 km/h + PLANKS | 107% | 114% |

of this value. The dynamic effect measured using plank obstacles simulating extreme road defects also remained below the standard value, whereas for the same tractor, calculated based on the static reference value, it was 1.85, and for the empty trailer, it was 1.63. Both wheeled vehicles significantly exceeded the value specified in the standard, because the standard applies to road surfaces of normal smoothness.

# 8. CONCLUSIONS

The bridge load testing conducted using military vehicles provided useful data and results for the military load-bearing capacity assessment of road bridges. Both the type of bridge structure tested (reinforced concrete, arch bridge) and the measurement technique used (displacement measurement) represent a novelty. This study presented the key results of the experimental load test of existing concrete arch bridge.

The tests confirmed that, compared to wheeled vehicles, the dynamic impact caused by tracked vehicles on reinforced concrete bridges is significantly more favourable, which allows for the use of lower dynamic factors. This increases the verifiable service load-carrying capacity of existing road bridges, thereby enhancing military mobility.

The load test demonstrated that, when evaluating tracked vehicles, only half of the dynamic factor used for wheeled vehicles needs to be considered.

The 60-year-old bridge structure under investigation behaved significantly stiffer than expected based on preliminary calculations.

The bridge's deformations were perfectly elastic; there were no permanent deformations, and any apparent residual deformations remaining after certain load conditions were all eliminated upon reloading the bridge.

It is recommended to continue the research that has been initiated, primarily by supplementing the dynamic measurements with crawler-based tests at various speeds. It is also advisable to extend the research to other structural systems (e.g., prefabricated prestressed bridge girders) and military vehicles traveling in convoys. The test loading results and further research findings are recommended for the attention of military transportation specialists.

# 9. ACKNOWLEDGEMENTS

This research would not have been possible without the support of the Hungarian Defense Forces, Cardium Ltd. and FAÉK Méréstechnika Ltd. This report is an edited version of the Hungarian-language summary (Hajós, 2025b).

# 10. REFERENCES

AEP-3.12.1.5 NATO Standard Military Load Classification of bridges, ferries, rafts and ve-hicles. Edition B Version 1, November 2024.

e-UT 07.01.12:2011 Erőtani számítás, Közúti hidak tervezése (KHT) 2. https://ume.kozut.hu/dokumentum/205 (letöltve: 2025. 04. 04.)

Everitt, A. (2019). Dynamic load effects of tracked and wheeled military vehicles from bridge load testing. A Thesis Submitted to the Division of Graduate Studies of the Royal Mil-itary College of Canada, MASc Thesis Document;

Everitt A., Wight, G. & Dagenais, M. (2019). Dynamic Load Allowance for Military Tracked and

Wheeled Vehicles: Experimental Results. International Conference on Military Technologies (ICMT) 2019 May 30 – 31, 2019, Brno, Czech Republic.

Everitt, A., Dagenais, M. & Wight, G. (2023). Comparative Dynamic Load Effects of Tracked and Wheeled Military Vehicles on Bridges. Bridge Engineering, 2023, 28(11): 04023085 https://doi.org/10.1061/JBENF2.BEENG-6394

Hajós Bence (2023). Szempontok és javaslatok a közúti hídtervezés hasznos ideális jármű te-herszintjének meghatározásához a készülő új Útügyi Műszaki Előírásban. Útügyi Lapok, 11(18) https://doi.org/10.36246/UL.2023.2.03

Hajós Bence (2024a). Paradigmaváltás a közúti hídtervezésben a hasznos járműterhek vonat-kozásában Katonai alapterhek helyett polgári járműterhek bevezetéséről. Műszaki Katonai Közlöny, 34(2) pp. 5-16. https://doi.org/10.325 62/mkk.2024.2.1

Hajós Bence (2024b). A közúti hidak dinamikus tényezőjének csökkentési lehetőségei túlsúlyos civil járművek és nehéz katonai szállítások esetén. Útügyi lapok, 2024(19), https://doi.org/10.36246/UL.2024.1.03

Hajós Bence (2025a). Kísérleti célú közúti híd próbaterhelés Leopard 2A7HU harckocsival. Haditechnika, 59(3), 52–55 https://doi.org/10.23713/HT.59.3.10

Hajós Bence (2025b). Vasbeton közúti híd kísérleti célú terheléses vizsgálata katonai járművekkel. Hadtudomány, XXXV(3) 71-85 https://doi.org/10.17047/HADTUD.2025.35.3.71

Kosmatka, J. B. (2011). "Dynamic behaviour of the composite army bridge (CAB): Field test-ing." In Proc., 8th Int. Conf. on Structural Dynamics, EURODYN 2011, edited by G, Roeck, 1559–1565. Leuven, Belgium: Katholieke Universiteit Leuven.

Kovács Ferenc (2004). Egyes közlekedésfejlesztési feladatoknak a NATO Biztonsági Beruhá-zási Programjába történő integrálása lehetőségének vizsgálata. tanulmány a Gaz-dasági és Közlekedési Minisztérium részére, Actual Mérnökiroda Bt. Budakeszi, 2004 p. 117.

KPM Sz. HI/I-56 R Közúti hídszabályzat. 1956 https://hidak.hu/konyvek/KHSZ1956.pdf (letöltve: 2025. 04. 04.)

Lenner, R. (2014). Safety Concept and Partial Factors for Military Assessment of Existing Concrete Bridges. PhD dissertation, Universität Der Bundeswehr München, Fakultät für Bauingenieurwesen und Umweltwissenchaften;

Pinkney, B., Dagenais, M. & Wight, G. (2022). Dynamic load testing of a modular truss bridge using military vehicles. Engineering Structures. 254. 113822. https://doi.org/10.1016/j.engstruct.2021.113822

Robinson, M. J. & P. E. Kosmatka. (2011). "Experimental dynamic response of a short-span composite bridge to military vehicles." J. Bridge Eng. 16: 166–170. https://doi.org/10.1061/(ASCE)BE.1943-5592.0000134

**Bence Hajós** (1978) He received his MSc in Civil Engineering from the Technical University of Budapest. Until 2014, he was involved in the operation and maintenance of road and railway bridges. He is currently a private engineer and bridge inspection expert. His main areas of research include the assessment of bridge load-bearing capacity, existing bridges, overloaded traffic, and the history of bridges. Email: elsolanchid@elsolanchid.hu

**Ákos Kővári** (1987) M.Sc. in Structural Engineering (Faculty of Civil Engineering, Budapest University of Technology and Economics, 2011); Lead Bridge Design Engineer (AlfaConsult Design and Consulting Ltd.) Field of interest: bridge and structural design, bridge building with low carbon footprint, reinforced concrete and steel structures, standardization issues. Young Engineer of the Year (2017) Construsoft BIM Awards (2019) Transportation Innovation Award (2023) Thesis title: "Development of Low-Carbon Bicycle Bridges", Feketeházy János Awards (Bridge designer of the Year 2025)

# FINITE ELEMENT INVESTIGATION OF THE BOND AND MECHANICAL BEHAVIOR OF GFRP BARS EXPOSED TO ELEVATED TEMPERATURES


Stefánia Mária Szél - Szabolcs Szinvai

https://doi.org/10.32970/CS.2026.1.4

*Corrosion reduces the service life of traditional steel-reinforced concrete structures. In cases where durability is critical or the structure is exposed to an aggressive environment, the use of non-metallic reinforcement may be a solution, as these materials are inherently insensitive to electrolytic corrosion. One such material is glass fiber reinforced polymer (GFRP). In addition to their excellent durability, GFRP bars are lightweight, easy to cut, and non-magnetic, making them suitable for a wide range of applications. However, for structures exposed to elevated temperatures, the relatively low glass transition temperature of the matrix material can present a problem. In this paper, the mechanical and bond behavior of GFRP bars subjected to thermal loading was investigated using numerical simulation. Nonlinear finite element models were developed in the ATENA software, where the matrix and the concrete were modeled with solid elements, while the fibers were represented as embedded line elements. Due to elevated temperature, the matrix's elastic modulus decreased, significantly reducing the efficiency of force transfer between fibers within the models, resulting in a loss of stiffness and tensile strength. Matrix properties also influence bond performance. The results showed that, with increasing temperature, the relative displacements between the concrete and the reinforcement increased progressively until a critical temperature was reached, at which bond failure occurred.*

**Keywords:** GFRP, tensile test, pullout test, thermal loading

## 1. INTRODUCTION

Composite materials are made by combining different materials. The properties of the new material are more favorable than those of its individual components. The engineering applications of FRP materials first appeared in aircraft and shipbuilding, then spread to the automotive industry, mainly due to their favorable mechanical and chemical properties. Their application in civil engineering began in the 1960s (Bank, 2006), primarily with carbon fiber products manufactured by pultrusion, which were used to strengthen reinforced concrete and masonry structures. More recently, their suitability for use as embedded reinforcement has also been investigated. Since embedded steel in reinforced concrete is prone to corrosion, this can cause serious maintenance problems, often even within the planned service life of the structure. High maintenance costs and structures exposed to aggressive environments require alternative solutions. Glass fiber reinforced polymer (GFRP) bars offer one option.

### 1.1. Mechanical behavior

GFRP bars are composite materials in which the fibers run parallel to each other in the axial direction. As a result, their behavior is anisotropic. Due to the mechanically weak matrix, the mechanical properties of FRP bars are excellent in the axial direction, while perpendicular to the axial direction, these properties are significantly worse. GFRP bars typically have a modulus of elasticity of 50-60 GPa in the axial direction, and their expected short-term tensile strength is around 1000-1500 MPa. The tensile strength also depends on the diameter of the bars, due to the so-called shear lag effect.

The essence of the shear lag effect is that the tensile force is not evenly distributed between the individual fibers of the FRP bar due to the shear deformation of the matrix (embedding material). The less rigid matrix cannot evenly transmit forces, so the outer fibers bear more stress while the inner fibers carry less load. As a result, the stress distribution within the cross-section is uneven, and this unevenness is more pronounced in larger diameter bars, thus reducing the average tensile strength. The shear lag effect in FRP bars is illustrated in *Figure 1.* During failure, the outer fibers rupture first, as they are the most loaded. For this reason, standards such as the Canadian CSA-S806 (CSA, 2012) limit the maximum cross-section of FRP bars (500 mm²) in order to mitigate the adverse effects of shear lag.

Tensile testing is a fundamental method for determining the mechanical properties of materials, a technique already employed by Leonardo da Vinci. During the test, a test specimen is subjected to tensile loading until it fails, while the force and the corresponding deformations are measured. The test must be performed accurately, as even minor inaccuracies can significantly distort the results.

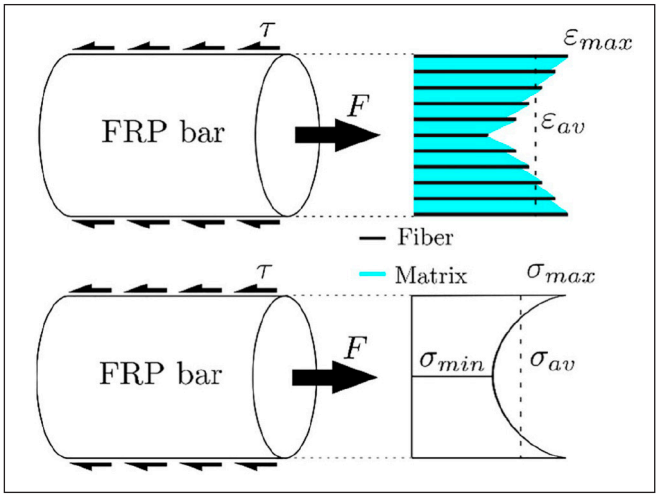


**Figure 1:** Shear lag effect in FRP bars

A special feature of the tensile test for GFRP bars is that the bar is fixed in the tensile testing machine using a steel tube filled with bedding material, which serves as an anchorage. The standards provide recommendations for the test specimen geometry (anchorage length), the measurement conditions (loading rate, temperature), and the measuring instruments (e.g., extensometer).

For FRP specimens, the most important tested parameters are typically tensile strength, elongation at rupture, and modulus of elasticity. The ASTM D7205/D7205M-06 (ASTM, 2011) and CSA S806 (CSA, 2012) standards prescribe different test methods, which can yield significant differences in results. This article is based on the test setup according to the American ASTM standard, which is the more commonly used of the two. The tensile test setup is illustrated in *Figure 2*.

## 1.2. Bond behavior

The bond behavior of FRP (fiber reinforced polymer) bars differs significantly from that of conventional steel bars, which will affect the transfer of forces, i.e., the interaction with the concrete. The bond between the concrete and the bars determines how the internal forces are transferred in the structural elements.

Bond behavior is influenced by various factors, including material inhomogeneity (particularly due to increased matrix content in the outer layers), surface treatment (e.g., sand-coated, ribbed, grooved), and temperature.

While in the case of steel bars, pullout failure typically occurs due to the shearing off of the concrete keys, in the case of GFRP bars, the mode of failure can be more varied and strongly depends on the surface design. Since the matrix material is weaker, pullout can occur through peeling of the

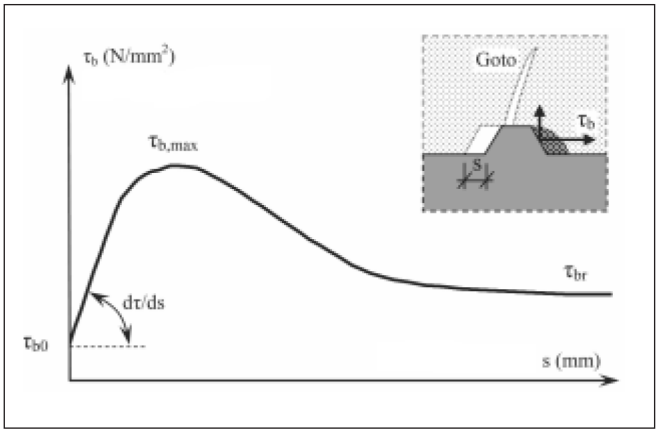


**Figure 3:** Typical bond stress-slip diagram for steel bars.

bar's surface, leading to softer behavior and reduced bond performance.

Bond is described by two main parameters: bond stress (τ), the pullout force in the bar divided by the total friction surface; relative displacement, or slip (s), the difference in displacement between the concrete and the bar under pullout loading. The result is the bond stress-slip diagram, plotted in *Figure 3*.

The purpose of the pullout test is to determine the bond properties of bars embedded in concrete (such as reinforcing steel, strands, or GFRP). During the test, the tested bar is loaded with a uniformly increasing tensile force, while the concrete test specimen is supported in some form. The measured data includes the load force, the slip on the unloaded side, and,

**Figure 4:** Standard pullout test setup (a), and examples of successful experiment (b-d)

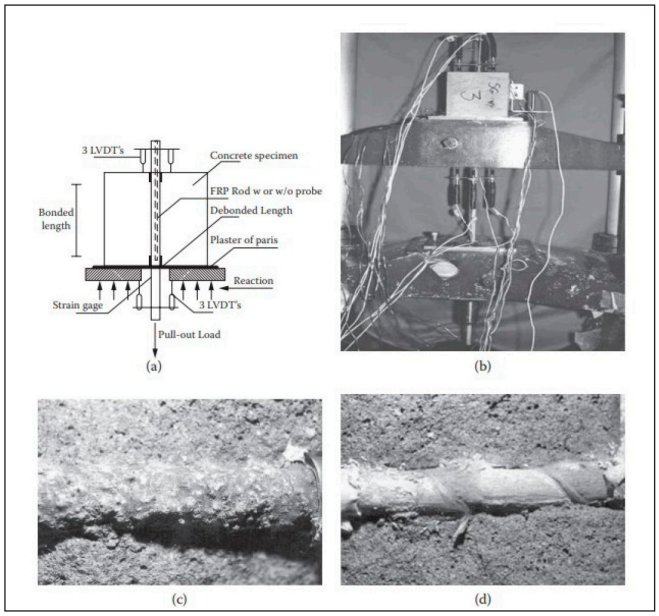


**Figure 2:** Schematic view of the standard tensile test

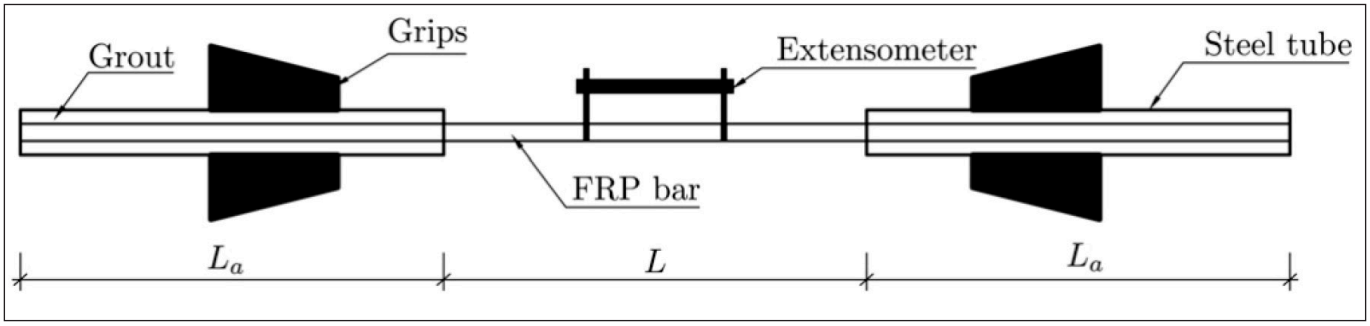

importantly, the slip on the loaded side. The results enable the determination of bond strength and allow conclusions about structural performance under actual loads.

Various international standards provide recommendations for performing the test, such as the American ACI, the Canadian CSA, and the European Eurocode. There are several types of pullout tests, including the cube, direct pullout, and beam tests. This article focuses only on the cube pullout test (an example is shown in *Figure 4*).

### 1.3. Thermal properties

During the design of structures, the effects of operating and extreme temperatures (e.g., fire-induced) must be considered, especially for reinforced concrete structures reinforced with GFRP. Elevated temperatures adversely affect the tensile and bond properties of GFRP bars.

The thermodynamic properties of GFRP, such as thermal conductivity, specific heat, and linear thermal expansion coefficient, differ significantly from those of conventional steel bars. The thermal expansion of FRP bars is directional: in the axial direction (αL), it is primarily the fibers that prevail, while in the transverse direction (αT), it is the characteristics of the matrix material that prevail. Depending on the type of FRP, these values may vary; for example, the axial thermal expansion of GFRP is ~6–10 × $10^{-6}$ °C[1], whereas in the case of CFRP, it can even be negative. Typical values are summarized in Table 1. In practice, the thermal expansion of FRP bars rarely causes problems within the operating temperature range. A more critical factor is the glass transition temperature (Tg) of the matrix material, which determines the temperature at which the composite retains its mechanical properties. The Tg value ranges from 70 to 100 °C for polyester resins, 70 to 160 °C for vinyl ester resins, and 70 to 175 °C for epoxy resins. According to standard recommendations, it is necessary to use a GFRP bar with a matrix that has a Tg at least 30°C higher than the expected maximum operating temperature. In the event of extreme heat, such as a fire, the softening of the matrix impairs the transfer of forces between the fibers, increases shear lag, and reduces the bond between the concrete and the bar. Additionally, if the bar is ribbed, an increase in temperature can reduce the ribs' stiffness, leading to greater displacements and, ultimately, failure.

**Table 1:** *Thermal expansion coefficients for FRP bars*

| | $\alpha_{cL}$ [1/°C] | $\alpha_{cT}$ [1/°C] |
|---|---|---|
| GFRP | 6...10*$10^{-6}$ | 21…23*$10^{-6}$ |
| AFRP | -2…-6*$10^{-6}$ | 60…80*$10^{-6}$ |
| CFRP | -9...0*$10^{-6}$ | 74...104*$10^{-6}$ |

## 2. PROBLEM STATEMENT

GFRP bars are often used when durability is critical or when the structure is exposed to aggressive environments. Elevated temperatures can occur in such applications, for example, due to fires in buildings, biological decomposition in sewage treatment plants, or in water pipes, such as thermal water pipes.

At high temperatures, polymer resins soften, i.e., the modulus of elasticity decreases and moisture absorption capacity increases, resulting in decreased tensile strength. In the case of GFRP bars, the decrease in modulus of elasticity significantly impairs the behavior of the bar. Softening reduces the matrix's load-transfer capacity, resulting in a more uneven stress distribution between the fibers. The average stress within a cross-section of the bar decreases, thereby reducing tensile strength. Force transfer between the concrete and the bar also occurs through the matrix, so the matrix's softening also negatively impacts bond strength.

For this reason, GFRP composites should not be used above their glass transition temperature. The glass transition temperature typically ranges from 70 °C to 200 °C, depending on the resin type. Current guidelines recommend that the operating temperature should be at least 30 °C below the glass transition temperature (ACI, 2015). The low glass transition temperature raises questions about the safe operating temperature range for GFRP bars and about how to ensure the fire resistance of GFRP-reinforced concrete structures.

This article examines the behavior of GFRP bars at elevated temperatures, focusing on their mechanical (axial tension) and bond properties.

## 3. APPROACH

Nonlinear finite element models were created in the ATENA software environment to perform the analysis. The model was constructed using the GiD general preprocessor. Two experimental setups were modeled to analyze the phenomena: a tensile test and a pullout test. In both cases, a 12 mm diameter Schöck Combar (Schöck, 2022) bar was used for modeling. During modeling, static loading was first applied until failure. In this step, verification (determining the appropriate mesh size) and validation (comparing the results with those in the literature) were performed.

In the next step, the effect of elevated temperatures was examined. For both the tensile and pullout models, the service load level (serviceability limit state) was first defined. Then, failure occurred due to a uniform increase in temperature, with deformations monitored. The properties of the resin and concrete were temperature-dependent. The temperature-dependent material properties of the resin were based on the manufacturer's data.

## 4. NUMERICAL MODELS

Two numerical models were created, one for tensile testing and one for pullout testing. In both cases, a static load was first defined, up to the point of failure. In the tensile test model, this meant fiber rupture. The pullout test model indicated pullout failure of the connection. The verification step (checking the finite element mesh and convergence) and the validation step (based on literature results) were performed for this model.

In the next step, an operational load level (serviceability load intensity) was defined in the model. Subsequently, failure occurred with a steady increase in temperature, as the matrix and concrete material models were temperature-dependent.

### 4.1. Geometry

In the tensile test setup, a 12 mm diameter bar with an approximately circular cross-section was modeled. The modeled fibers were arranged on concentric circles. One line element modeled multiple fibers. The number of line elements used was determined in the verification step *(Figure 5)*.

In the experimental setup, the free length of the test

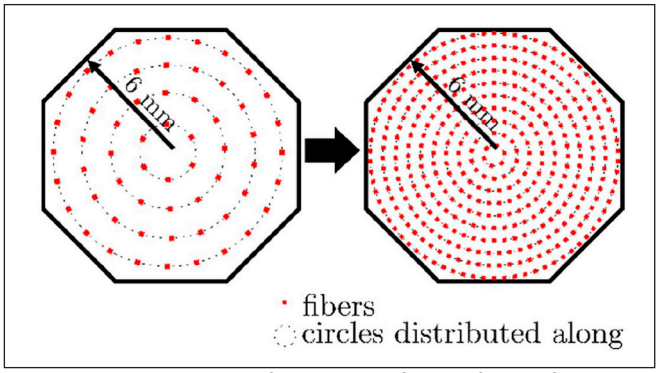


**Figure 5:** *The distribution of the modeled fibers before verification (left) and after (right) (Szinvai, 2024)*

specimen is 60 cm, and the anchoring elements on both sides are 40 cm each *(Figure 6)*. The anchoring element on the left side is defined as a boundary condition, while the anchoring element on the right side is defined as a rigid body.

In the modeled pullout test, the dimensions were those of the cube test setup, with a 5d adhesion length of 60 mm. There are several options for modeling the bar's surface, as shown in *Figure 7.* Modeling the complete geometry may yield more accurate results, but it is complex (Szinvai, 2022); therefore, the ribs of the bar were defined using the simplified geometry shown on the right side of the figure. Only a quarter of the experimental setup is included in the model, as shown in *Figure 8,* taking advantage of the symmetry conditions.

## 4.2. Material properties

The matrix was defined as a volume element with a linear elastic material model. Its modulus of elasticity was E = 3 GPa, and its Poisson's ratio was 0.4 (epoxy).

**Figure 7:** *The surface of the real GFRP bar and possible modeling solutions*

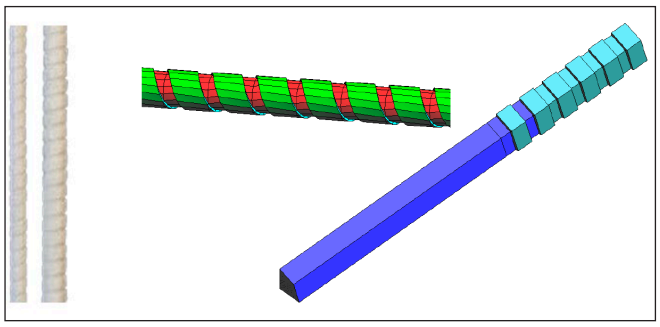

**Figure 8:** *Side view of the modeled pullout test setup.*

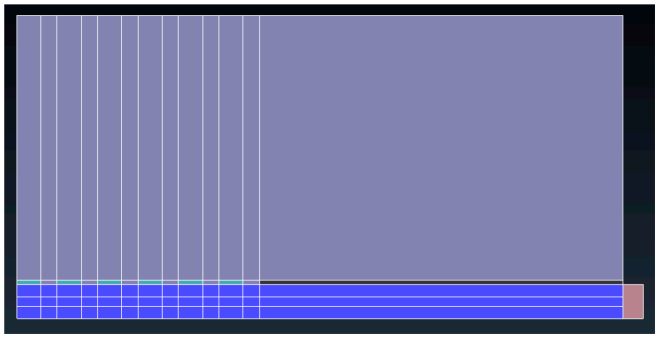

The glass fibers were defined as linear elastic line elements. The elastic modulus of the glass fiber was set to E = 80 GPa (manufacturer's data), and the given fiber distribution and fiber-to-volume ratio were used to determine its cross-sectional area.

The concrete also appears as a volume element, with a concrete grade of C50/60, its standard expected mean values, and the material model „CC3DNonLinCementitious2" defined in the program.

A frictional connection was established between the concrete and the insert, with a friction coefficient of 0.3, as determined during the validation step.

## 4.3. Boundary conditions

The boundary conditions are illustrated in *Figure 9.* In the tensile test case, the outer surface was fixed in the axial direction along the left-hand anchoring element, and support was defined transversely at a single point along the edges over the entire length to ensure model stability.

In the pullout test setup, in addition to the boundary conditions corresponding to the symmetry conditions, a load-distributing steel plate is also present on the loaded side, which is fixed in the axial direction of the embedded bar.

## 4.4. Mesh

The finite element meshes used after the verification step are shown in *Figure 10.* As shown, dense meshing was required along the bar's cross-section to model shear lag properly, and significant mesh refinement was applied along the bond length in the pullout test.

**Figure 9:** *Boundary conditions for the tensile test setup (left) and for the pullout test setup (right).*

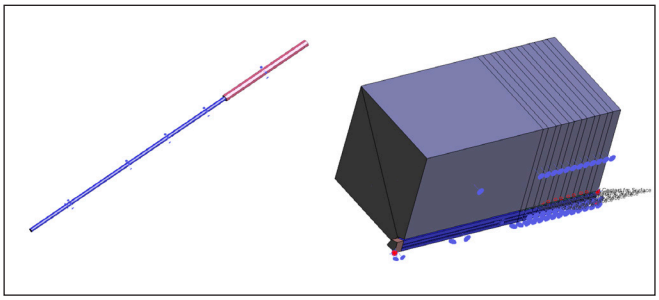

**Figure 10:** *Applied finite element mesh in the tensile test (left) and in the pullout test (right)*

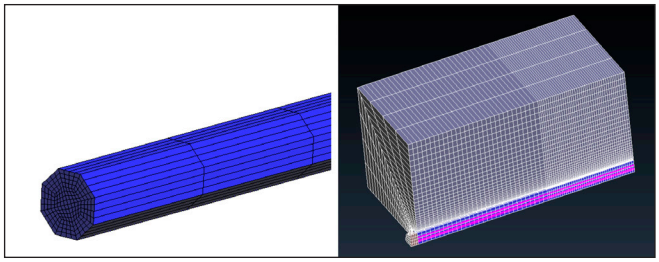

**Figure 6:** *Tensile test setup in the model.*

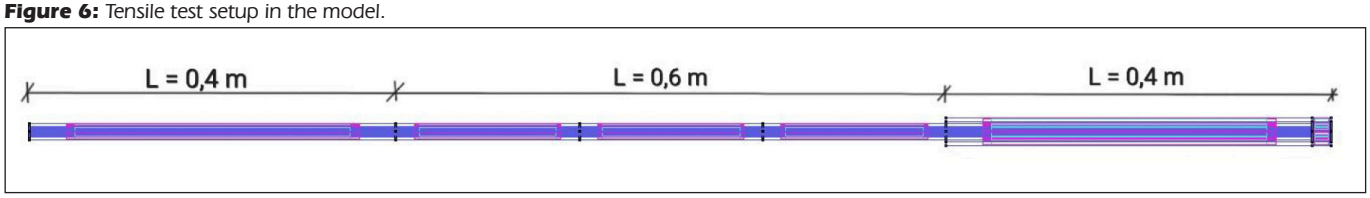

# 5. RESULTS

## 5.1. Tensile test

According to the literature, the stresses arising in the fibers increase as we move from the center of the bar toward its edge. Based on the model results, *Figure 11* shows that the shear lag effect is evident even at relatively large mesh sizes and small numbers of modeled fibers. However, a stress distribution closer to reality was only achieved after increasing the mesh density and the number of modeled fibers. At the same time, the average stress also decreased, indicating a corresponding decrease in tensile strength.

The model was not intended to determine the exact tensile strength, but rather to model the modulus of elasticity and composite behavior (shear lag effect). Under static loading, the numerical model's bar had an elastic modulus of 60 GPa, the value specified by the manufacturer.

**Figure 11:** *Tensile stresses in the modeled line elements [MPa] for decreasing mesh size*

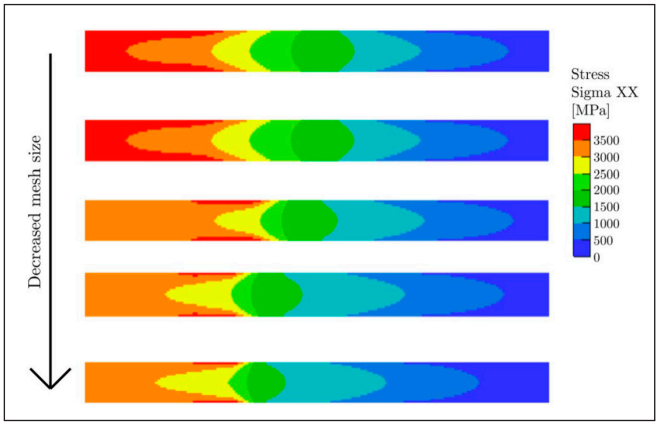


**Figure 12:** *The change of the modulus of elasticity of the matrix material in terms of temperature*

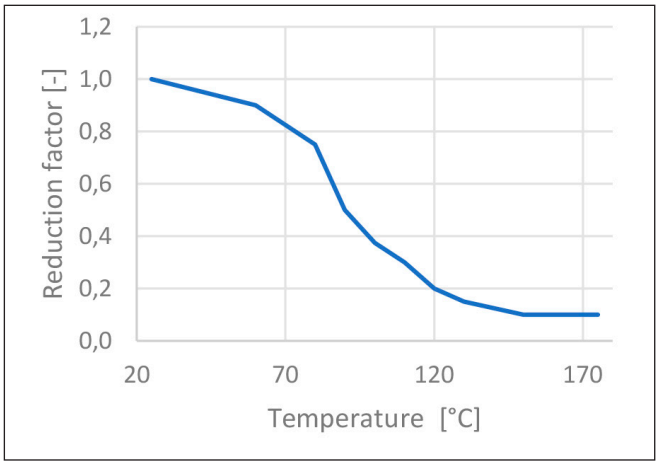


**Figure 13:** *Thermal distribution inside the cross-section*

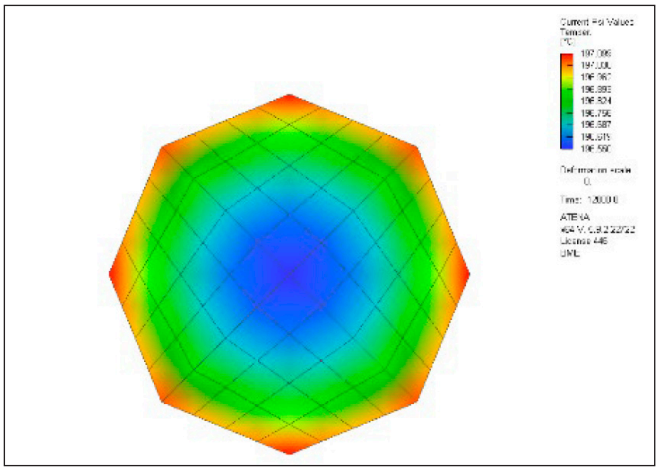

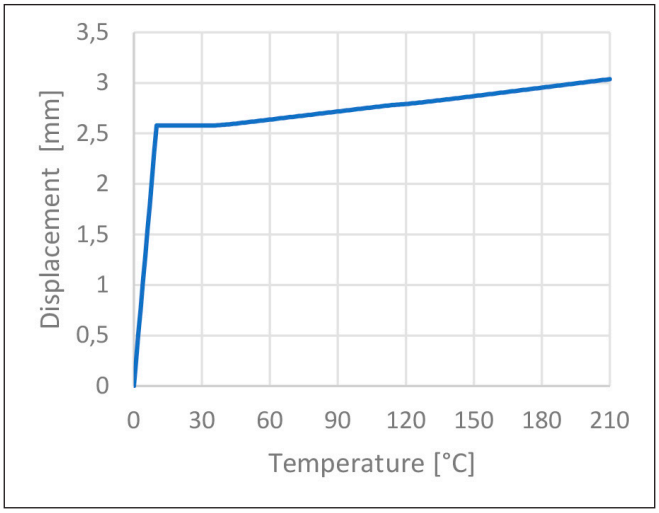


**Figure 14:** *The increase in the maximum displacement in terms of temperature loading*

After static loading, the bar was subjected to temperature loading at service load levels. The aim was to understand the fundamental mechanisms of the behavior of the GFRP bar. The model can later be used to determine the temperature-dependent strength of the GFRP bar. To do this, the tested bar must be loaded to failure at different temperatures. The test points then outline the behavior of the GFRP bar.

During the temperature load, the matrix had temperature-dependent material properties. The change in the matrix modulus of elasticity with temperature is shown in *Figure 12*. *Figure 13* shows the temperature distribution within the bar at the maximum load temperature (170 °C). As can be seen, the temperature inside the bar is still significantly lower. After this, with a further increase in temperature, where the matrix had already reached 170 °C, no further decrease in stiffness was defined, but the temperature inside the bar continued to rise.

At the same time, the displacement associated with the constant load force also increased. Due to the reduced stiffness, the displacement associated with the same load force increased. Even after increasing the load temperature to 170 °C, the displacement continued to increase because the temperature inside the bar remained significantly lower.

A redistribution of tension stresses between the fibers essentially caused the failure. The average stress remained unchanged, but the stress distribution between the fibers changed, and the stress difference between the middle and outer fibers increased (shear lag effect), indicating that the stress in the outer fiber approached its tensile strength. Failure occurred when the critical outer fiber reached its tensile strength. Failure then occurred suddenly and progressively. When the outer fiber ruptured, the load it had previously borne was transferred to the surrounding fibers, which also became overloaded; subsequently, the entire cross-section ruptured.

## 5.2. Pullout test

In the first step, the experimental numerical model was subjected to a static load until failure. The validation was based on the manufacturer's data. *Figure 15* shows the bond stress-slip diagram obtained from the numerical model compared

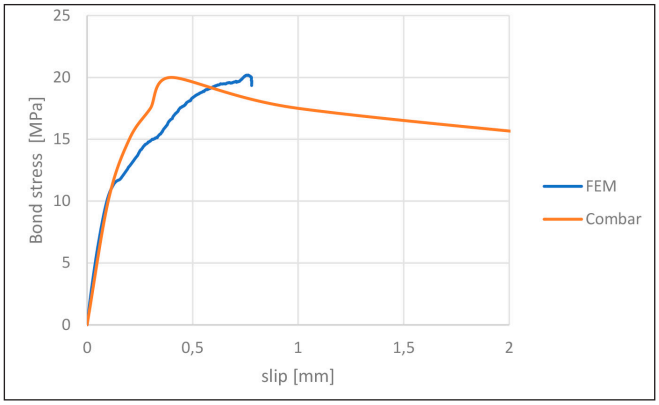


**Figure 15:** Comparison of bond stress-slip curves. Finite element results versus experimental results provided by the manufacturer.

with the manufacturer's data. It can be seen that the initial stiffness is the same. However, as the concrete keys begin to shear off, a difference develops between the numerical model and the manufacturer's experimental results. The discrepancy can most likely be explained by the smeared-crack model used in ATENA and the fixed crack direction. In the model, the cracks remained fixed after formation. The result could be further improved by modifying the crack propagation parameters (e.g., allowing crack rotation up to 20-30% of the concrete tensile strength).

To optimize the model's convergence and running time, this modification was not implemented, and the fixed crack direction after formation was used instead.

Figures of cracking validate the results obtained. *Figure 16* shows the cracks formed under low load (~20% of failure load), and *Figure 17* shows the cracks formed during pullout failure. In the latter case, the concrete keys have essentially worn away, and the bar can pull out freely (only frictional resistance remains)

After preparing the validated pullout test model, the next step was to load the model to its service load level and then apply a surface temperature load to the concrete test specimen. *Figure 18* compares the bar temperature with the

**Figure 18:** Maximum temperature inside the tested bar vs temperature loading

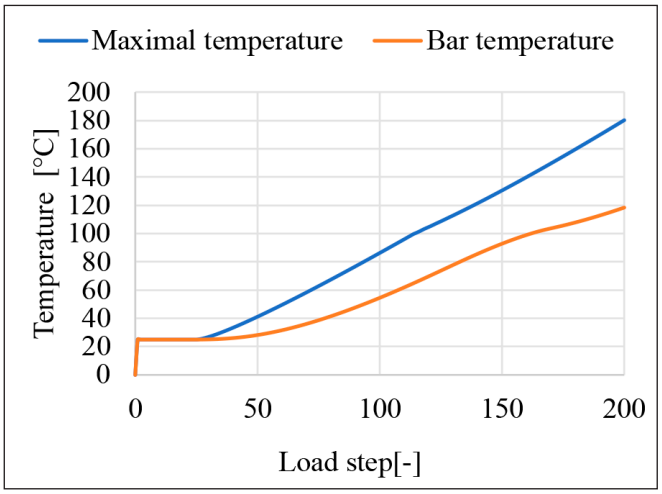


**Figure 16:** Microcracks from induced static loading, at 20% of the failure load

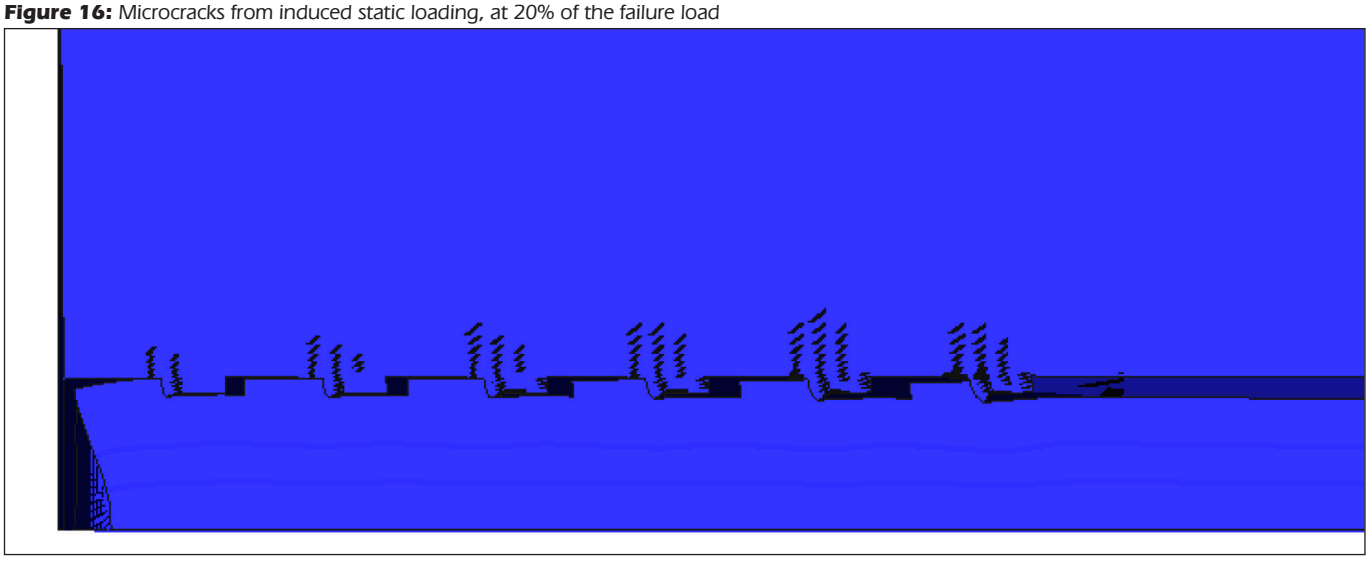

**Figure 17:** Microcracks from induced static loading, close to pullout failure

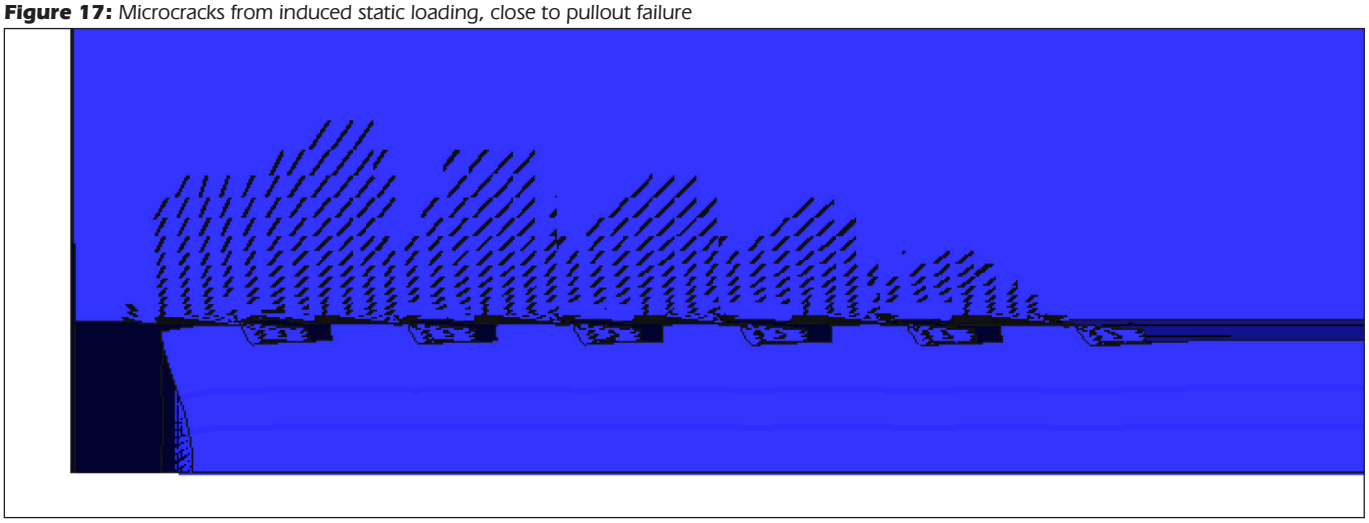

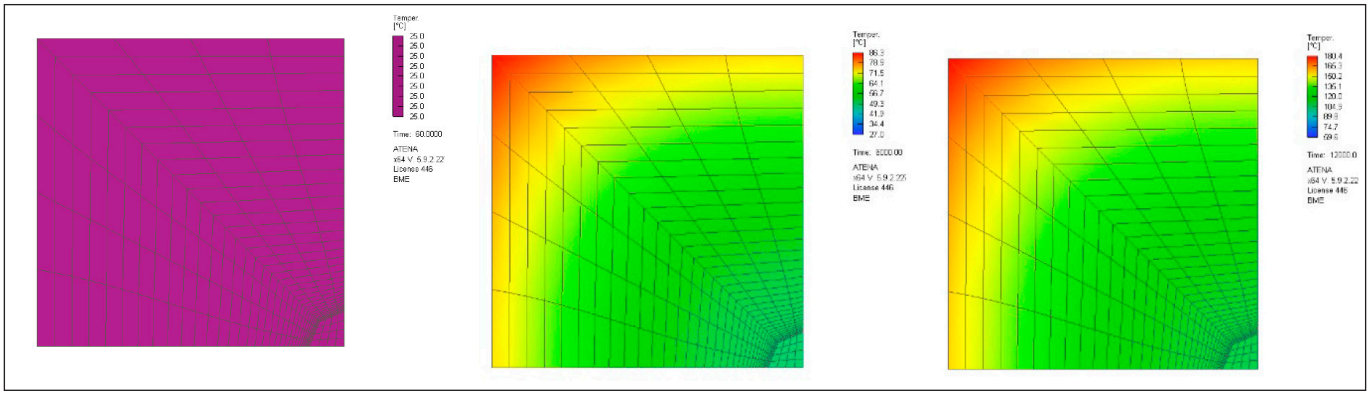

**Figure 19:** *Thermal distribution inside the concrete specimen*

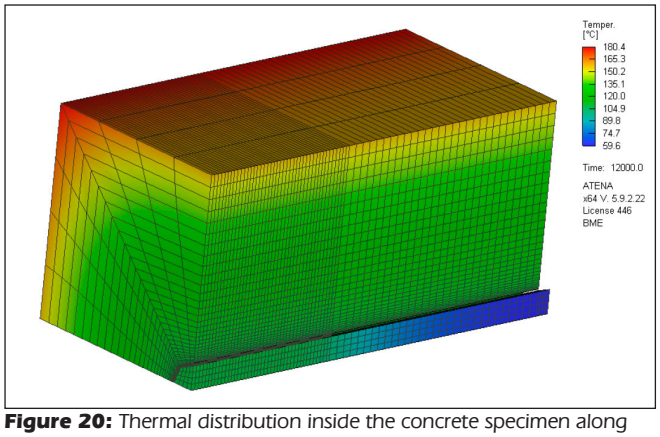


**Figure 20:** *Thermal distribution inside the concrete specimen along the axes of the tested bar*

maximum temperature during the temperature load. It can be seen that the temperature in the bar remained essentially 50-60°C lower.

During the temperature increase, the temperature distribution within the test specimen at the maximum load temperature is shown in *Figures 19* and *20.* The temperature decreased continuously as one moved towards the interior of the concrete.

As the temperature rose, the matrix and concrete materials deteriorated. *Figure 21* shows that as the temperature rose and the bond between the concrete and bar softened, the slips measured on the unloaded side also increased.

The crack pattern and stress distribution at the end of the static load are shown in *Figure 22. Figure 23* illustrates the moment of failure due to thermal load. The number and extent of cracks increased, but the failure did not occur due to the shearing off of the concrete keys; instead, it was caused by the softening of the ribs of the GFRP bar. At sufficiently high temperatures, the ribs became so soft that the bar slipped out of the concrete test specimen, with only friction providing residual resistance.

## 6. CONCLUSIONS

The use of GFRP bars is becoming increasingly common in applications where durability is important or where structures are exposed to aggressive environments. Due to their material composition, GFRP bars are immune to electrolytic corrosion. However, the application of GFRP bars is complicated by problems arising from the low glass transition temperature of the matrix material. Concrete structures made with GFRP bars can be exposed to high operating temperatures or extreme fire conditions. In that case, the suitability of GFRP becomes questionable, or special thermal insulation and heat-resistant materials may be required.

In this article, the two most important properties of GFRP bars were examined: mechanical and bond properties under service load levels, with a uniform increase in temperature. To perform the test, nonlinear finite element models were created in the ATENA software environment, in which the matrix and concrete were modeled using volume elements, and the fibers were represented as embedded line elements. Two experimental setups were examined: a tensile test and a pullout test. In both cases, the subject of the investigation was a 12 mm-diameter GFRP product called Schöck Combar, which has a grooved surface.

The results showed that, under a constant tensile force,

**Figure 21:** *Increase in slip from thermal loading*

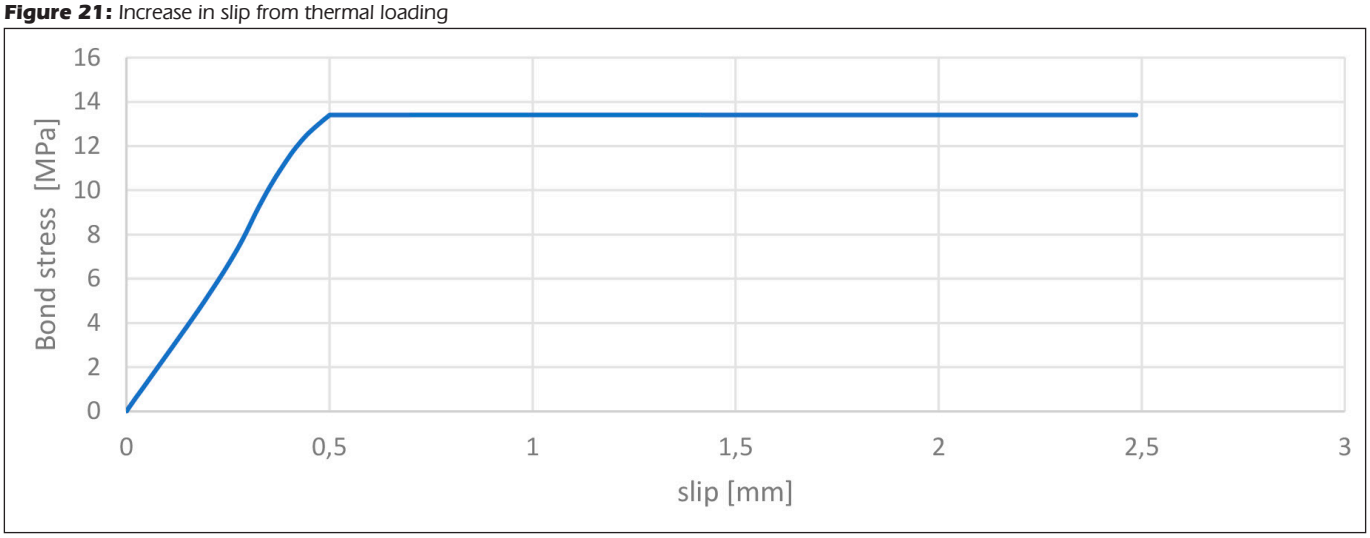

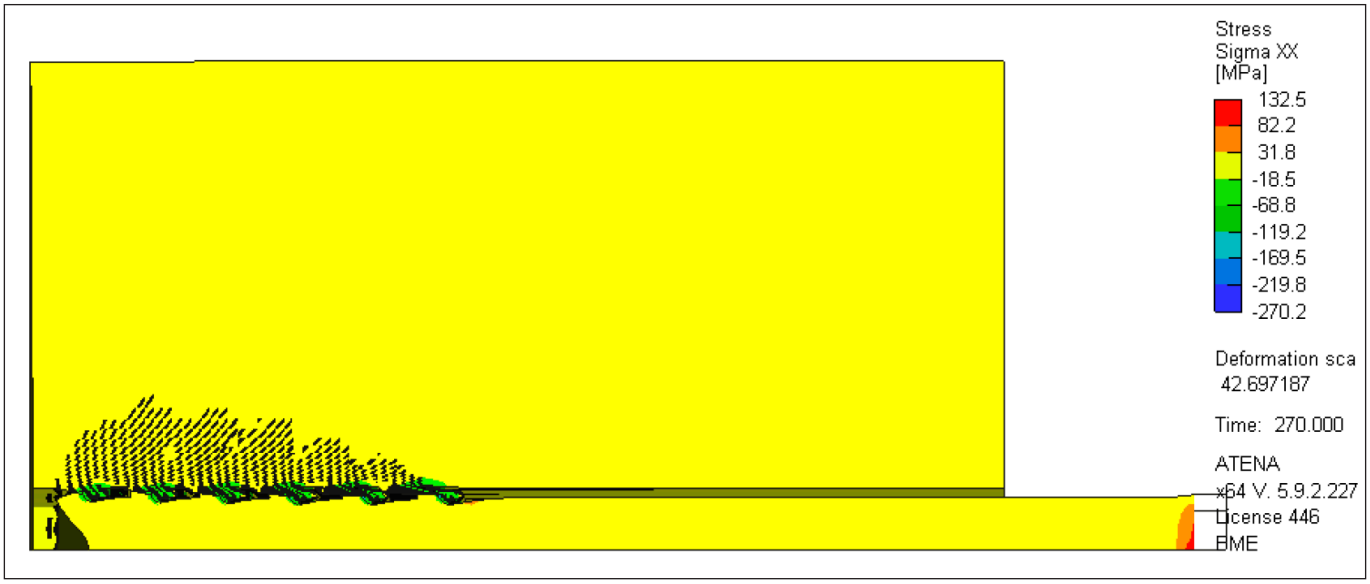


**Figure 22:** *Cracking and stress distribution inside the specimen after static loading*

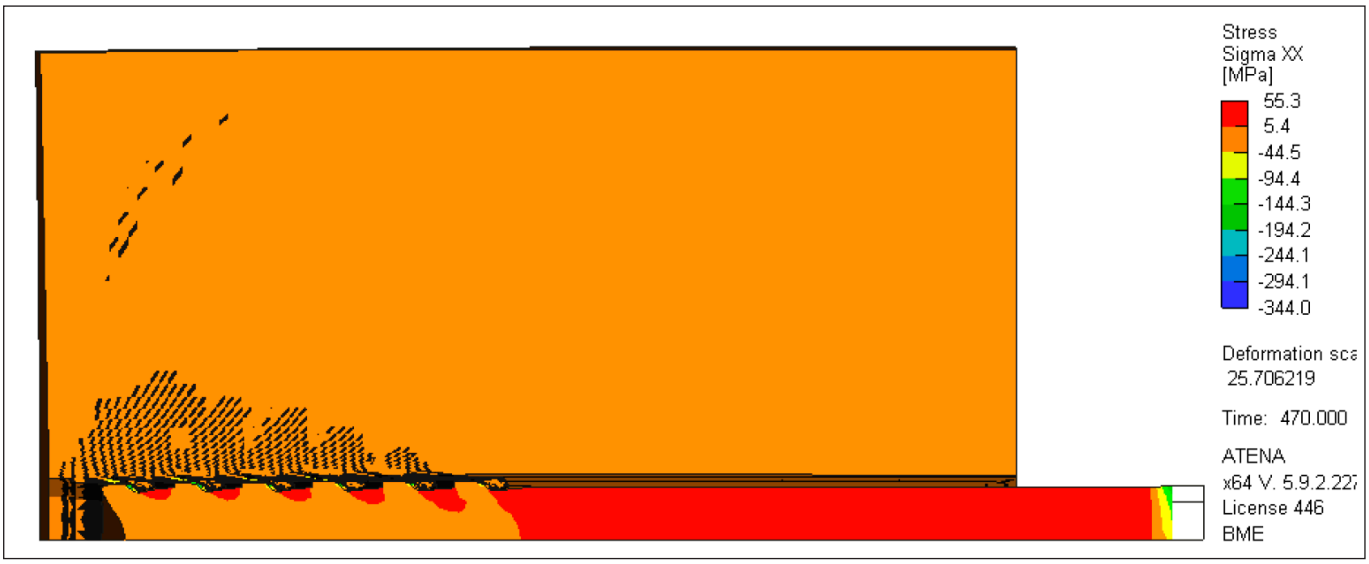


**Figure 23:** *Cracking and stress distribution inside the specimen close to failure caused by thermal loading*

the average stress across the bar's cross-section remained constant as the temperature increased. However, a decrease in the matrix modulus of elasticity increased the shear lag effect, i.e., the stress difference between the middle and the most loaded outer fibers increased. Thus, as the temperature increased further, the stress in the critical edge fiber increased, and when it reached the fiber's tensile strength, progressive failure occurred, ultimately leading to the entire cross-section rupturing.

During the pullout test, the bar ribs were modeled using simplified volume elements. The simplification enabled examination of the effect of softening the GFRP ribs as the temperature increased. As the temperature increased, the connection's stiffness decreased, and slippage on the unloaded side increased continuously. The cracks also widened and spread in the concrete, but unlike under static loading, failure did not occur due to the shear failure of the concrete keys; instead, it was caused by the peeling off of the GFRP ribs. After the ribs lost their stiffness, the bar slipped out of the concrete, with only friction providing residual resistance.

Overall, the validated numerical models were suitable for investigating the behavior of the GFRP bar under temperature loading. Further validation of the results is necessary through laboratory testing, and further investigations can be carried out using the models created to enable the use of GFRP bars under higher or extreme temperature loads.

## ACKNOWLEDGEMENTS

This article presents my Master's Thesis, submitted and defended in 2025, and summarizes its objectives, solution mechanism, and conclusions. I would like to thank Szabolcs Szinvai for agreeing to be my supervisor and for encouraging and supporting my work throughout the semester, enabling me to get the most out of the topic.

## REFERENCES

Bank, L., C. (2006). „Composites for Construction." *John Wiley & Sons*, https://doi.org/10.1002/9780470121429

CSA, S806-12. (2021). „Design and Construction of Building Components with Fiber-Reinforced Polymers." *Canadian Standards Association*

ASTM, D7205/D7205M. (2011). „Test Method for Tensile Properties of Fiber Reinforced Polymer Matrix Composite Bars." *American Society for Testing and Materials*

ACI, 440.1R. (2015). „Guide for the Design and Construction of Structural Concrete Reinforced with Fiber-Reinforced Polymer (FRP) Bars." *American Concrete Institute*

Schöck. (2022). „Combar Brochure." *Schöck Bauteile GmbH*
Szinvai, S., & Kovács, T. (2024). „Numerical modeling of the shear lag effect in GFRP as function of fiber content." *Pollack Periodica*, 20(2), 1-7, https://doi.org/10.1556/606.2024.01049
Szinvai, S., & Kovács, T. (2022). „Numerical modelling of the bond behaviour between uncracked concrete and deformed steel and fibre reinforced polymer bars." *Proceedings of the 14th fib International PhD Symposium in Civil Engineering*, 621-628, https://www.fib-international.org/publications/fib-proceedings/14th-phd-symposium-in-rome-italy-2022-proceedings-em-pdf-em-detail.html

**Stefánia Mária Szél (**2000**)** civil engineer, Acélhidak Kft. Quality Control Department (MEO). Graduated from the Structural Engineering Department at the Budapest University of Technology and Economics in 2025. Main areas of interest: bridge design and construction, with a particular focus on practical issues, bridge construction and inspection during manufacturing.

**Szabolcs Szinvai** (1997) civil engineer, PhD student, BME Structural Engineering Department. Main areas of interest: the application of fiber reinforced polymers in concrete structures, with a focus on bond-related issues and structural behavior. Head of the Young Member Group of *fib* HU (International Federation of Concrete), member of *fib* TG10.3 and TG5.1 working groups.

# DEVELOPMENT OF A SIMPLIFIED MULTILINEAR SPRING MODEL FOR HYBRID BOLTED CONNECTIONS USED IN PRECAST REINFORCED CONCRETE BEAM ASSEMBLIES


Wael Hameedi - István Völgyi

https://doi.org/10.32970/CS.2026.1.5

*The overall structural behaviour of precast systems depends not only on its members strength, but also on the stiffness and deformability of their connections, modelling the precast connections is of a great important to reflect the real behaviour of the structure, 3D finite element representation of the bolted connections were widely adopted in previous research, such detailed method are often complicated and time consuming, in this context, the present paper proposes a simplified modelling approach in which bolted connection are represented by spring elements. An experimental program was conducted to measure the separation at the bolted connection level and to draw the corresponding nonlinear load-separation relationships. Based on the experimental results, simplified multilinear spring models were developed to reflect the tensile behaviour of the investigated bolted connection in a form suitable for structural analysis. This spring model was validated using ANSYS finite element software. A parametric study was also conducted to further validate the spring model and demonstrate the effect of increased initial imperfections on the global behaviour of the assembled beam. while the ultimate load remains almost unchanged. Larger bolt diameters showed better tolerance to assembly imperfections. The proposed spring models can therefore be used as a practical tool for structural analysis and design of hybrid precast connections.*

**Keywords:** precast structures, hybrid bolted connection, initial imperfection, spring element, finite element analysis

## 1. INTRODUCTION

Precast concrete (PC) building system has a number of distinct advantages in the form of faster construction rates, better quality control through manufacturing processes, and better cost efficiency in terms of reduced material wastage, faster construction rates, and lower safety risks during construction (Elliott, 2019; Psycharis & Mouzakis, 2012). These attributes often result in lower overall construction costs compared to traditional cast-in-place reinforced concrete (RC) building systems(Yuksel et al., 2015) .

The performance of precast structures depends greatly on their joints, which play a key role in enabling rapid erection, demountability, and effective load transfer across member interfaces. For a structure assembled from such precast reinforced concrete members, the overall behaviour of the structure in the frame is not only governed by the strength of the individual members but also by the stiffness and deformability of their joints (Bao & Tan, 2023; Holly & Abrahoim, 2020; Taher et al., 2015) . For design purposes, joints are usually considered either pinned or rigid; however, previous investigations have shown that structural connections, exhibit reduced performance under service and ultimate loading due to various factors (W. S. Hameedi & Völgyi, 2025; Zhong et al., 2019). Therefore, using an idealized joint condition may lead to an inaccurate representation of frame stiffness, redistribution of internal forces, and stability-sensitive behaviour. Hybrid bolted connections have become an increasingly attractive method for assembling precast concrete members because they combine fast construction with more efficient force transfer between the assembled members(Pham et al., 2024; Qing et al., 2022; Wang et al., 2020; Yrjölä & Kinnunen, 2023). However, when their structural behaviour is investigated numerically, detailed three-dimensional models for connections are usually required to represent the complex interaction between its components (Yang et al., 2025). Such models are often time-consuming and computationally demanding. Therefore, a simplified representation of the bolted connections as a spring element provides a more practical alternative, as it can capture the essential connection behaviour while being easier to incorporate into analytical and numerical studies.

This study aims to develop simplified spring models capable of representing the realistic response of hybrid bolted precast assemblies while accounting for the influence of anchor-bolt diameter and initial assembly imperfection on both the initial stiffness and the ultimate behaviour of the assembly. In addition, the proposed spring models are verified through a simple finite element model to evaluate their applicability as a practical alternative to the explicit modeling of complex three-dimensional bolted connections. The developed modeling approach is further used as a parametric tool to generate

the global load-deflection response of the assembly under different imperfection levels.

## 2. EXPERIMENTAL OVERVIEW

An experimental test was carried out to evaluate the local tensile force-separation behaviour of hybrid bolted beam-to-beam connections used in precast reinforced concrete members, where the local separation is the horizontal displacement measured at the bolted connection level with a fixed gauge length of 60 mm. The aim is to capture the response of the bolted joint under flexural loading, with particular attention to the influence of assembly condition on the local connection behaviour. For this purpose, full-scale assembled beam specimens were tested previously by the authors under monotonic four-point bending, while the local opening at the joint was monitored directly at the bolted connection level. A total of six assembled specimens were investigated. The specimens were grouped according to the diameter of the anchor bolts used in the lower tensile zone of the joint, namely 16, 20, and 24 mm. For each bolt size, two assembly conditions were considered: a perfect configuration and an imperfect configuration. Accordingly, the test series consisted of specimens A16, B16, A20, B20, A24, and B24. In this notation, the letter A denotes the perfectly assembled configuration with zero face rotation, whereas the letter B denotes the imperfect configuration in which a controlled initial face rotation of 1.2° was introduced during setup. This matrix enabled examination of both the effect of bolt size and that of assembly imperfection on the local joint response. Each specimen consisted of two precast reinforced concrete beam segments connected at midspan through a hybrid bolted connection and a grouted joint, as shown in *Fig.1*. The lower part of the joint contained the structural anchor bolts responsible for transferring the tensile force generated by bending, while the upper part of the section mainly carried compressive stresses. The tested arrangement was selected to represent the actual force-transfer mechanism in the connection region under bending-dominated loading. Since the present study focuses on the development of a realistic spring-type representation of the bolted connection, the local force-separation behaviour of the tension side of the joint was treated as the key experimental output. The specimens were tested using a four-point bending setup under monotonic loading. This loading arrangement created a constant-moment region around the joint and allowed the tensile behaviour of the bottom bolted connection to be observed in a controlled manner. To monitor local joint opening, linear variable differential transformers (LVDTs) were positioned at the bolted connections positions on both sides of the joint.

These sensors measured the relative separation occurring at the tensile side of the connection. To reduce the influence of possible local asymmetry and obtain a representative local response, the average value of the two LVDT readings was used in the analysis. Thus, the reported separation response corresponds to the mean opening measured at both sides of the bolted connection. The adopted test program was therefore designed to provide the experimental basis for relating the tensile force in the connection to the corresponding local separation, while accounting for two practical assembly conditions: perfect alignment (0°) and a first-level imperfection (1.2°), where the degree of imperfection refers to the beam's face upward inclination at the joint region. . To draw a local response of the bolted connection, the applied load converted to equivalent local tension force on the anchor bolt by employing simple equilibrium, the experimental results are shown in *Fig. 2*. More detailed information about the layouts of the reinforcement and the bolted connection components can be found in the author's previous study (W. Hameedi & Völgyi, 2026).

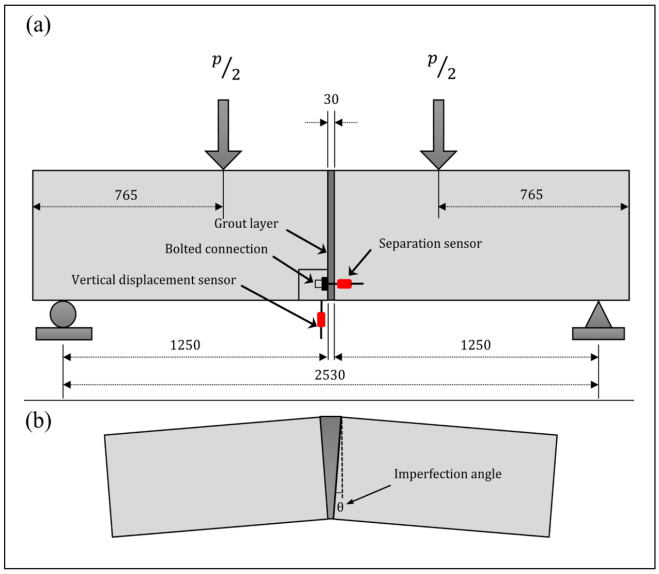


**Fig. 1:** *Experimental test setup and definition of the initial imperfection, (a) test configuration, (b) schematic representation of the initial imperfection*

## 3. DEVELOPMENT OF SIMPLIFIED SPRING MODELS

Based on experimental test measurements, simplified spring models were developed to represent the tensile behaviour of the investigated hybrid bolted connections, in a form suitable for design-oriented structural analysis. The load-separation response measured at the connection level was converted into an equivalent anchor-bolt tension force-separation relationship using simple sectional equilibrium. In this procedure, the applied load was converted to bolt tension force by assuming a constant lever arm between the resultant compressive force and the anchor bolts in tension. In this way, a simplified nonlinear spring relationship was established for each specimen type. The obtained nonlinear spring models showed that geometric imperfections mainly affected the initial tensile stiffness of the connection, while their influence on the yield and ultimate load capacity levels remained non-significant. For practical structural applications, the nonlinear spring relationships were further simplified into multilinear spring models, which provided sufficiently close fitting to the experimental nonlinear response while being easier to implement in structural analysis and design models. Therefore, the proposed spring models offer practical input for designers who require to simulate the realistic deformation behaviour of such hybrid precast joints in global frame analysis and connection assessment. The proposed multilinear spring models for the tested specimens are presented in *Fig. 3*.

Based on the multilinear models illustrated in Fig. 3(a), equations are constructed to calculate the stiffness for each segment of each bolt diameter and each imperfection level, a nonlinear regression analysis was used to relate the segment stiffness to bolt diameter. Specifically, a polynomial was used

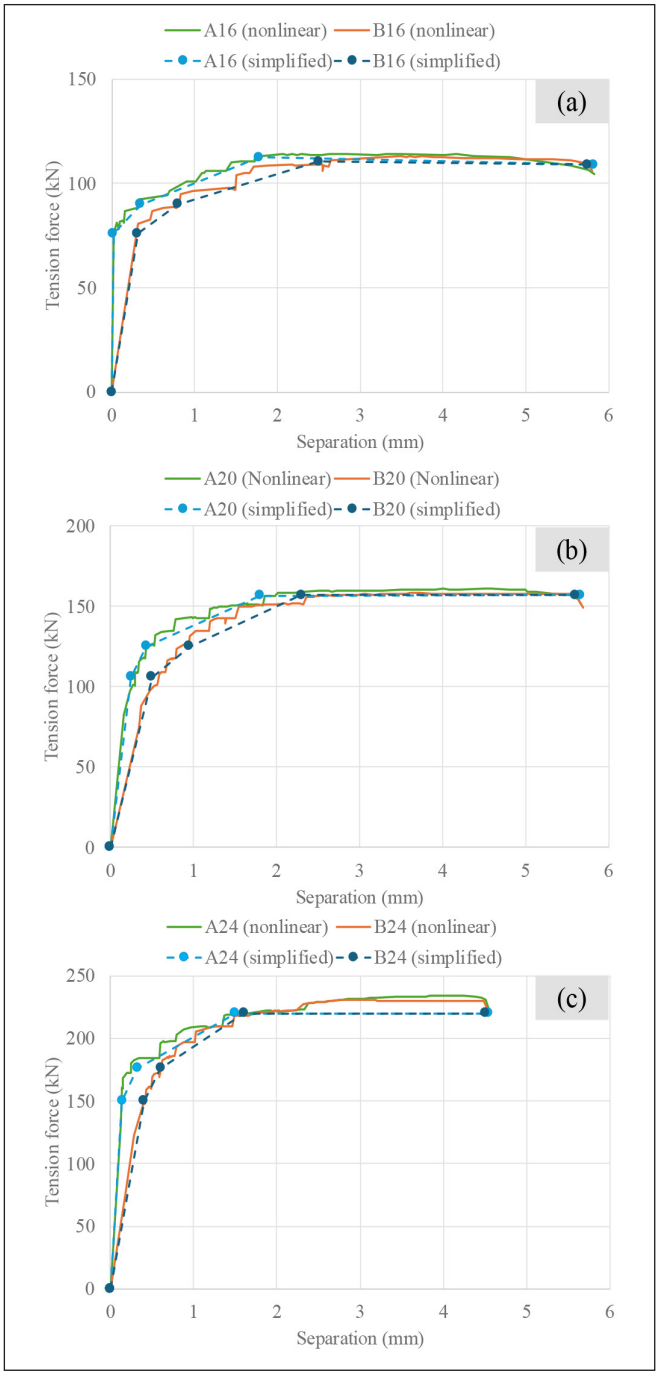


**Fig. 2:** Experimental test results with multilinear fitted curves for the perfect and imperfect configurations: (a) 16 mm, (b) 20 mm, and (c) 24 mm bolt diameters.

for all the segments with R2 approximately close to 1, as it better captured the non-monotonic difference in initial stiffness across the three bolt diameters. as described in equation

$$k(d,i,s)=\begin{cases}(121.52-115.46i)\cdot d^2+(-5185.12+4959.34i)\cdot d+(55517.5-53212.9i)\\(-0.6419+2.9488i)\cdot d^2+(38.3834-118.02i)\cdot d+(-407.0242+1119.5843i)\\(0.213+0.0653i)\cdot d^2+(-5.8103-1.3292i)\cdot d+(54.0416+1.0033i)\end{cases}$$

Where:

$k$: required segment stiffness in kN/mm

$d$: anchor bolt diameter in mm,

$i$: imperfection level (0=perfect, 1=imperfect)

$s$: segments number

It is worth noting that the proposed equations are valid only within the investigated ranges of bolt diameter and imperfection level. Additional experimental studies are required to extend and generalize their applicability beyond the tested cases.

# 4. FINITE ELEMENT MODELING

A finite element (FE) model was developed using the multipurpose FE software ANSYS 2026 R1 to validate the applicability of the proposed simplified spring models to capture the behaviour of the hybrid bolted connection. The main purpose of this numerical model was to examine whether the experimentally derived spring laws could be used as a practical alternative to the detailed three-dimensional modeling of the bolted connection components, which is generally more complex, time-consuming, and computationally demanding. In this study, the simplified spring representation was introduced into the FE model to capture the local connection deformability while allowing efficient prediction of the global and local structural response of the assembled reinforced concrete (RC) beams. The numerical model was also used as a parametric tool to investigate the influence of connection imperfection on the global behaviour represented by load-deflection response of the assembled beams. After validating the applicability of the simplified spring approach against the reference behaviour, multiple imperfection levels were introduced. In this way, the FE model made it possible to assess how different initial imperfection values affect the global response and the overall stiffness of the assembled RC beams without the need to repeatedly construct detailed local three-dimensional connection models.

## 4.1 GEOMETRY AND BOUNDARY CONDITIONS

Geometric and material nonlinearities were considered in the finite element modeling of the different components of the assembled beam. The reinforced concrete beam parts and the grout block at the joint region were modeled using the eight-node three-dimensional solid element SOLID65, which is capable of representing the nonlinear behaviour of reinforced concrete and was therefore adopted to reflect the actual stiffness of the tested beams. The longitudinal and secondary reinforcing bars were modeled using the truss element LINK180. The bolted connection at the joint was represented using the unidirectional nonlinear spring element COMBIN39, which enabled simulation of the interfacial behaviour of the connection through the tension force-separation relationships developed from the experimental tests. In the model, the COMBIN39 elements were assigned between two opposite nodes located at the exact positions of the bolted connections. The geometry of the model was defined in a global Cartesian coordinate system. The beam depth was oriented along the Y-direction, while the beam span was aligned with the X-direction. To represent the interface conditions at the joint, the COMBIN39 elements were also assigned very high stiffness values in the Y- and Z-directions. The spring in the Z-direction was used to simulate the negligible transverse relative movement at the joint, while the spring in the Y-direction reflected the restraint provided by the grout confinement. The actual horizontal interfacial behaviour of the connection was modeled by a nonlinear COMBIN39 spring acting in the X-direction, whose load-separation profile was defined to match the experimentally derived spring model corresponding to each specimen type and setup configuration, as presented previously. Regarding the boundary conditions, the supports were defined to reproduce the simply supported arrangement used in the experimental tests. At one support, translational displacements were restrained in all directions,

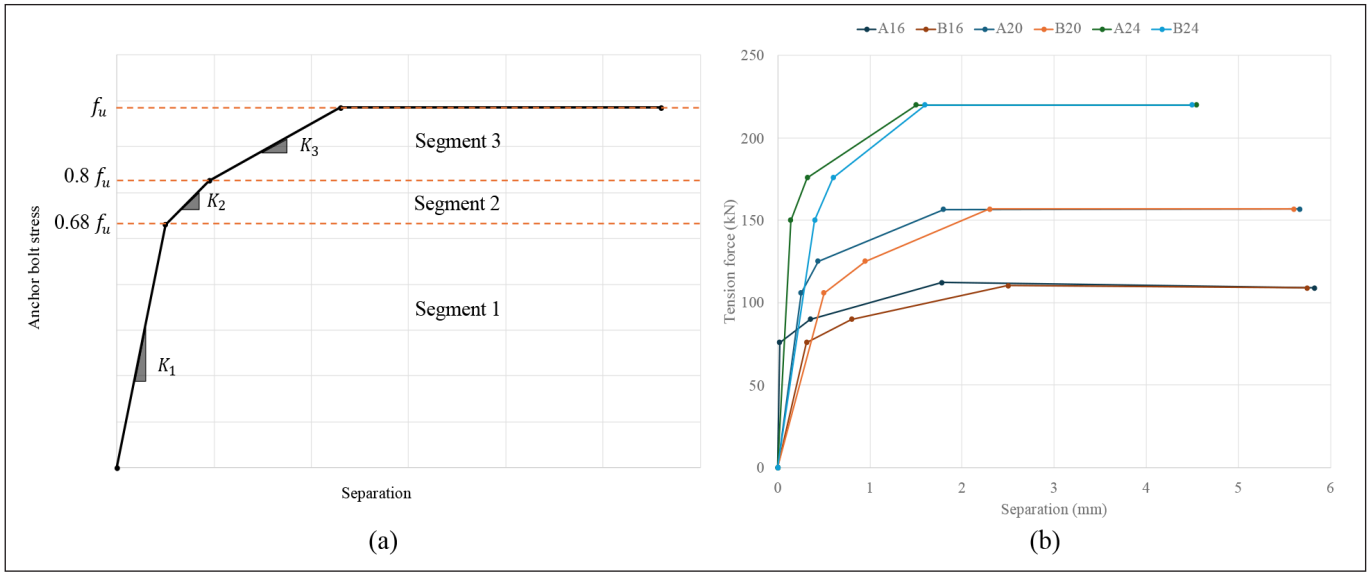


**Fig. 3:** *Simplified multilinear spring models (a) a schematic definition of the spring segments, (b) experimentally derived spring models for A16, B16, A20, B20, A24, and B24 specimens.*

whereas at the other support only the displacement in the Y-direction was restrained, allowing longitudinal movement of the beam. Loading was applied in a displacement-controlled manner in the Y-direction. The numerical analysis was terminated according to the same principle adopted in the experimental program, namely when the joint separation reached 7 mm. *Fig. 4* shows the meshed model with boundary conditions and the used spring models positions.

Additionally, the reinforced concrete beam components and the grout block were discretized using quadrilateral-based solid elements within the adopted three-dimensional mesh generation scheme in ANSYS. A comprehensive mesh sensitivity study was conducted to determine the optimum mesh size for the numerical model. For this purpose, the 16 mm specimen was selected as a reference case, and several element sizes were examined by comparing the corresponding predicted ultimate load capacities. The results showed that a mesh size of 50 mm provided sufficiently accurate predictions of the ultimate load with a variation of less than 5%, while still maintaining reasonable computational efficiency. Accordingly, this mesh size was adopted for the subsequent analyses. In this way, an appropriate balance was achieved between numerical accuracy and computational cost.

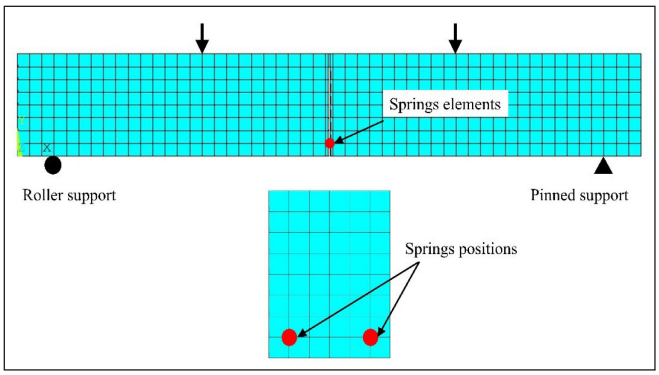


**Fig.4:** *Finite element model showing boundary conditions and spring elements locations*

## 4.2 VALIDATION OF THE SIMPLIFIED SPRING MODELS

The validation process was carried out by comparing the numerical predictions with the experimental results previously obtained by the authors for all tested specimens. *Fig.5* presents the comparison between the experimental and numerical responses in terms of the global behaviour, represented by the load–deflection curves, and the local behaviour, represented

**Fig.5:** *Numerical vs experimental results comparison for all the tested specimens (a) load-deflection response, (b) load-separation response*

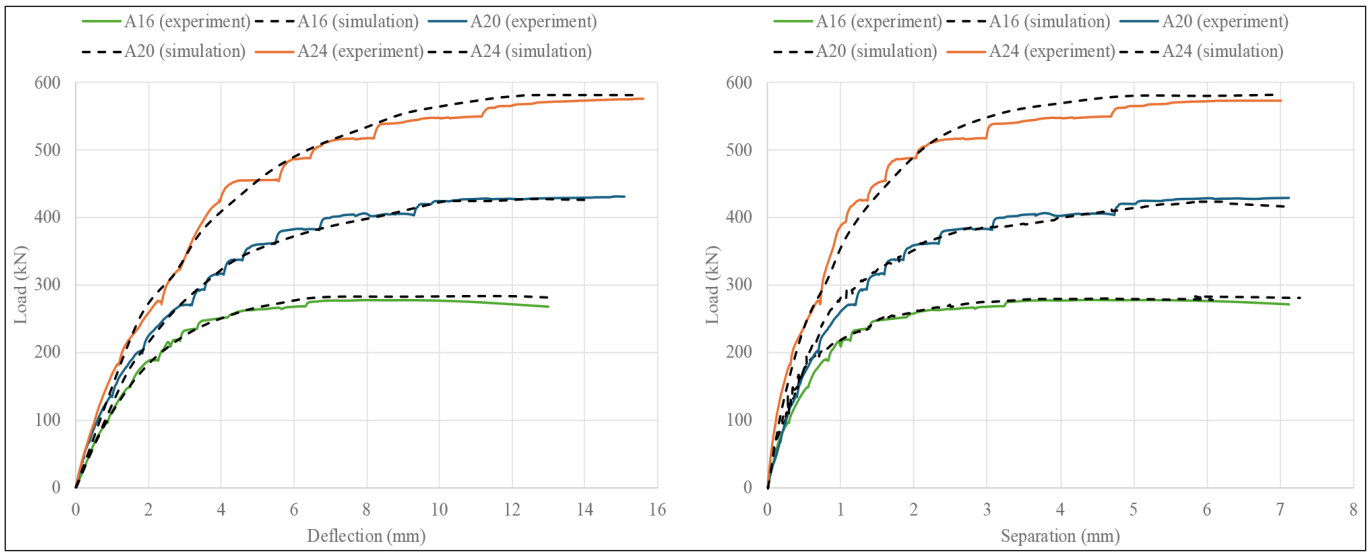

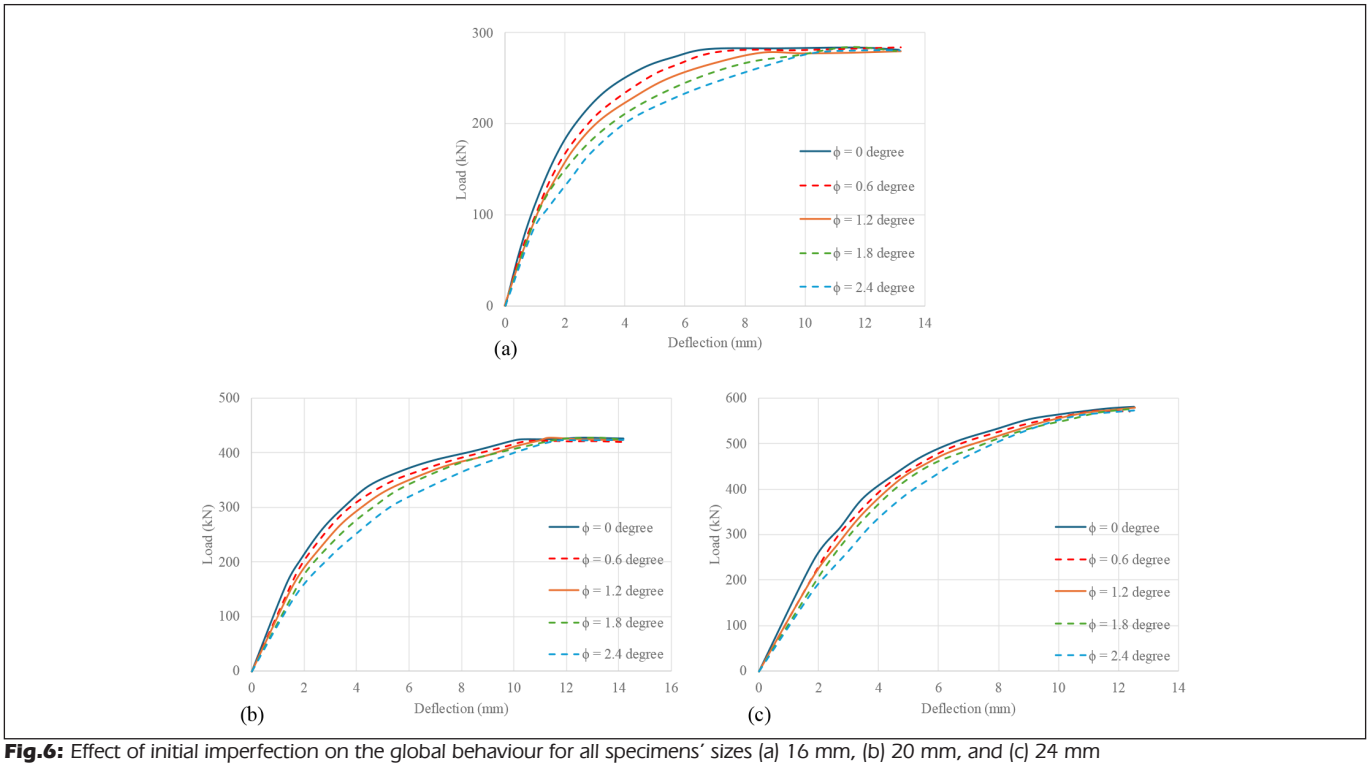


**Fig.6:** Effect of initial imperfection on the global behaviour for all specimens' sizes (a) 16 mm, (b) 20 mm, and (c) 24 mm

by the load–separation curves, for the modeled configurations. In general, the numerical model showed good agreement with the experimental results and was able to reproduce the main behaviour of the tested specimens with reasonable accuracy, where the difference in ultimate load between the experimental test and the FE analysis was less than 5%. The model captured the initial stiffness, the nonlinear response, and the final load level reasonably. Generally, the comparison confirms that the developed numerical model is suitable for representing both the global and local behaviour of the assembled beam.

## 4.3 EFFECT OF INITIAL IMPERFECTION ON THE GLOBAL BEHAVIOUR OF ASSEMBLED BEAMS

Using simple interpolation and extrapolation, additional spring models representing further levels of initial geometrical imperfection were generated. These models were then implemented in the simplified ANSYS model to investigate the ability of the proposed spring representation to capture the influence of initial imperfection on the global behaviour of the considered beams. In total, five imperfection levels were considered for each specimen size, namely , , , , and , and the obtained results were compared, as shown in *Fig. 6* and *table 1*.

Fig.6 illustrates the influence of the initial geometrical imperfection on the global load–deflection response of the assembled beams for the 16, 20, and 24 mm connection types. In all cases, increasing the imperfection level resulted in a clear reduction in the initial global stiffness, which is represented by the stiffness of the line plotted from the origin to 70% of the ultimate load capacity. To quantify this effect, the secant stiffness was calculated from the origin to 70% of the ultimate load. The results showed a progressive decrease in stiffness with increasing imperfection angle for all specimen types. For the 16 mm specimen, the secant stiffness decreased from 85.79 kN/mm at to 51.30 kN/mm at , corresponding to a reduction of 40.2%. For the 20 mm specimen, the stiffness decreased from 85.68 to 57.41 kN/mm, giving a reduction of 33.0%, while for the 24 mm specimen, it decreased from 102.46 to 77.16 kN/mm, corresponding to a reduction of 24.7%. These results indicate that the initial geometrical imperfection mainly affects the stiffness-related response of the assembled beams, while the ultimate load capacity remains almost unchanged. This means that imperfection has a more pronounced influence on the serviceability behaviour than on the load-carrying capacity. It is also evident that the smaller-diameter connections are more sensitive to the imposed imperfection, as the 16 mm specimens exhibited the largest stiffness reduction, whereas the 24 mm specimens showed the smallest reduction and maintained the highest stiffness values throughout the investigated range. Therefore, the results confirm that larger bolt diameters provide better tolerance against assembly imperfections and are less affected by the reduction in contact efficiency caused by the inclined setup configuration, this difference mainly caused by higher axial stiffness and higher clamping force generated from the same applied torque for the bigger anchor bolts.

# 5. CONCLUSIONS

This study was conducted to develop a simplified representation of the three-dimensional bolted connection by using spring elements that capture the actual behaviour of hybrid bolted connections employed in precast reinforced concrete assemblies. The proposed multilinear spring models were derived by fitting the experimental results to represent the tension force–separation response at the connection location. Spring models were developed for three connection sizes under both perfect and imperfect setup configurations of the assembled precast members, and an equation was also introduced to enable simple calculation of the stiffness of each spring segment. Based on these findings, the following conclusions can be drawn:

**Table 1:** *Initial stiffness degradation caused by initial imperfections*

| Specimen type | Imperfection (degree) | $K_{sec,0.7}$ (kN/mm) | Stiffness reduction against (0 degrees) |
|---|---|---|---|
| 16 mm | 0.0 | 86 | 0% |
| | 0.6 | 73 | 15% |
| | 1.2 | 67 | 22% |
| | 1.8 | 57 | 34% |
| | 2.4 | 51 | 40% |
| 20 mm | 0.0 | 86 | 0% |
| | 0.6 | 81 | 5% |
| | 1.2 | 72 | 16% |
| | 1.8 | 65 | 24% |
| | 2.4 | 57 | 33% |
| 24 mm | 0.0 | 102 | 0% |
| | 0.6 | 97 | 5% |
| | 1.2 | 92 | 11% |
| | 1.8 | 88 | 15% |
| | 2.4 | 77 | 25% |

1- The numerical results closely agree with the experimental measurements, confirming that the proposed models can capture both local and global behaviour of the assembled structures. Additionally, equations were proposed to calculate the stiffness of the required segment as a function of the bolt diameter and imperfection level. However, these stiffness predictions remain limited to the investigated ranges of bolt diameter and imperfection level.

2- A parametric study was conducted to investigate the effect of initial imperfection on the global behaviour of RC assemblies. As the imperfection degree increases, the initial stiffness of the load-deflection response decreases. At the same time, the ultimate load capacity stays almost unchanged. The study reveals that the smaller anchor bolts had a higher reduction in the initial stiffness than the bigger ones, which can be attributed to the fact that the bigger bolts have higher axial stiffness, and more clamping force can be exerted using the same tightening torque percentage of the maximum allowable torque for the smaller bolts.

Overall, the developed simplified multilinear spring models offer an important tool for structural designers and researchers who require a simpler, more practical way to simulate the realistic behaviour of hybrid bolted connections.

# 6. REFERENCES


Bao, Y., & Tan, K. H. (2023). Experimental and numerical study on performance of precast concrete wet and dry joints under progressive collapse scenario. *Journal of Building Engineering*, *74*, 106739. https://doi.org/10.1016/j.jobe.2023.106739.

Elliott, K. S. (2019). *Precast concrete structures*. Crc Press. https://doi.org/10.1201/9780367814885.

Hameedi, W. S., & Völgyi, I. (2025). Experimental Investigation of Lateral Stability of a Longitudinally Assembled Girder Made of Precast Reinforced and Prestressed Concrete Parts. *Periodica Polytechnica Civil Engineering*. https://doi.org/10.3311/PPci.38183.

Hameedi, W., & Völgyi, I. (2026). Experimental investigation on the initial stiffness of bolted connections in precast RC members. *Discover Applied Sciences*, *8*(4), 414. https://doi.org/10.1007/s42452-026-08457-9.

Holly, I., & Abrahoim, I. (2020). Connections and Joints in Precast Concrete Structures. *Slovak Journal of Civil Engineering*, *28*(1), 49–56. https://doi.org/10.2478/sjce-2020-0007.

Pham, K. V. A., Kim, Y.-N., Woo, S., Kim, S. J., Lee, G., & Lee, K. (2024). Experimental-FEA investigation of the structural performance of steel box connector in precast concrete connection. *Journal of Building Engineering*, *95*, 110077. https://doi.org/10.1016/j.jobe.2024.110077.

Psycharis, I. N., & Mouzakis, H. P. (2012). Shear resistance of pinned connections of precast members to monotonic and cyclic loading. *Engineering Structures*, *41*, 413–427. https://doi.org/10.1016/j.engstruct.2012.03.051.

Qing, Y., Wang, C.-L., Meng, S., & Zeng, B. (2022). Experimental study on the seismic performance of precast concrete columns with thread-bolt combination couplers. *Engineering Structures*, *251*, 113461. https://doi.org/10.1016/j.engstruct.2021.113461.

Taher, S. E. F., ATTA, A., & SHARKAWI, A. E.-D. (2015). Wet vs. Dry Techniques in Connecting Piecewise Precast Reinforced Concrete Beam-Column Elements In Moment Resisting Frames. *No. March*.

Wang, G., Li, Y., Li, Z., & Ingham, J. M. (2020). Experimental and numerical study of precast concrete columns with hybrid bolted splice connections. *Structures*, *28*, 17–36. https://doi.org/10.1016/j.istruc.2020.08.042.

Yrjölä, J., & Kinnunen, J. (2023). *Bolted Column Shoe Connections – Sustainable and Smart Solution for Precast Structures* (pp. 1724–1733). https://doi.org/10.1007/978-3-031-32511-3_177.

Yuksel, E., Karadogan, H. F., Bal, İ. E., Ilki, A., Bal, A., & Inci, P. (2015). Seismic behavior of two exterior beam–column connections made of normal-strength concrete developed for precast construction. *Engineering Structures*, *99*, 157–172. https://doi.org/10.1016/j.engstruct.2015.04.044.

Zhong, Y., Xiong, F., Chen, J., Deng, A., Chen, W., & Zhu, X. (2019). Experimental Study on a Novel Dry Connection for a Precast Concrete Beam-To-Column Joint. *Sustainability*, *11*(17), 4543. https://doi.org/10.3390/su11174543.



**Wael Hameedi** (1988) He is a PhD candidate at the Department of Structural Engineering, Budapest University of Technology and Economics, Hungary. He received his MSc in Structural Engineering from the National University of Malaysia. His research interests include reinforced concrete structures and precast reinforced concrete connections. He is a member of the Iraqi Engineers Association. E-mail: wael.hameedi@edu.bme.hu

**István Völgyi** He made his MSc and Ph.D. at the Budapest University of Technology and Economics, Hungary, where he serves as an associate professor. He is a member of the fib and standardization committees of MSZT and MAÚT. E-mail: volgyi.istvan@emk.bme.hu

# FROM CLAY MINERALOGY TO FUNCTIONAL ADDITIVES: A SYSTEMATIC REVIEW OF MATERIAL FACTORS GOVERNING THE MECHANICAL PROPERTIES OF LC3 BASED CEMENTITIOUS SYSTEMS


Sara Baradarandilmaghani – Sándor Sólyom

https://doi.org/10.32970/CS.2026.1.6

*Limestone calcined clay cement (LC³ or LC3) is a promising low-carbon binder because it can substantially reduce clinker content through the combined use of calcined clay and limestone. Despite growing research interest, the mechanical performance of LC3-based systems is influenced by many interacting variables, including clay mineralogy, calcination conditions, limestone characteristics, sulphate balance, supplementary cementitious materials, admixtures, nano-additives, fibres, recycled aggregates, and curing regimes. This systematic literature review synthesizes how this material factors affect the mechanical properties of LC3-based paste, mortar, concrete, and cementitious composites. The review followed PRISMA 2020 and was based on record-level exports from Scopus and Web of Science. A total of 1275 records were identified; after removing 407 duplicates, 448 LC3-focused records were retained for evidence mapping, including 429 primary research records and 19 contextual review records. The synthesis indicates that compressive strength is the most frequently reported mechanical property, whereas tensile strength, flexural strength, elastic modulus, shrinkage, creep, fracture energy, bond strength, and toughness remain less systematically investigated. High-kaolinite calcined clays generally promote strength development through pozzolanic reaction, alumina release, carboaluminate formation, and pore refinement. However, mechanical performance is not governed by kaolinite content alone, but also by calcination quality, fineness, sulphate optimization, water-to-binder ratio, workability, and curing. Overall, LC3 mechanical optimization requires integrated material characterization and mixture design rather than simple clinker-replacement rules.*

**Keywords:** *Limestone calcined clay cement, LC³, LC3, calcined clay, mechanical properties, supplementary cementitious materials, nano additives, fibres, recycled aggregate, systematic literature review.*

## 1 INTRODUCTION

Concrete is essential for infrastructure development, but the environmental burden of ordinary Portland cement is a central challenge for sustainable construction. The clinker phase of cement is responsible for a large fraction of the carbon footprint because clinker production requires calcination and high-temperature processing (Scrivener et al., 2018b; Meenakshi Sharma et al., 2021). Reducing the clinker factor through supplementary cementitious materials is therefore one of the most realistic strategies for lowering embodied carbon in concrete without abandoning the existing cement and concrete infrastructure. Limestone calcined clay cement, commonly called LC3 or LC3, has become a major low-carbon binder technology because it combines Portland clinker, calcined clay, limestone, and gypsum. A frequently investigated formulation is LC3-50, in which clinker content is reduced to approximately 50% and the remaining binder fraction is mainly calcined clay, limestone, and gypsum (Scrivener et al., 2018b; M. Sharma et al., 2021). The performance of LC3 is not explained by dilution alone. Calcined clay supplies reactive alumina and silica, limestone participates in carbonate-aluminate reactions, and the fine particles modify packing and nucleation. The combined reaction produces carboaluminate phases and contributes to porosity refinement and strength development (Antoni et al., 2012; Zunino and Scrivener, 2021a).

Existing LC3 research has demonstrated that properly designed LC3 binders can achieve mechanical performance comparable to OPC and other blended cement systems (Avet and Scrivener, 2018; Dhandapani et al., 2018; Scrivener et al., 2018b; Meenakshi Sharma et al., 2021). However, LC3 is not a single fixed material. Its performance depends strongly on the mineralogy and reactivity of the clay, the amount and fineness of limestone, the sulphate balance, the water-to-binder ratio, particle-size distribution, curing, admixture compatibility, and the presence of additional functional materials. This makes LC3 a material system rather than a simple cement replacement. Previous reviews have addressed LC3 hydration, durability, sustainability, and general concrete performance (Scrivener et al., 2018b; Meenakshi Sharma et al., 2021). Nevertheless, the evidence remains fragmented with respect

to the mechanical role of material modifications. Many papers report compressive strength, while fewer report tensile strength, flexural strength, elastic modulus, shrinkage, creep, toughness, fracture energy, bond strength, or structural-scale mechanical behaviour. A systematic synthesis focused specifically on material factors is therefore needed. The present review addresses this gap by asking: How do clay mineralogy, calcination, limestone, sulphate balance, supplementary cementitious materials, nano additives, admixtures, fibres, recycled materials, and curing conditions govern the mechanical properties of LC3 based cementitious systems? The review is intended to support mix-design decisions, identify robust performance mechanisms, and define future research priorities for LC3 concrete.

# 2 REVIEW OBJECTIVES AND RESEARCH QUESTIONS (RQ)

The objective of this review is to systematically synthesize material factors governing the mechanical properties of LC3 based paste, mortar, concrete, and cementitious composites. The review focuses on material-performance relationships rather than only on overall sustainability or durability.

- RQ1: How does clay mineralogy, kaolinite content, calcination temperature, calcination duration, and clay fineness influence LC3 strength development?
- RQ2: How do limestone content, limestone fineness, gypsum dosage, and sulphate balance affect hydration, porosity refinement, and mechanical properties?
- RQ3: What are the effects of additional SCMs and waste-derived powders on compressive, tensile, flexural, and stiffness-related properties?
- RQ4: How do nano additives and chemical admixtures affect early strength, workability, compaction, hydration, and mechanical performance?
- RQ5: How do fibres, engineered cementitious composite concepts, recycled aggregates, and alternative aggregates influence flexural behaviour, toughness, cracking, and strength?
- RQ6: What reporting and experimental gaps limit the development of reliable LC3 mechanical mix-design guidelines?

# 3 METHODOLOGY

## 3.1 Review design and reporting framework

The review was structured according to PRISMA 2020, which requires systematic reviews to identify the report as a systematic review, define eligibility criteria, information sources, search strategies, selection processes, data items, risk-of-bias methods, synthesis methods, and study-selection flow (Page et al., 2021). The uploaded PRISMA checklist and expanded checklist were used as reporting guides. This manuscript therefore reports database sources, search strategy, deduplication, screening, inclusion logic, data extraction, and synthesis categories.

## 3.2 Information sources and search data

Record level research was performed using Scopus and Web of Science exports *Table 1* supplied by the author. The search focused on LC3 based paste, mortar, concrete, and cementitious composites in relation to mechanical properties and material factors. Additional literature known to be central to LC3 development, including foundational LC3 chemistry and PRISMA guidance, was retained for contextual interpretation and reference framing.

## 3.3 Search strategy

The Scopus search string used TITLE-ABS-KEY fields, and the Web of Science search used Topic fields. The conceptual structure combined LC3 terms, material scale terms, and mechanical/material-factor terms *Table 1*.

## 3.4 Eligibility criteria

The inclusion and exclusion criteria are reported in *Table 2*. These criteria were designed to align the screening process with the central objective of the review: identifying how material factors influence the mechanical performance of LC3 based cementitious systems. Accordingly, records were included when they explicitly addressed LC3, limestone calcined clay cement, calcined clay limestone binders, or equivalent formulations, and when they examined LC3 based paste, mortar, concrete, engineered cementitious composites, recycled aggregate systems, 3D-printable materials, or related construction applications. To be retained, each study also had to report at least one relevant material variable and at least one mechanical or mechanical adjacent response.

## 3.5 Record management, deduplication/remove, and selection process

The two database exports contained 539 Scopus records and 736 Web of Science records, giving 1275 total records. Deduplication (removing repeated paper) was performed using DOI as the primary key and normalized title as the secondary key. This removed 407 duplicate records and left 868 records for title/abstract screening. A strict LC3 title rule was used to reduce false positives from broad calcined clay, metakaolin, geopolymer, or limestone powder records. This maintained 448 LC3-focused records, including 429 primary records and 19 context/review records.

## 3.6 Data extraction

*Table 3* summarises the data items extracted from each included record. The extracted information covered bibliographic details, material scale, binder/material factors, mechanical outcomes, mechanistic evidence, and screening decisions. This structure ensured that the included studies were not only counted bibliographically but also analysed according to the specific LC3-related variables relevant to the review. In particular, clay mineralogy, kaolinite content, calcination, limestone content, sulphate balance, SCMs, nano-additives, fibres, recycled materials, and curing conditions were extracted because these factors directly influence the mechanical performance of LC3-based cementitious systems. Mechanistic information such as hydration, carboaluminate formation,

pore refinement, particle packing, ITZ effects, crack bridging, and workability was also recorded to support interpretation of the performance trends.

### 3.7 Synthesis method and certainty assessment

Because mixture designs, binder compositions, curing regimes, material sources, and outcome definitions differed widely across the records, a quantitative meta-analysis was not performed. Instead, a structured narrative synthesis and evidence-map approach was used. Records were grouped into material-factor categories: clay mineralogy/calcination, limestone/sulphate balance, additional SCMs, nano additives, chemical admixtures/rheology, fibres/ECC, recycled/alternative aggregates, curing/temperature, 3D printing, and prediction/optimization. Evidence strength was judged qualitatively as strong, moderate, limited, or emerging based on the number of records, consistency of direction, availability of mechanistic explanation, and relevance to concrete-scale mechanical performance.

## 4 RESULTS

### 4.1 Study selection

As illustrated in the PRISMA 2020-style flow diagram in *Fig 1* process reduced the initial literature pool to the final body of studies included in this review. The database search yielded 1,275 records, of which 539 were retrieved from Scopus and 736 from Web of Science. Following duplicate removal, 868 unique records remained for title and abstract screening. The removal of 407 duplicate records reflects the expected overlap between the two databases and indicates that the search strategy captured a substantial shared body of LC3-related publications.

At the title and abstract screening stage, 420 records were excluded because they fell outside the scope of the review. These records generally addressed non-LC3 binders, unrelated cementitious or non-cementitious systems, topics without direct relevance to mechanical performance, or studies that did not examine the material factors targeted in this review.

The remaining 448 records were assessed for eligibility and included in the final review. As reported in *Table 4* the final dataset consisted of 429 primary records used in the material-factor synthesis and 19 contextual or review records used to support background discussion and interpretation. This classification separates primary experimental evidence from secondary contextual literature and improves the transparency of the review methodology.

### 4.2 Bibliometric overview

The included LC3 evidence base has expanded rapidly in recent years. The publication trend indicates that LC3 mechanical-performance research has moved from foundational paste and mortar studies toward concrete, ECC, 3D-printing, recycled aggregate, and functional additive systems.

The descriptive distribution of the included LC3 literature is presented in *Fig 2-8*. As shown in *Fig 2* the number of included LC3 material-factor records increased gradually after 2017 and rose sharply after 2022. This trend indicates that LC3 has moved from an emerging low-clinker cement concept toward a rapidly expanding research field. The strongest growth appears in the most recent years, particularly around 2024–2025, which confirms the increasing scientific interest in LC3 as a practical route for lowering clinker content while maintaining mechanical and durability performance. The slight reduction in 2026 should be interpreted cautiously, because the year is not yet complete and the available records only represent publications indexed at the time of database extraction.

The distribution of publication sources is shown in *Fig 3*. The highest number of included records was published in Construction and Building Materials, followed by sources such as RILEM Book series, Journal of Building Engineering, Cement and Concrete Composites, and Cement and Concrete Research. This pattern confirms that LC3 research is mainly concentrated on construction materials, cement chemistry, and concrete Technology journals. The dominance of these sources is consistent with the scope of this review, which focuses on material factors governing the mechanical properties of LC3-based cementitious systems.

The thematic classification of the included records is presented in *Fig 4*. The largest groups are related to clay mineralogy/calcination and limestone/carbonate/gypsum/sulphatebalance, followed by curing conditions, supplementary cementitious materials, chemical admixtures/rheology, fibres, recycled aggregates, nano additives, 3D printing, and prediction or machine learning related studies. This distribution shows that the LC3 literature is still strongly dominated by fundamental binder design variables, especially clay reactivity, limestone content, and sulphate optimization. In contrast, fewer studies address advanced functional applications such as nano modified LC3, fibre reinforced LC3, recycled aggregate LC3, and printable LC3. This imbalance highlights an important research gap: while the basic hydration and material design mechanisms of LC3 are increasingly understood, its development into multifunctional and application-specific cementitious systems remains less mature.

As illustrated in *Fig 5* the subject-area distribution is dominated by Engineering and Materials Science, which together account for many included records. Smaller contributions are

**Table 1:** Database search strings used for systematic review

| Database | Search string |
|---|---|
| **Scopus** | (“limestone calcined clay cement” OR “LC3” OR “LC³” OR “calcined clay limestone cement”) AND (concrete OR mortar OR paste) AND (“mechanical properties” OR “compressive strength” OR “tensile strength” OR “flexural strength” OR “elastic modulus” OR shrinkage OR creep OR toughness OR fibre OR fibre OR “nano silica” OR “superplasticizer” OR “recycled aggregate” OR “supplementary cementitious materials”) |
| **Web of Science** | (“limestone calcined clay cement” OR “LC3” OR “LC³” OR “calcined clay limestone cement”) AND (concrete OR mortar OR paste) AND (“mechanical properties” OR “compressive strength” OR “tensile strength” OR “flexural strength” OR “elastic modulus” OR shrinkage OR creep OR toughness OR fibre OR fibre OR “nano silica” OR “superplasticizer” OR “recycled aggregate” OR “supplementary cementitious materials”) |

**Table 2:** Inclusion and exclusion criteria

| Type | Criterion |
|---|---|
| Inclusion | LC3, limestone calcined clay cement, calcined clay-limestone cementitious systems, or equivalent formulations in title/abstract/key-words |
| Inclusion | Paste, mortar, concrete, engineered cementitious composites, recycled aggregate concrete, 3D-printable cementitious materials, or structural/construction applications based on LC3 |
| Inclusion | One relevant material factor at least: clay type, calcination, limestone, sulphate/gypsum, SCM, additive, admixture, fibre, aggregate, recycled material, or curing |
| Inclusion | At least one mechanical or mechanical-adjacent outcome: compressive strength, tensile strength, flexural strength, elastic modulus, shrinkage, creep, toughness, fracture, bond, stiffness, or strength development |
| Exclusion | Records without a clear LC3 or limestone-calcined-clay focus |
| Exclusion | Records dealing only with OPC, geopolymer, alkali-activated materials, or general calcined clay systems without LC3 relevance |
| Exclusion | Records with no mechanical/material factor focus after title/abstract screening |

**Table 3:** Data items extracted from the database exports

| Data group | Extracted variables |
|---|---|
| **Bibliographic** | Authors, year, title, source, DOI, database source, citation count |
| **Material scale** | Paste, mortar, concrete, ECC, fibre-reinforced composite, recycled aggregate concrete, 3D-printable composite |
| **Binder/material factors** | Clay mineralogy, kaolinite content, calcination, fineness, limestone, gypsum, sulphate balance, SCMs, nano additives, fibres, recycled materials, curing |
| **Mechanical outcomes** | Compressive strength, tensile strength, flexural strength, elastic modulus, shrinkage, creep, toughness, fracture, bond, impact, ductility |
| **Mechanistic evidence** | Hydration, carboaluminate formation, pore refinement, particle packing, ITZ, crack bridging, workability/compaction |
| **Screening decision** | Include/exclude, synthesis role, material category tags, exclusion reason |

observed from Environmental Science, Energy, Chemistry, Earth and Planetary Sciences, and other fields. This confirms that LC3 research is primarily positioned within engineering and materials science, but it also has clear links to sustainability, environmental impact reduction, cement chemistry, and resource efficiency. The presence of environmental and energy related subject areas is important because LC3 is not only a mechanical properties topic, but also a low-carbon cement technology intended to reduce clinker-related $CO_2$ emissions.

The country distribution in *Fig 6* shows that LC3 research is geographically broad, but unevenly distributed. China appears as the leading contributor, followed by countries such as India, the United Kingdom, Switzerland, Iran, Turkey, Cuba, Colombia, Malaysia, Austria, and Portugal. This distribution reflects both the global interest in LC3 and the importance of regional raw material availability, especially calcined clay and limestone. The relatively high contribution from countries with strong cement, concrete, and sustainability research programs suggests that LC3 is increasingly being investigated as a regionally adaptable binder technology rather than a single fixed cement formulation.

The document type distribution is presented in *Fig 7*. Most included records are journal articles, while smaller portions are book chapters, conference papers, and review papers. This indicates that the evidence base of the present review is mainly built on peer-reviewed original research articles rather than secondary sources. This is important for the reliability of the synthesis, because the review aims to evaluate material factors and their influence on mechanical properties using primary experimental and material performance evidence.

Finally, *Fig* 8 indicates the affiliation distribution of the included records. The results indicate that LC3 research is supported by a wide range of universities, research institutes, and technical organizations. The presence of several leading

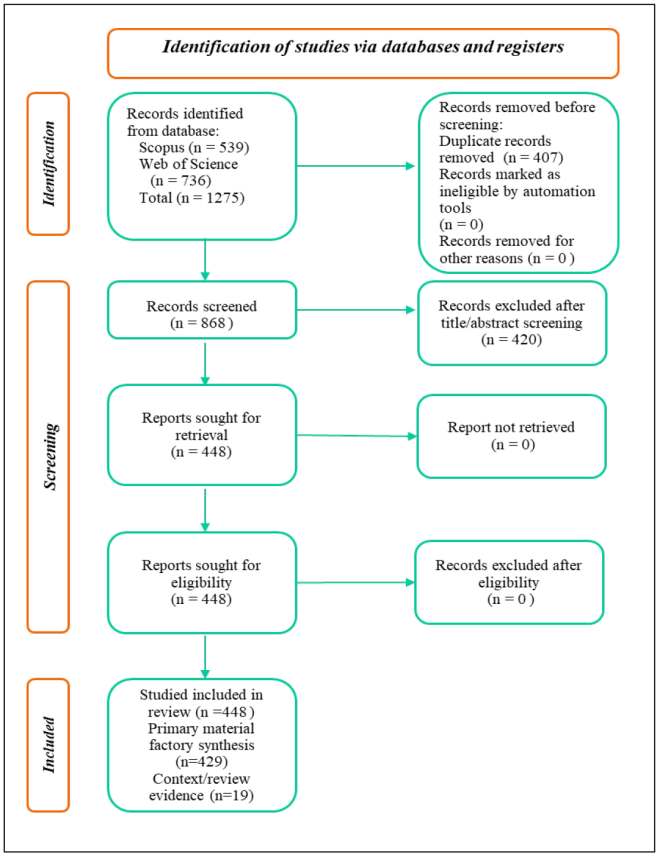


**Fig 1:** PRISMA 2020 style study-selection flow diagram based on Scopus and Web of Science exports

institutions with repeated contributions suggests that LC3 research has developed around specialized cement materials research groups, while the long tail of smaller contributors indicates a widening international research base. This institutional diversity supports the relevance of LC3 as a global

**Table 4** Final PRISMA counts

| PRISMA item | Number |
|---|---|
| Records identified from Scopus | 539 |
| Records identified from Web of Science | 736 |
| Total records identified | 1275 |
| Duplicate records removed | 407 |
| Records screened | 868 |
| Records excluded after title/abstract screening | 420 |
| Reports assessed for eligibility | 448 |
| Studies included in review | 448 |
| Primary records in material-factor synthesis | 429 |
| Context/review records retained | 19 |

research topic, but it also suggests that differences in local clay sources, testing methods, curing regimes, and mixture designs may create variability across published studies.

Together, *Fig 2-8* shows that LC3 research has expanded rapidly in recent years, is mainly concentrated in engineering and materials science journals, and is dominated by studies on clay mineralogy, calcination, limestone interaction, sulphate balance, and mechanical performance. However, the bibliometric patterns also reveal clear underexplored areas, particularly LC3 systems incorporating nano additives, fibres, recycled aggregates, 3D printing, rheology-oriented design, and predictive modelling. These gaps support the need for a systematic review that connects material factors with mechanical properties and identifies future directions for multifunctional LC3 based cementitious systems.

**Fig 2:.** Publication trend of included LC3 material-factor records

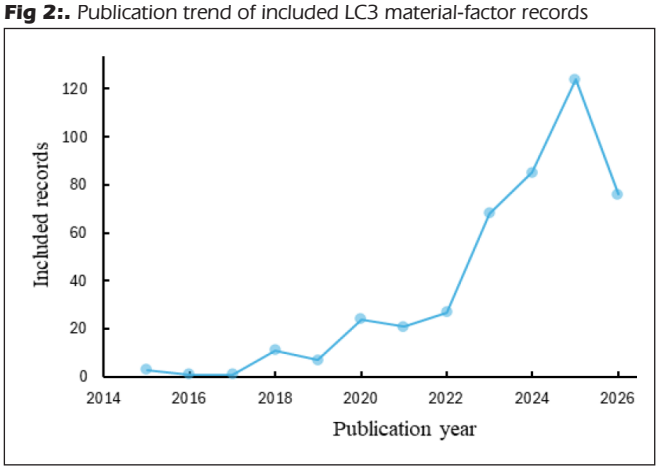


**Fig 3:** Top publication sources

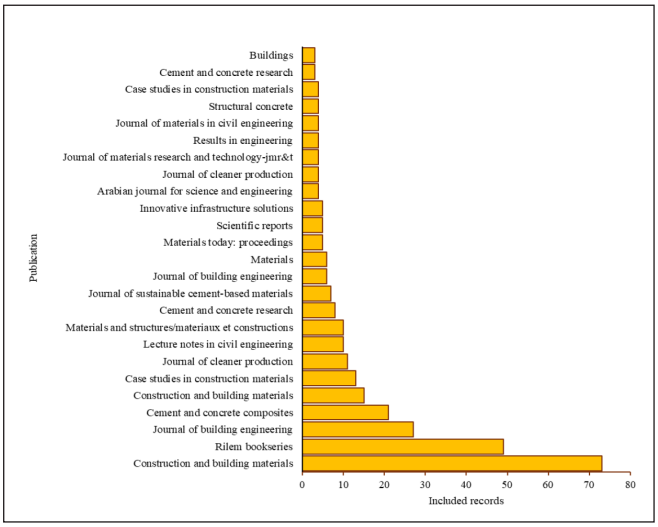


## 4.3 Key included studies

The representative records used to organize the thematic synthesis are summarized in *Table 5*. These studies were selected because they are either highly cited, methodologically influential, or directly relevant to the main material factor categories considered in this review. The *Table 5* indicates that the LC3 literature is strongly centred on clay mineralogy, calcination, limestone/carbonate reactions, gypsum/sulphate balance, pore structure development, and mechanical performance. At the same time, several studies extend the field toward engineered cementitious composites, chemical admixtures, curing temperature effects, and supplementary waste based additions. Therefore, *Table 5* provides a transparent link between the bibliometric screening stage and the subsequent technical synthesis, showing how the main discussion categories were derived from the most relevant records in the final dataset.

# 5 MATERIAL-FACTOR SYNTHESIS

## 5.1 Clay mineralogy, kaolinite content, and calcination

Clay mineralogy is the central material factor in LC3. Calcination transforms kaolinite into metakaolin, which provides reactive alumina and silica. These reactive species participate in pozzolanic reaction and promote carboaluminate formation when limestone is present. Therefore, kaolinite content is a strong predictor of LC3 reactivity, but not the only predictor of mechanical properties (Antoni et al., 2012; Avet and Scrivener, 2018). The systematic evidence map shows that clay mineralogy/calcination appeared in most included records. This high frequency is expected because calcined clay is the defining reactive SCM in LC3. However, the literature shows that simply reporting calcined clay is insufficient. Mechanical properties depend on kaolinite content, degree of dihydroxylation, calcination temperature, calcination duration, amorphous content, fineness, impurities, and water demand (Scrivener et al., 2018b). High-kaolinite clays generally support higher strength development because they release more reactive alumina and silica. Nevertheless, very reactive, or very fine clays can increase water demand and reduce workability, which may reduce realized concrete strength if admixture dosage and compaction are not optimized. Low grade clays remain important for industrial LC3 because they are more widely available, but their performance is more variable and requires stronger characterization (Alujas et al., 2015).

**Fig 4:** Material-factor categories detected in included records

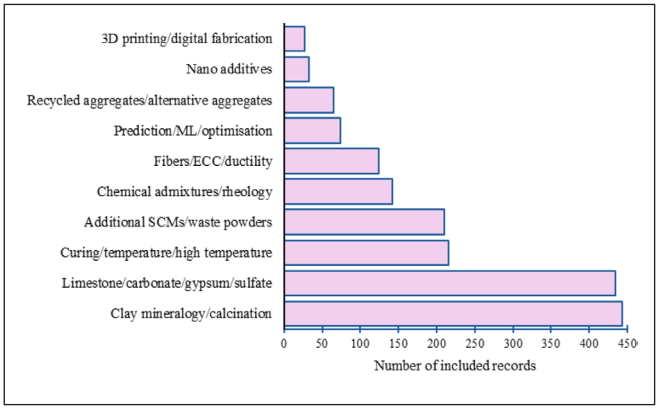

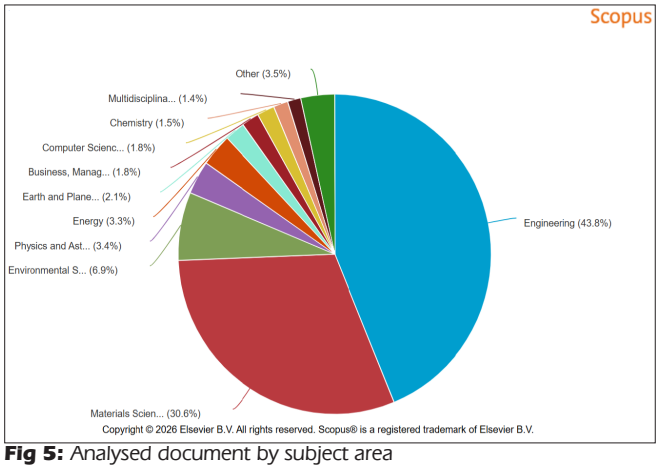


**Fig 5:** Analysed document by subject area

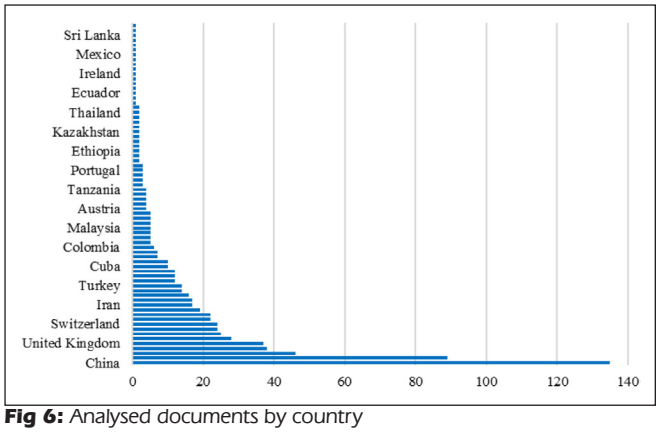


**Fig 6:** Analysed documents by country

## 5.2 Limestone content, limestone fineness, and carbonate-alumina synergy

Limestone is both a physical filler and a chemical participant in LC3 (X. Li et al., 2023). Physically, fine limestone can improve particle packing and provide nucleation surfaces. Chemically, carbonate participates in the stabilization of carboaluminate phases when reactive alumina is available from calcined clay (Antoni et al., 2012; Scrivener et al., 2018b; Zunino and Scrivener, 2021a). This synergy explains why the combined use of metakaolin/calcined clay and limestone can provide stronger performance than simple inert dilution.

Therefore, limestone dosage should be optimized together with clay reactivity and sulphate balance rather than treated as a fixed constant. The evidence base supports the use of limestone as a functional component, but it also shows that limestone purity, fineness, and substitution level should be reported more consistently.

## 5.3 Sulphate balance and gypsum dosage

Sulphate balance is a decisive but sometimes underreported variable in LC3 mechanical properties. Increasing sulphate, decrease portlandite content, because increasing sulphate, increases ettringite precipitation (Andrade Neto et al., 2022; He et al., 1995; Silva et al., 2024). Gypsum regulates early aluminate reactions, ettringite formation, setting, and the transition toward carboaluminate assemblages. Because LC3 contains additional alumina from calcined clay and high filler content, its sulphate demand may differ from OPC. Inadequate sulphate can cause non-optimal early hydration and strength, whereas

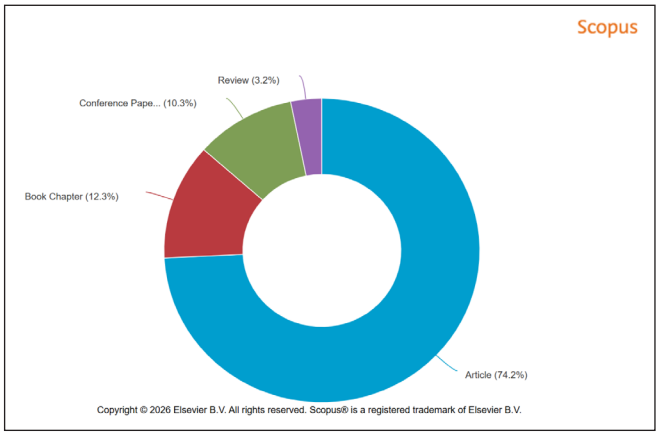


**Fig 7:** Analysed documents by type

excessive sulphate may alter the balance of ettringite and carboaluminate phases (Antoni et al., 2012; Silva et al., 2024).

A key implication for the review is that strength differences between LC3 mixtures should not be attributed only to clay source or limestone content if sulphate optimization was not controlled. Future papers should report gypsum content, sulphate source, sulphate optimization method, calorimetry response, and early-age strength together.

## 5.4 Additional SCMs and waste-derived powders

Additional SCMs and waste-derived powders are increasingly studied in LC3 systems. These include fly ash, slag/GGBFS, silica fume, rice husk ash, bagasse ash, natural pozzolans, volcanic ash, glass powder, ceramic waste, biochar, phosphor-gypsum derived materials, marble powder, and other industrial by-products. Their effects on mechanical properties are not uniform because they may act through reactivity, filler effects, particle packing, later-age pozzolanic reaction, or dilution.

Slag rich additions may improve later-age strength because of latent hydraulic reactivity and additional C-A-S-H formation. Fly ash may improve workability and later-age properties, but early strength can suffer if replacement levels are high or curing is insufficient. Silica fume and nano silica can refine pores and improve early performance, but water demand and dispersion become critical. Waste powders can support circular economy goals, but they require characterization of chemical composition, particle size, and reactivity.

## 5.5 Nano additives

Nano additives represent an emerging LC3 modification route. Nano silica is the most frequently reported nano additive because it can provide nucleation sites, accelerate hydration, and refine pore structure. The included evidence indicates that nano silica can improve early compressive strength and microstructural densification when properly dispersed (Lin et al., 2022). However, nano additives may also increase water demand and cost.

The practical significance of nano additives depends on dosage, dispersion, admixture compatibility, and whether performance improvements are large enough to justify additional production complexity. For future research, nano additives should be evaluated not only at paste scale but also in mortar and concrete with realistic mixing procedures and workability targets.

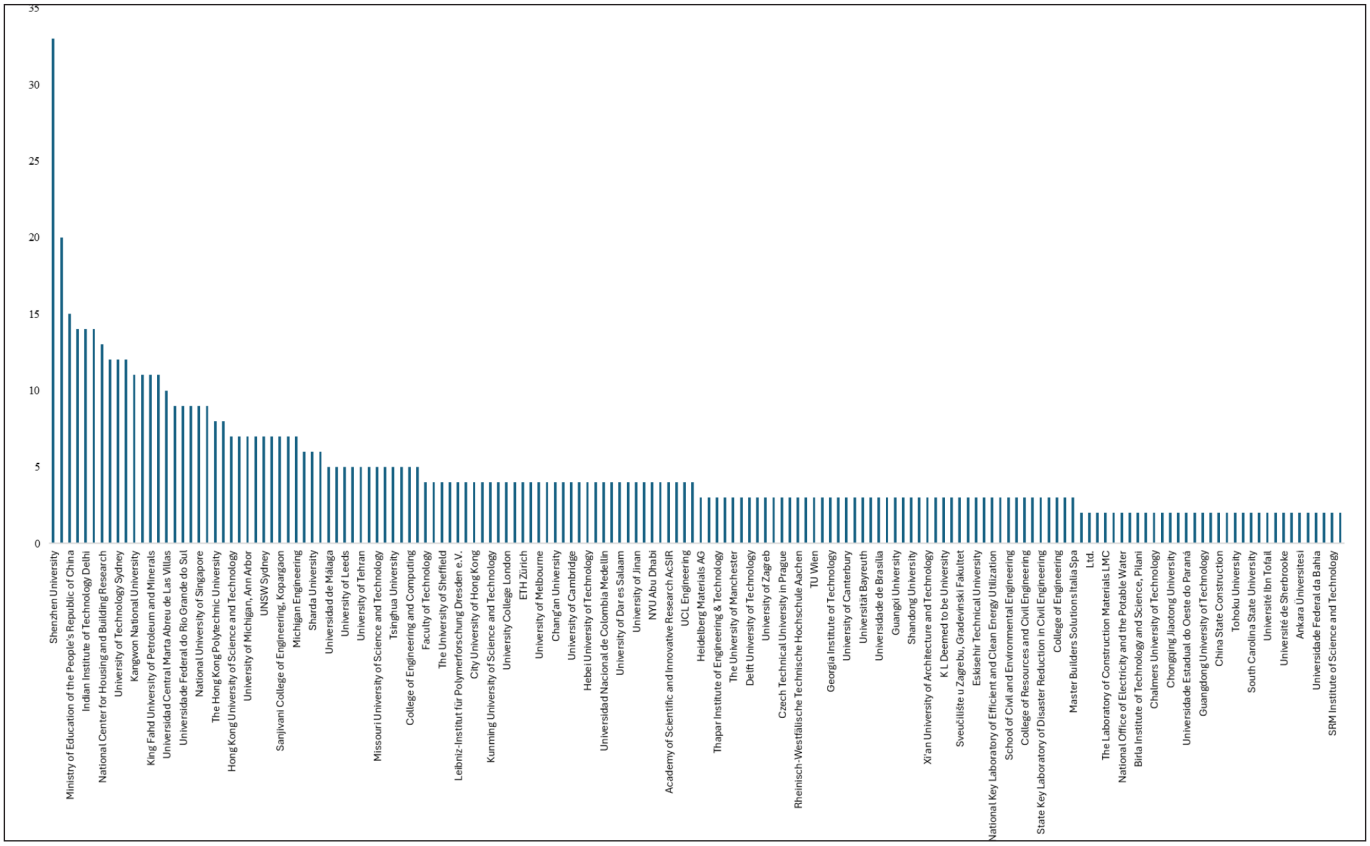


**Fig 8:** *Analysed document by affiliation*

## 5.6 Chemical admixtures and rheology

Chemical admixtures influence mechanical performance indirectly through workability, dispersion, and compaction. Calcined clay particles often have high surface area and layered morphology, which increases water and superplasticizer demand. If workability is poor, concrete may contain entrapped voids and a weaker interfacial transition zone, reducing compressive and flexural strength.

Polycarboxylate ether superplasticizers are widely used in LC3 systems, but admixture compatibility depends on clay mineralogy, ionic environment, sulphate content, and addition sequence. Future LC3 mechanical-performance papers should report admixture type, dosage, mixing procedure, slump or flow retention, and air content together with strength results.

## 5.7 Fibres, ECC, toughness, and crack control

Fibres influence LC3 mechanical behaviour differently from SCMs. While SCMs mostly alter hydration and matrix density, fibres improve post-cracking behaviour, ductility, toughness, residual flexural strength, and crack-width control. Steel, polypropylene, PVA, basalt, glass, and hybrid fibre systems have been explored in LC3-based composites and engineered cementitious composites (ECC).

Fibre reinforced LC3 systems should not be judged only by compressive strength. The most important performance indicators are flexural strength, deflection capacity, fracture energy, tensile strain capacity, residual strength, and toughness. Fibre dosage must also be balanced against workability loss and dispersion difficulty.

## 5.8 Recycled aggregates and alternative aggregates

Recycled aggregates and alternative aggregates allow LC3 to contribute not only to low-carbon binder design but also to circular construction. However, recycled aggregates may have higher porosity, higher water absorption, and residual old mortar, which can weaken the interfacial transition zone. The mechanical response depends on replacement level, presaturation, aggregate quality, paste volume, and curing.

The evidence suggests that moderate recycled aggregate contents can be compatible with LC3 if mixture design is optimized, but high replacement levels can reduce compressive strength and stiffness. Future work should focus more on tensile strength, flexural behaviour, shrinkage, creeping, bond strength, and cracking rather than compressive strength alone.

## 5.9 Curing and temperature effects

Curing is a major cross-cutting variable. LC3 hydration and pozzolanic reaction require sufficient moisture, and early-age drying can suppress reaction, increase porosity, and reduce strength. Temperature affects hydration kinetics, phase assemblage, and residual strength after thermal exposure. The included records show growing interest in microwave curing, heat curing, elevated-temperature exposure, and fire-related residual performance.

Therefore, LC3 performance should always be interpreted together with curing regime. Studies that compare material modifications without controlling curing can confuse true material effects with curing effects.

**Table 5:** *Highly cited and representative included records used to structure the synthesis*

| Title | Authors | Year | Source title | DOI | Cited by | Material category tags |
|---|---|---|---|---|---|---|
| Mechanical properties and durability performance of concretes with Limestone Calcined Clay Cement (LC3) (Dhandapani et al., 2018) | Dhandapani Y.; Sakthivel T.; Santhanam M.; Gettu R.; Pillai R.G. | 2018 | Cement and Concrete Research | 10.1016/j.cemconres.2018.02.005 | 569 | Clay mineralogy/calcination; Limestone/carbonate/gypsum/sulphate; Additional SCMs/waste powders |
| Impacting factors and properties of limestone calcined clay cements (LC3) (Scrivener et al., 2018a) | Scrivener, K; Avet, F; Marag-hechi, H; Zunino, F; Ston, J; Han-pongpun, W; Favier, A | 2019 | Green Materials | 10.1680/jgrma.18.00029 | 314 | Clay mineralogy/calcination; Limestone/carbonate/gypsum/sulphate; Chemical admixtures/rheology; Curing/temperature/high temperature |
| Assessment of pore structure evolution in the limestone calcined clay cementitious system and its implications for performance (Dhandapani and Santhanam, 2017) | Dhandapani Y.; Santhanam M. | 2017 | Cement and Concrete Composites | 10.1016/j.cemconcomp.2017.08.012 | 314 | Clay mineralogy/calcination; Limestone/carbonate/gypsum/sulphate; Additional SCMs/waste powders |
| Engineered Cementitious Composites (ECC) with limestone calcined clay cement (LC3) (Zhang et al., 2020) | Zhang D.; Jaworska B.; Zhu H.; Dahl-quist K.; Li V.C. | 2020 | Cement and Concrete Composites | 10.1016/j.cemconcomp.2020.103766 | 248 | Clay mineralogy/calcination; Limestone/carbonate/gypsum/sulphate; Chemical admixtures/rheology; Fibres/ECC/ductility |
| Performance of Limestone Calcined Clay Cement (LC3) with various kaolinite contents with respect to chloride transport (Maraghechi et al., 2018) | Maraghechi H.; Avet F.; Wong H.; Kamyab H.; Scrivener K. | 2018 | Materials and Structures | 10.1617/s11527-018-1255-3 | 235 | Clay mineralogy/calcination; Limestone/carbonate/gypsum/sulphate |
| Feasibility of using ultrahigh-volume limestone-calcined clay blend to develop sustainable medium-strength Engineered Cementitious Composites (ECC) (Yu et al., 2020) | Yu J.; Wu H.-L.; Leung C.K.Y. | 2020 | Journal of Cleaner Production | 10.1016/j.jclepro.2020.121343 | 199 | Clay mineralogy/calcination; Limestone/carbonate/gypsum/sulphate; Additional SCMs/waste powders; Fibres/ECC/ductility |
| Compressive strength and environmental impact of sustainable blended cement with high-dosage Limestone and Calcined Clay (LC2) (J. Yu et al., 2021) | Yu J.; Wu H.-L.; Mishra D.K.; Li G.; Leung C.K. | 2021 | Journal of Cleaner Production | 10.1016/j.jclepro.2020.123616 | 179 | Clay mineralogy/calcination; Limestone/carbonate/gypsum/sulphate; Additional SCMs/waste powders; Curing/temperature/high temperature |
| A study on fresh properties of limestone calcined clay blended cementitious systems (Nair et al., 2020) | Nair N.; Mo-hammed Haneefa K.; Santhanam M.; Gettu R. | 2020 | Construction and Building Materials | 10.1016/j.conbuildmat.2020.119326 | 154 | Clay mineralogy/calcination; Limestone/carbonate/gypsum/sulphate; Additional SCMs/waste powders; Chemical admixtures/rheology |
| Macro–meso–micro experimental studies of calcined clay limestone cement (LC3) paste subjected to elevated temperature (Lin et al., 2021) | Lin R.-S.; Han Y.; Wang X.-Y. | 2021 | Cement and Concrete Composites | 10.1016/j.cemconcomp.2020.103871 | 150 | Clay mineralogy/calcination; Limestone/carbonate/gypsum/sulphate; Fibres/ECC/ductility; Curing/temperature/high temperature |
| Techno-socio-economic aspects of Portland cement, Geopolymer, and Limestone Calcined Clay Cement (LC3) composite systems: A-State-of-Art-Review (Kanagaraj et al., 2023) | Kanagaraj B.; Anand N.; Samuvel Raj R.; Lubloy E. | 2023 | Construction and Building Materials | 10.1016/j.conbuildmat.2023.132484 | 136 | Clay mineralogy/calcination; Limestone/carbonate/gypsum/sulphate |
| Sprayable engineered cementitious composites (ECC) using calcined clay limestone cement (LC3) and PP fibre(Zhu et al., 2021) | Zhu H.; Yu K.; Li V.C. | 2021 | Cement and Concrete Composites | 10.1016/j.cemconcomp.2020.103868 | 128 | Clay mineralogy/calcination; Limestone/carbonate/gypsum/sulphate; Chemical admixtures/rheology; Fibres/ECC/ductility |
| Understanding of the factors slowing down metakaolin reaction in limestone calcined clay cement (LC3) at late ages (Briki et al., 2021) | Briki, Y; Avet, F; Zajac, M; Bowen, P; Ben Haha, M; Scrivener, K | 2021 | Cement and Concrete Research | 10.1016/j.cemconres.2021.106477 | 126 | Clay mineralogy/calcination; Limestone/carbonate/gypsum/sulphate |
| Novel application of low carbon limestone calcined clay cement (LC3) in expansive soil stabilization: An eco-efficient approach (Ijaz et al., 2022) | Ijaz N.; Ye W.; Rehman Z.U.; Ijaz Z. | 2022 | Journal of Cleaner Production | 10.1016/j.jclepro.2022.133492 | 122 | Clay mineralogy/calcination; Limestone/carbonate/gypsum/sulphate; Chemical admixtures/rheology; Curing/temperature/high temperature |

| | | | | | | |
|---|---|---|---|---|---|---|
| Shrinkage, hydration, and strength development of limestone calcined clay cement (LC3) with different sulfation levels (Hay et al., 2022) | Hay R.; Li L.; Celik K. | 2022 | Cement and Concrete Composites | 10.1016/j.cemconcomp.2021.104403 | 120 | Clay mineralogy/calcination; Limestone/carbonate/gypsum/sulphate; Additional SCMs/waste powders; Curing/temperature/high temperature |
| Limestone calcined clay cements (LC3) (Franco Zunino, 2021) | Zunino F.; Martirena F.; Scrivener K. | 2021 | ACI Materials Journal | 10.14359/51730422 | 113 | Clay mineralogy/calcination; Limestone/carbonate/gypsum/sulphate; Curing/temperature/high temperature |
| Printability and particle packing of 3D-printable limestone calcined clay cement composites (Long et al., 2021) | Long, WJ; Lin, C; Tao, JL; Ye, TH; Fang, Y | 2021 | Construction and Building Materials | 10.1016/j.conbuildmat.2021.122647 | 108 | Clay mineralogy/calcination; Limestone/carbonate/gypsum/sulphate; Additional SCMs/waste powders; Chemical admixtures/rheology; 3D printing/digital fabrication |
| Sustainable lightweight engineered cementitious composites using limestone calcined clay cement (LC3) (Zhou et al., 2022) | Zhou Y.; Gong G.; Xi B.; Guo M.; Xing F.; Chen C. | 2022 | Composites Part B: Engineering | 10.1016/j.compositesb.2022.110183 | 106 | Clay mineralogy/calcination; Limestone/carbonate/gypsum/sulphate; Additional SCMs/waste powders; Fibres/ECC/ductility; Curing/temperature/high temperature |
| Autogenous and total shrinkage of limestone calcined clay cement (LC3) concretes (Nguyen et al., 2022) | Nguyen Q.D.; Afroz S.; Zhang Y.; Kim T.; Li W.; Castel A. | 2022 | Construction and Building Materials | 10.1016/j.conbuildmat.2021.125720 | 105 | Clay mineralogy/calcination; Limestone/carbonate/gypsum/sulphate; Curing/temperature/high temperature; Prediction/ML/optimization |
| Assessing the effect of alkanolamine grinding aids in limestone calcined clay cements hydration (Zunino and Scrivener, 2021b) | Zunino, F; Scrivener, K | 2021 | Construction and Building Materials | 10.1016/j.conbuildmat.2020.121293 | 99 | Clay mineralogy/calcination; Limestone/carbonate/gypsum/sulphate; Chemical admixtures/rheology |
| Strengthening the performance of limestone-calcined clay cement (LC3) using nano silica (Lin et al., 2022) | Lin R.-S.; Oh S.; Du W.; Wang X.-Y. | 2022 | Construction and Building Materials | 10.1016/j.conbuildmat.2022.127723 | 95 | Clay mineralogy/calcination; Limestone/carbonate/gypsum/sulphate; Nano additives; Curing/temperature/high temperature |
| Investigating the potential of low-grade calcined clays to produce durable LC3 binders against chloride ions attack (Zolfagharnasab et al., 2021) | Zolfagharnasab A.; Ramezanianpour A.A.; Bahman-Zadeh F. | 2021 | Construction and Building Materials | 10.1016/j.conbuildmat.2021.124541 | 88 | Clay mineralogy/calcination; Limestone/carbonate/gypsum/sulphate; Additional SCMs/waste powders; Curing/temperature/high temperature |
| Mechanical, environmental and economic performance of sustainable Grade 45 concrete with ultrahigh-volume Lime-stone-Calcined Clay (LCC) (Jing Yu et al., 2021) | Yu J.; Mishra D.K.; Hu C.; Leung C.K.Y.; Shah S.P. | 2021 | Resources, Conservation and Recycling | 10.1016/j.resconrec.2021.105846 | 84 | Clay mineralogy/calcination; Limestone/carbonate/gypsum/sulphate; Additional SCMs/waste powders |
| Design, dynamic performance and ecological efficiency of fibre-reinforced mortars with different binder systems: Ordinary Portland cement, limestone calcined clay cement and alkali-activated slag (Long et al., 2022) | Long W.-J.; Wu Z.; Khayat K.H.; Wei J.; Dong B.; Xing F.; Zhang J. | 2022 | Journal of Cleaner Production | 10.1016/j.jclepro.2022.130478 | 82 | Clay mineralogy/calcination; Limestone/carbonate/gypsum/sulphate; Additional SCMs/waste powders; Chemical admixtures/rheology; Fibres/ECC/ductility |
| Influence of clay calcination method on the mechanical properties and chloride diffusion resistance of limestone calcined clay cement (LC3) concrete (Nguyen et al., 2020) | Nguyen Q.D.; Afroz S.; Castel A. | 2020 | Journal of Marine Science and Engineering | 10.3390/jmse8050301 | 82 | Clay mineralogy/calcination; Limestone/carbonate/gypsum/sulphate; Curing/temperature/high temperature |
| Thermal stability of limestone calcined clay cement (LC3) at moderate temperatures 100–400 °C (Cao et al., 2023) | Cao Y.; Wang Y.; Zhang Z.; Ma Y.; Wang H. | 2023 | Cement and Concrete Composites | 10.1016/j.cemconcomp.2022.104832 | 80 | Clay mineralogy/calcination; Limestone/carbonate/gypsum/sulphate; Fibres/ECC/ductility; Curing/temperature/high temperature |
| Effects of water-to-binder ratios (w/b) and superplasticizer on physicochemical, microstructural, and mechanical evolution of limestone calcined clay cement (LC3) (Hay and Celik, 2023) | Hay R.; Celik K. | 2023 | Construction and Building Materials | 10.1016/j.conbuildmat.2023.131529 | 75 | Clay mineralogy/calcination; Limestone/carbonate/gypsum/sulphate; Chemical admixtures/rheology; Curing/temperature/high temperature |
| Quaternary blended limestone-calcined clay cement concrete incorporating fly ash (Dixit et al., 2021) | Dixit A.; Du H.; Dang J.; Pang S.D. | 2021 | Cement and Concrete Composites | 10.1016/j.cemconcomp.2021.104174 | 74 | Clay mineralogy/calcination; Limestone/carbonate/gypsum/sulphate; Additional SCMs/waste powders; Chemical admixtures/rheology; Curing/temperature/high temperature |

| | | | | | | |
|---|---|---|---|---|---|---|
| Physico-chemical properties of Kenyan made calcined Clay - Limestone cement (LC3) (Marangu, 2020) | Marangu J.M. | 2020 | Case Studies in Construction Materials | 10.1016/j.cscm.2020.e00333 | 71 | Clay mineralogy/calcination; Limestone/carbonate/gypsum/sulphate; Additional SCMs/waste powders; Curing/temperature/high temperature |
| Strength-promoting mechanism of alkanolamines on limestone-calcined clay cement and the role of sulphate (Huang et al., 2021) | Huang, H; Li, XR; Avet, F; Hanpongpun, W; Scrivener, K | 2021 | Cement And Concrete Research | 10.1016/j.cemconres.2021.106527 | 70 | Clay mineralogy/calcination; Limestone/carbonate/gypsum/sulphate |
| Exploring the role of dilutive effects on microstructural development and hydration kinetics of limestone calcined clay cement (LC3) made of low-grade raw materials (Ahmed et al., 2023) | Ahmed, AH; Nune, S; Liebscher, M; Köberle, T; Willomitzer, A; Noack, I; Butler, M; Mechtcherine, V | 2023 | Journal Of Cleaner Production | 10.1016/j.jclepro.2023.139438 | 68 | Clay mineralogy/calcination; Limestone/carbonate/gypsum/sulphate; Additional SCMs/waste powders |
| Influence of limestone calcined clay cement on properties of 3D printed concrete for sustainable construction (Ibrahim et al., 2023) | Ibrahim K.A.; van Zijl G.P.A.G.; Babafemi A.J. | 2023 | Journal of Building Engineering | 10.1016/j.jobe.2023.106186 | 67 | Clay mineralogy/calcination; Limestone/carbonate/gypsum/sulphate; Chemical admixtures/rheology; Fibres/ECC/ductility; Curing/temperature/high temperature; 3D printing/digital fabrication |
| A fresh view on limestone calcined clay cement (LC3) pastes (Ez-zaki et al., 2021) | Ez-zaki H.; Marangu J.M.; Bellotto M.; Dalconi M.C.; Artioli G.; Valentini L. | 2021 | Materials | 10.3390/ma14113037 | 65 | Clay mineralogy/calcination; Limestone/carbonate/gypsum/sulphate; Chemical admixtures/rheology; Curing/temperature/high temperature |
| Multiscale assessment of performance of limestone calcined clay cement (LC3) reinforced with virgin and recycled carbon fibres (H. Li et al., 2023) | Li H.; Yang J.; Wang L.; Li L.; Xia Y.; Köberle T.; Dong W.; Zhang N.; Yang B.; Mechtcherine V. | 2023 | Construction and Building Materials | 10.1016/j.conbuildmat.2023.133228 | 63 | Clay mineralogy/calcination; Limestone/carbonate/gypsum/sulphate; Chemical admixtures/rheology; Fibres/ECC/ductility; Curing/temperature/high temperature |
| Exploring low-grade clay minerals diving into limestone calcined clay cement (LC3): Characterization − Hydration – Performance (Blouch et al., 2023a) | Blouch N.; Rashid K.; Ju M. | 2023 | Journal of Cleaner Production | 10.1016/j.jclepro.2023.139065 | 63 | Clay mineralogy/calcination; Limestone/carbonate/gypsum/sulphate; Fibres/ECC/ductility; Curing/temperature/high temperature |
| Performance evaluation of recycled aggregate concrete incorporating limestone calcined clay cement (LC3) (Guo et al., 2022) | Guo M.; Gong G.; Yue Y.; Xing F.; Zhou Y.; Hu B. | 2022 | Journal of Cleaner Production | 10.1016/j.jclepro.2022.132820 | 62 | Clay mineralogy/calcination; Limestone/carbonate/gypsum/sulphate; Recycled aggregates/alternative aggregates |
| Influence of temperature on hydration and microstructure properties of limestone-calcined clay blended cement (Mishra et al., 2019) | Mishra, G; Emmanuel, AC; Bishnoi, S | 2019 | Materials And Structures | 10.1617/s11527-019-1390-5 | 62 | Clay mineralogy/calcination; Limestone/carbonate/gypsum/sulphate; Additional SCMs/waste powders; Curing/temperature/high temperature |
| Prioritization of low-grade kaolinite and mixed clays for performance evaluation of Limestone Calcined Clay Cement (LC3): Multi-criteria assessment (Blouch et al., 2023b) | Blouch, N; Rashid, K; Zafar, I; Ltifi, M; Ju, M | 2023 | Applied clay science | 10.1016/j.clay.2023.107080 | 59 | Clay mineralogy/calcination; Limestone/carbonate/gypsum/sulphate; Additional SCMs/waste powders |
| Development of limestone calcined clay cement concrete in South China and its bond behaviour with steel reinforcement (Huang et al., 2020) | Huang Z.Y.; Huang Y.S.; Liao W.-Y.; Han N.X.; Zhou Y.-W.; Xing F.; Sui T.B.; Wang B.; Ma H.Y. | 2020 | Journal of Zhejiang University: Science A | 10.1631/jzus.a2000163 | 58 | Clay mineralogy/calcination; Limestone/carbonate/gypsum/sulphate; Chemical admixtures/rheology |
| Natural kenaf fibre and LC3 binder for sustainable fibre-reinforced cementitious composite: A review (Baghban and Mahjoub, 2020) | Baghban M.H.; Mahjoub R. | 2020 | Applied Sciences | 10.3390/app10010357 | 56 | Clay mineralogy/calcination; Limestone/carbonate/gypsum/sulphate; Fibres/ECC/ductility |
| Limestone calcined clay cement (LC3): A sustainable solution for mitigating environmental impact in the construction sector (Kanagaraj et al., 2024) | Kanagaraj B.; Anand N.; Johnson Alengaram U.; Samuvel Raj R.; Karthick S. | 2024 | Resources, Conservation and Recycling Advances | 10.1016/j.rcradv.2023.200197 | 55 | Clay mineralogy/calcination; Limestone/carbonate/gypsum/sulphate; Chemical admixtures/rheology; Recycled aggregates/alternative aggregates |

| | | | | | | |
|---|---|---|---|---|---|---|
| Performance assessment of LC3 concrete structures considering life-cycle cost and environmental impacts (Huang et al., 2024) | Huang X.; Jiao Z.; Xing F.; Sui L.; Hu B.; Zhou Y. | 2024 | Journal of Cleaner Production | 10.1016/j.jclepro.2023.140380 | 55 | Clay mineralogy/calcination; Limestone/carbonate/gypsum/sulphate; Fibres/ECC/ductility; Recycled aggregates/alternative aggregates |
| 3D printing of limestone-calcined clay cement: A review of its potential implementation in the construction industry (Al-Noaimat et al., 2023) | Al-Noaimat, YA; Chougan, M; Al-kheetan, MJ; Al-Mandhari, O; Al-Saidi, W; Al-Maqbali, M; Al-Hosni, H; Ghaffar, SH | 2023 | Results in Engineering | 10.1016/j.rineng.2023.101115 | 55 | Clay mineralogy/calcination; Limestone/carbonate/gypsum/sulphate; Additional SCMs/waste powders; Chemical admixtures/rheology; 3D printing/digital fabrication |
| Concrete performance of limestone calcined clay cement (LC3) compared with conventional cements (Avet et al., 2019) | Avet F.; Sofia L.; Scrivener K. | 2019 | Advances in Civil Engineering Materials | 10.1520/acem20190052 | 55 | Clay mineralogy/calcination; Limestone/carbonate/gypsum/sulphate; Additional SCMs/waste powders; Chemical admixtures/rheology |
| Mechanical properties and hydration of ultra-high-performance seawater sea-sand concrete (UHPSSC) with limestone calcined clay cement (LC3) (Wang and Huang, 2023) | Wang J.; Huang Y. | 2023 | Construction and Building Materials | 10.1016/j.conbuildmat.2023.130950 | 53 | Clay mineralogy/calcination; Limestone/carbonate/gypsum/sulphate; Additional SCMs/waste powders; Curing/temperature/high temperature |
| Optimization of mechanical performance of limestone calcined clay cement: Effects of calcination temperature of nano sized tubular halloysite, gypsum content, and water/binder ratio (Yu et al., 2023) | Yu, T; Zhang, BF; Yuan, P; Guo, HZ; Liu, D; Chen, JR; Liu, HM; Belaroui, LS | 2023 | Construction And Building Materials | 10.1016/j.conbuildmat.2023.131709 | 50 | Clay mineralogy/calcination; Limestone/carbonate/gypsum/sulphate; Additional SCMs/waste powders; Nano additives; Curing/temperature/high temperature; Prediction/ML/optimization |
| Investigation of using limestone calcined clay cement (LC3) in engineered cementitious composites: The effect of propylene fibres and the curing system (Liu et al., 2021) | Liu, J; Zhang, WZ; Li, ZL; Jin, HS; Liu, W; Tang, LP | 2021 | Journal Of Materials Research and Technology-J | 10.1016/j.jmrt.2021.09.023 | 50 | Clay mineralogy/calcination; Limestone/carbonate/gypsum/sulphate; Additional SCMs/waste powders; Fibres/ECC/ductility; Curing/temperature/high temperature; Prediction/ML/optimization |
| Performance of limestone calcined clay cement (LC3) incorporating low-grade marine clay (Hu et al., 2024) | Hu Y.; Xiong L.; Yan Y.; Geng G. | 2024 | Case Studies in Construction Materials | 10.1016/j.cscm.2024.e03283 | 49 | Clay mineralogy/calcination; Limestone/carbonate/gypsum/sulphate; Curing/temperature/high temperature |
| Exploring sulphate optimization techniques in Limestone Calcined Clay Cements (LC3): limitations and insights (Silva et al., 2024) | Silva M.R.C.D.; Andrade Neto J.D.S.; Walkley B.; Kirchheim A.P. | 2024 | Cement and Concrete Research | 10.1016/j.cemconres.2023.107375 | 48 | Clay mineralogy/calcination; Limestone/carbonate/gypsum/sulphate; Curing/temperature/high temperature; Prediction/ML/optimization |
| Contribution to low-carbon cement studies: Effects of silica fume, fly ash, sugarcane bagasse ash and acai stone ash incorporation in quaternary blended limestone-calcined clay cement concretes (Tino Balestra et al., 2023) | Tino Balestra C.E.; Garcez L.R.; Couto da Silva L.; Veit M.T.; Jubanski E.; Nakano A.Y.; Pietrobelli M.H.; Schneider R.; Ramirez Gil M.A. | 2023 | Environmental Development | 10.1016/j.envdev.2022.100792 | 48 | Clay mineralogy/calcination; Limestone/carbonate/gypsum/sulphate; Additional SCMs/waste powders; Chemical admixtures/rheology |
| Shrinkage of blended cement concrete with fly ash or limestone calcined clay (Afroz et al., 2023) | Afroz S.; Zhang Y.; Nguyen Q.D.; Kim T.; Castel A. | 2023 | Materials and Structures | 10.1617/s11527-023-02099-8 | 48 | Clay mineralogy/calcination; Limestone/carbonate/gypsum/sulphate; Additional SCMs/waste powders |
| Physicochemical properties of limestone calcined clay cement (LC3) concrete made using Saudi clays (Abdulqader et al., 2023) | Abdulqader M.; Khalid H.R.; Ibrahim M.; Adekunle S.K.; Al-Osta M.A.; Ahmad S.; Sajid M. | 2023 | Journal of Materials Research and Technology | 10.1016/j.jmrt.2023.06.114 | 48 | Clay mineralogy/calcination; Limestone/carbonate/gypsum/sulphate; Chemical admixtures/rheology |
| Reducing clinker factor in limestone calcined clay-slag cement using C-S-H seeding – A way towards sustainable binder (X. Li et al., 2023) | Li X.; Dengler J.; Hesse C. | 2023 | Cement and Concrete Research | 10.1016/j.cemconres.2023.107151 | 47 | Clay mineralogy/calcination; Limestone/carbonate/gypsum/sulphate; Additional SCMs/waste powders; Chemical admixtures/rheology; Curing/temperature/high temperature |

| | | | | | | |
|---|---|---|---|---|---|---|
| Hydration behaviour of limestone-calcined clay and limestone-slag blends in ternary cement (Parashar and Bishnoi, 2021) | Parashar A.; Bishnoi S. | 2021 | RILEM Technical Letters | 10.21809/rilemtechlett.2021.134 | 47 | Clay mineralogy/calcination; Limestone/carbonate/gypsum/sulphate; Additional SCMs/waste powders; Curing/temperature/high temperature |
| Carbon-negative heat-stored limestone calcined clay cement mortar containing form-stable phase change materials (Yu et al., 2024) | Yu, KY; Liu, CC; Li, L; Tian, WC; Yang, YZ; Liu, YS | 2024 | Journal of Cleaner Production | 10.1016/j.jclepro.2024.140703 | 46 | Clay mineralogy/calcination; Limestone/carbonate/gypsum/sulphate; Curing/temperature/high temperature; Prediction/ML/optimization |
| A Review on Hydration Process and Setting Time of Limestone Calcined Clay Cement (LC3) (Zhao and Zhang, 2023) | Zhao Y.; Zhang Y. | 2023 | Solids | 10.3390/solids4010003 | 46 | Clay mineralogy/calcination; Limestone/carbonate/gypsum/sulphate; Chemical admixtures/rheology |
| Performance assessment of limestone calcined clay cement (LC3)-Based lightweight green mortars incorporating recycled waste aggregate (Alghamdi et al., 2023) | Alghamdi H.; Shoukry H.; Abadel A.A.; Khawaji M. | 2023 | Journal of Materials Research and Technology | 10.1016/j.jmrt.2023.01.133 | 46 | Clay mineralogy/calcination; Limestone/carbonate/gypsum/sulphate; Additional SCMs/waste powders; Recycled aggregates/alternative aggregates; Curing/temperature/high temperature |
| Performance of limestone-calcined clay cement mortar incorporating high volume ferrochrome waste slag aggregate (Shoukry et al., 2022) | Shoukry H.; Perumal P.; Abadel A.; Alghamdi H.; Alamri M.; Abdel-Gawwad H.A. | 2022 | Construction and Building Materials | 10.1016/j.conbuildmat.2022.128928 | 44 | Clay mineralogy/calcination; Limestone/carbonate/gypsum/sulphate; Additional SCMs/waste powders; Chemical admixtures/rheology; Recycled aggregates/alternative aggregates |
| Mechanics, hydration phase and pore development of embodied energy and carbon composites based on ultrahigh-volume low-carbon cement with limestone calcined clay (Liu et al., 2022) | Liu, J; Zhang, WZ; Li, ZL; Jin, HS; Tang, LP | 2022 | Case Studies in Construction Materials | 10.1016/j.cscm.2022.e01299 | 42 | Clay mineralogy/calcination; Limestone/carbonate/gypsum/sulphate; Additional SCMs/waste powders; Fibres/ECC/ductility |
| Mechanical, environmental, and economic performance of engineered cementitious composite incorporated limestone calcined clay cement: A review (Al-Fakih et al., 2023) | Al-Fakih, A; Al-Shugaa, MA; Al-Osta, MA; Thomas, BS | 2023 | Journal of Building Engineering | 10.1016/j.jobe.2023.107901 | 41 | Clay mineralogy/calcination; Limestone/carbonate/gypsum/sulphate; Fibres/ECC/ductility |
| Sustainability enhancement of calcined clay and limestone powder hybrid ultra-high-performance concrete using belite-rich Portland cement (Xuan et al., 2022) | Xuan M.-Y.; Bae S.C.; Kwon S.-J.; Wang X.-Y. | 2022 | Construction and Building Materials | 10.1016/j.conbuildmat.2022.128932 | 40 | Clay mineralogy/calcination; Limestone/carbonate/gypsum/sulphate; Curing/temperature/high temperature |
| Influence of Low- to Medium-Kaolinite Clay on the Durability of Limestone Calcined Clay Cement (LC3) Concrete (Ram et al., 2022) | Ram K.; Flegar M.; Serdar M.; Scrivener K. | 2023 | Materials | 10.3390/ma16010374 | 39 | Clay mineralogy/calcination; Limestone/carbonate/gypsum/sulphate |
| Mechanical Performance and Physico-Chemical Properties of Limestone Calcined Clay Cement (LC3) in Malawi (Kafodya et al., 2023) | Kafodya, I; Basuroy, D; Marangu, JM; Kululanga, G; Maddalena, R; Novelli, VI | 2023 | BUILDINGS | 10.3390/buildings13030740 | 38 | Clay mineralogy/calcination; Limestone/carbonate/gypsum/sulphate; Additional SCMs/waste powders |
| Tailoring crack width control of LC3-based engineered cementitious composites (ECC) via fibre hybridization: From micromechanics design to macro investigation (Hou and Li, 2023) | Hou, MJ; Li, VC | 2023 | Materials & Design | 10.1016/j.matdes.2023.112433 | 37 | Fibres/ECC/ductility |
| Limestone calcined clay cement: mechanical properties, crystallography, and microstructure development (Sui et al., 2023) | Sui, H; Hou, PK; Liu, YM; Sagoe-Crentsil, K; de Souza, FB; Duan, WH | 2023 | Journal of Sustainable Cement-Based Materials | 10.1080/21650373.2022.2074911 | 37 | Clay mineralogy/calcination; Limestone/carbonate/gypsum/sulphate; Recycled aggregates/alternative aggregates |
| An innovative strategy for CO2 conversion and utilization: Semi-wet carbonation pretreatment of wollastonite to prepare carbon-fixing products and produce LC3 (Wang et al., 2025) | Wang Y.-S.; Meng L.-Y.; Chen L.; Wang X.-Y. | 2025 | Cement and Concrete Composites | 10.1016/j.cemconcomp.2025.106050 | 36 | Clay mineralogy/calcination; Limestone/carbonate/gypsum/sulphate; Additional SCMs/waste powders; Chemical admixtures/rheology |
| Comparative performance of limestone calcined clay and limestone calcined laterite blended cement concrete (Musbau et al., 2021) | Musbau K.D.; Kolawole J.T.; Babafemi A.J.; Olalusi O.B. | 2021 | Cleaner Engineering and Technology | 10.1016/j.clet.2021.100264 | 36 | Clay mineralogy/calcination; Limestone/carbonate/gypsum/sulphate; Chemical admixtures/rheology |

| | | | | | | |
|---|---|---|---|---|---|---|
| Investigation of the hydrate formation and mechanical performance of limestone calcined clay cement paste incorporating nano CaCO3 and nano SiO2 as partial limestone substitutes (Kim et al., 2024) | Kim G.; Cho S.; Moon J.; Suh H.; Her S.; Sim S.; Bae S. | 2024 | Construction and Building Materials | https://doi.org/10.1016/j.conbuildmat.2024.135335 | 35 | Clay mineralogy/calcination; Limestone/carbonate/gypsum/sulphate; Additional SCMs/waste powders; Nano additives |
| Comparative environmental assessment of limestone calcined clay cements and typical blended cements (Martinez et al., 2023) | Martinez D.M.; Horvath A.; Monteiro P.J.M. | 2023 | Environmental Research Communications | 10.1088/2515-7620/acccd8 | 35 | Clay mineralogy/calcination; Limestone/carbonate/gypsum/sulphate; Additional SCMs/waste powders; Prediction/ML/optimization |
| Experimental studies on durability performances of ultra-lightweight low-carbon LC3 cement composites against chloride ingression and carbonation (Huang et al., 2023) | HUANG Z.; LIANG T.; CHEN L. | 2023 | Construction and Building Materials | https://doi.org/10.1016/j.conbuildmat.2023.132340 | 35 | Clay mineralogy/calcination; Limestone/carbonate/gypsum/sulphate; Additional SCMs/waste powders; Chemical admixtures/rheology |
| Effect of carbonation on chloride binding capacity of limestone calcined clay cement (LC3) and binary pastes (Bahman-Zadeh et al., 2022) | Bahman-Zadeh F.; Ramezanianpour A.A.; Zolfagharnasab A. | 2022 | Journal of Building Engineering | 10.1016/j.jobe.2022.104447 | 35 | Clay mineralogy/calcination; Limestone/carbonate/gypsum/sulphate; Additional SCMs/waste powders |
| Phase and microstructure evolutions in LC3 binders by multi-technique approach including synchrotron microtomography (Bernal et al., 2021) | Bernal, IMR; Shirani, S; Cuesta, A; Santacruz, I; Aranda, MAG | 2021 | Construction and Building Materials | 10.1016/j.conbuildmat.2021.124054 | 35 | Clay mineralogy/calcination; Limestone/carbonate/gypsum/sulphate; Curing/temperature/high temperature |
| The microstructure and mechanical properties of cementitious materials comprised of limestone, calcined clay and clinker (Li, 2019) | Qinfei L.; Han W.; Pengkun H.; Heng C.; Yang W.; | 2019 | Ceramics - Silikaty | 10.13168/cs.2019.0031 | 35 | Clay mineralogy/calcination; Limestone/carbonate/gypsum/sulphate; Additional SCMs/waste powders; Curing/temperature/high temperature |
| Hardening properties and microstructure of 3D printed engineered cementitious composites based on limestone calcined clay cement (Wang et al., 2024) | Wang Y.; Chen M.; Zhang T.; Zhang M. | 2024 | Cement and Concrete Composites | 10.1016/j.cemconcomp.2024.105641 | 34 | Clay mineralogy/calcination; Limestone/carbonate/gypsum/sulphate; Fibres/ECC/ductility; 3D printing/digital fabrication |
| Synergic effect of triethanolamine and C-S-H seeding on early hydration of the limestone calcined clay cement in UHPC (Luan, 2023) | Luan C.; Wang J.; Zhou Z. | 2023 | Construction and Building Materials | https://doi.org/10.1016/j.conbuildmat.2023.132675 | 34 | Clay mineralogy/calcination; Limestone/carbonate/gypsum/sulphate; Additional SCMs/waste powders; Chemical admixtures/rheology; Curing/temperature/high temperature |
| Multi-characterizations of the hydration, microstructure, and mechanical properties of a biochar-limestone calcined clay cement (LC3) mixture (Wang and Wang, 2023) | Wang, YS; Wang, XY | 2023 | Journal Of Materials Research and Technology | https://doi.org/10.1016/j.jmrt.2023.04.033 | 34 | Clay mineralogy/calcination; Limestone/carbonate/gypsum/sulphate; Additional SCMs/waste powders; Curing/temperature/high temperature |

## 5.10 Brief comparison with geopolymer systems

LC3 and geopolymer/alkali-activated systems may use similar aluminosilicate resources, such as fly ash, slag, metakaolin, or waste powders, but their reaction mechanisms are fundamentally different. LC3 remains a hydraulic blended cement system involving clinker hydration, pozzolanic reaction, limestone-alumina synergy, and sulphate-controlled phase development. Geopolymers rely on alkali activation and gel formation governed by activator type, alkalinity, silicate modulus, and curing temperature. Therefore, material-performance relationships should not be transferred directly from geopolymer systems to LC3 without mechanism-based validation. For this reason, geopolymer studies were not included in the systematic dataset, but they provide useful conceptual comparison for future low-carbon binder selection.

# 6 SUMMARY OF MATERIAL EFFECTS

The overall synthesis of material effects is presented in *Table 6*. This table integrates evidence from the reviewed studies by linking each material factor with its typical mechanical influence, dominant mechanism, and evidence strength. The strongest and most consistent evidence is associated with high-kaolinite calcined clay, optimized limestone content, optimized gypsum/sulphate balance, and adequate curing. These factors directly influence the main LC3 hydration mechanisms, including pozzolanic reaction, aluminate reaction, carboaluminate formation, ettringite stability, pore refinement, and strength development.

Thus, *Table 6* provides the final evidence-based framework of the review, showing that future LC3 mixture design should simultaneously consider clay reactivity, limestone sulphate balance, admixture compatibility, curing regime, pore refinement, and functional additives to achieve reliable mechanical performance.

# 7 RESEARCH GAPS

The following research gaps were identified from the reviewed literature at the moment:

1) Clay reporting remains inconsistent. Many records do not report complete mineralogy, kaolinite content, amorphous content, calcination temperature, calcination duration, fineness, or water demand.
2) Compressive strength is overrepresented. Tensile strength, flexural strength, elastic modulus, shrinkage, creep, frac-

**Table 6:** Synthesis of material effects on LC3 mechanical performance

| Material factor | General effect | Dominant mechanism | Evidence strength |
|---|---|---|---|
| High kaolinite calcined clay | Usually positive for strength | Reactive alumina/silica, pozzolanic reaction, carboaluminate formation | Strong |
| Low grade/mixed clay | Mixed but promising | Depends on mineralogy, calcination, fineness, water demand, and sulphate balance | Moderate |
| Optimized limestone | Positive | Filler effect, nucleation, carbonate-alumina synergy | Strong |
| Excess limestone | Negative or mixed | Dilution dominates if reactive alumina is insufficient | Moderate |
| Optimized gypsum/sulphate | Positive | Controls aluminate reaction, ettringite/carboaluminate balance, early strength | Strong |
| Fly ash/slag/silica fume/waste powders | Material-specific | Later reaction, packing, dilution, sustainability benefit | Moderate |
| Nano silica | Positive at optimized dosage | Hydration acceleration, nucleation, pore refinement | Moderate |
| Superplasticizers/PCE (Polycarboxylate Ether) | Indirectly positive | Improved dispersion, workability, compaction, shrinkage and water reduction | Moderate |
| Fibres | Positive mainly for flexural/toughness | Crack bridging and post cracking response | Moderate |
| Recycled aggregates | Mixed | ITZ and porosity effects; depends on aggregate quality and replacement level | Emerging |
| Curing | Strongly positive when adequate | Sustains hydration and pozzolanic reaction | Strong |

ture energy, bond strength, and structural-scale behaviour are reported less consistently.

3) Sulphate balance is often underreported, even though gypsum dosage can strongly affect early hydration and strength development.
4) Multi-SCM LC3 systems are promising but insufficiently standardized; systematic comparisons across SCM type, dosage, age, and curing are still limited.
5) Nano additives require concrete-scale validation. Many improvements are shown at paste or mortar scale, but dispersion, cost, workability, and scale up remain barriers.
6) Fibre-reinforced LC3 needs more structural testing of beams, slabs, crack widths, residual strength, and serviceability.
7) Recycled aggregate LC3 needs more long-term mechanical data, especially shrinkage, creep, stiffness, and bond behaviour.
8) Machine learning and optimization models are emerging but require high-quality datasets with consistent material characterization and testing ages.

# 8 FUTURE DIRECTION FOR RESEARCH

The proposed future research agenda is presented in *Table 7.* This agenda synthesizes the main knowledge gaps identified throughout the review and translates them into targeted research directions. The first group of recommendations concerns the fundamental design of LC3 binders, particularly clay classification and sulphate optimization. Because LC3 performance depends strongly on clay mineralogy, kaolinite content, calcination conditions, particle fineness, water demand, and gypsum dosage, future studies should develop clay-specific quality indices and report sulphate optimization using consistent calorimetry, strength, and TGA based methods.

The second group of recommendations in *Table 7* concerns the expansion of LC3 performance assessment beyond compressive strength. Although compressive strength remains the most reported property, structural use of LC3 requires reliable data on tensile strength, flexural strength, elastic modulus, shrinkage, creep, fracture, bond, toughness, and ductility. Moreover, concrete-scale validation remains essential because paste- and mortar-level findings cannot always be transferred directly to concrete systems. The table therefore highlights the need for realistic LC3 concrete mixtures with documented workability, compaction, curing regime, and long-term performance.

**Table 7:.** Future research agenda

| Research content/direction | Recommendation |
|---|---|
| Clay classification | Create LC3 specific clay quality indices including mineralogy, kaolinite content, calcination window, fineness, and water demand |
| Sulphate optimisation | Report gypsum dosage and use calorimetry/strength/TGA based optimization for different clays |
| Mechanical properties | Move beyond compressive strength to tensile, flexural, modulus, shrinkage, creep, fracture, bond, and toughness |
| Concrete scale validation | Test realistic concrete mixtures, not only paste/mortar, with documented workability and compaction |
| Functional additives | Evaluate nano silica, PCEs, fibres, recycled materials, and SCMs using dose response designs. |
| Durability-mechanical coupling | Study how cracking, shrinkage, and stiffness influence chloride/carbonation resistance |
| Data-driven design | Develop open datasets and ML models for LC3 mix design using standardized variables and uncertainty reporting |
| LC3 and geopolymer comparison | Compare low carbon binders mechanistically, not only by strength or CO2 reduction |

The final group of recommendations addresses emerging and application oriented research directions. Functional additives, including nano silica, PCEs, fibres, recycled materials,

and additional SCMs, should be investigated through systematic dose response studies rather than isolated mixture trials. Similarly, durability and mechanical performance should be studied together, especially where shrinkage, cracking, chloride ingress, and carbonation interact. Data-driven design and machine learning (ML) models are also promising, but they require open datasets, standardized variables, and uncertainty reporting. Therefore, *Table 7* functions as the concluding roadmap of the review, showing that LC3 development should progress from single factor material studies toward integrated, multi objective binder and concrete design.

# 9 CONCLUSIONS

Following conclusions can be drawn from the presented literature review on Material Factors Governing the Mechanical Properties of LC3 Based Cementitious Systems:

1) The systematic search of Scopus and Web of Science identified 1275 records; after DOI/title deduplication and title/abstract screening, 448 LC3-focused records were retained.
2) LC3 mechanical performance is governed by an integrated chain of material variables rather than by clinker replacement level alone. The most important variables are clay mineralogy, calcined kaolinite content, calcination quality, limestone-carbonate synergy, sulphate balance, fineness, water demand, curing, and admixture compatibility.
3) High reactivity calcined clays generally improve strength, but their benefits can be limited by high water demand, poor dispersion, or non-optimized sulphate balance. Low grade clays can be viable when properly characterized and processed.
4) Limestone contributes physically and chemically through filler/nucleation effects and carboaluminate formation. However, excessive limestone may reduce strength if the system lacks sufficient reactive alumina.
5) Additional SCMs, waste powders, nano silica, fibres, recycled aggregates, and chemical admixtures offer promising routes for LC3 optimization, but their effects are highly system-dependent and require standardized reporting.
6) Future LC3 mechanical properties research should emphasize tensile/flexural properties, modulus, shrinkage, creep, toughness, bond behaviour, structural elements, and open datasets for predictive mix design.

# ACKNOWLEDGEMENT

The authors acknowledge the support of the Central Europe Leuven Strategic Alliance (grant number: CELSA/25/10).

# REFERENCES

Abdulqader, M., Khalid, H.R., Ibrahim, M., Adekunle, S.K., Al-Osta, M.A., Ahmad, S., Sajid, M., 2023. Physicochemical properties of limestone calcined clay cement (LC3) concrete made using Saudi clays. J. Mater. Res. Technol. 25, 2769–2783. https://doi.org/10.1016/j.jmrt.2023.06.114

Afroz, S., Zhang, Y., Nguyen, Q.D., Kim, T., Castel, A., 2023. Shrinkage of blended cement concrete with fly ash or limestone calcined clay. Mater Struct 56, 15. https://doi.org/10.1617/s11527-023-02099-8

Ahmed, A.H., Nune, S., Liebscher, M., Köberle, T., Willomitzer, A., Noack, I., Butler, M., Mechtcherine, V., 2023. Exploring the role of dilutive effects on microstructural development and hydration kinetics of limestone calcined clay cement (LC3) made of low-grade raw materials. Journal of Cleaner Production 428, 139438. https://doi.org/10.1016/j.jclepro.2023.139438

Al-Fakih, A., A. Al-Shugaa, M., A. Al-Osta, M., Thomas, B.S., 2023. Mechanical, environmental, and economic performance of engineered cementitious composite incorporated limestone calcined clay cement: A review. Journal of Building Engineering 79, 107901. https://doi.org/10.1016/j.jobe.2023.107901

Alghamdi, H., Shoukry, H., Abadel, A.A., Khawaji, M., 2023. Performance assessment of limestone calcined clay cement (LC3)-Based lightweight green mortars incorporating recycled waste aggregate. Journal of Materials Research and Technology 23, 2065–2074. https://doi.org/10.1016/j.jmrt.2023.01.133

Al-Noaimat, Y.A., Chougan, M., Al-kheetan, M.J., Al-Mandhari, O., Al-Saidi, W., Al-Maqbali, M., Al-Hosni, H., Ghaffar, S.H., 2023. 3D printing of limestone-calcined clay cement: A review of its potential implementation in the construction industry. Results in Engineering 18, 101115. https://doi.org/10.1016/j.rineng.2023.101115

Alujas, A., Fernández, R., Quintana, R., Scrivener, K.L., Martirena, F., 2015. Pozzolanic reactivity of low grade kaolinitic clays: Influence of calcination temperature and impact of calcination products on OPC hydration. Appl. Clay Sci. 108, 94–101. https://doi.org/10.1016/j.clay.2015.01.028

Andrade Neto, J.S., Rodríguez, E.D., Monteiro, P.J.M., De la Torre, A.G., Kirchheim, A.P., 2022. Hydration of C3S and Al-doped C3S in the presence of gypsum. Cement and Concrete Research 152, 106686. https://doi.org/10.1016/j.cemconres.2021.106686

Antoni, M., Rossen, J., Martirena, F., Scrivener, K., 2012. Cement substitution by a combination of metakaolin and limestone. Cement and Concrete Research 42, 1579–1589. https://doi.org/10.1016/j.cemconres.2012.09.006

Avet, F., Scrivener, K., 2018. Investigation of the calcined kaolinite content on the hydration of Limestone Calcined Clay Cement (LC3). Cem Concr Res 107, 124–135. https://doi.org/10.1016/j.cemconres.2018.02.016

Avet, F., Sofia, L., Scrivener, K., 2019. Concrete performance of limestone calcined clay cement (LC3) compared with conventional cements. Adv. Civ. Eng. Mater. 8. https://doi.org/10.1520/ACEM20190052

Baghban, M.H., Mahjoub, R., 2020. Natural Kenaf Fiber and LC3 Binder for Sustainable Fiber-Reinforced Cementitious Composite: A Review. Applied Sciences 10, 357. https://doi.org/10.3390/app10010357

Bahman-Zadeh, F., Ramezanianpour, A.A., Zolfagharnasab, A., 2022. Effect of carbonation on chloride binding capacity of limestone calcined clay cement (LC3) and binary pastes. Journal of Building Engineering 52, 104447. https://doi.org/10.1016/j.jobe.2022.104447

Bernal, I.M.R., Shirani, S., Cuesta, A., Santacruz, I., Aranda, M.A.G., 2021. Phase and microstructure evolutions in LC3 binders by multi-technique approach including synchrotron microtomography. Construction and Building Materials 300, 124054. https://doi.org/10.1016/j.conbuildmat.2021.124054

Blouch, N., Rashid, K., Ju, M., 2023a. Exploring low-grade clay minerals diving into limestone calcined clay cement (LC3): Characterization − Hydration − Performance. Journal of Cleaner Production 426, 139065. https://doi.org/10.1016/j.jclepro.2023.139065

Blouch, N., Rashid, K., Zafar, I., Ltifi, M., Ju, M., 2023b. Prioritization of low-grade kaolinite and mixed clays for performance evaluation of Limestone Calcined Clay Cement (LC3): Multi-criteria assessment. Applied Clay Science 243, 107080. https://doi.org/10.1016/j.clay.2023.107080

Briki, Y., Avet, F., Zajac, M., Bowen, P., Haha, M.B., Scrivener, K., 2021. Understanding of the factors slowing down metakaolin reaction in limestone calcined clay cement (LC3) at late ages. Cem Concr Res 146. https://doi.org/10.1016/j.cemconres.2021.106477

Cao, Y., Wang, Y., Zhang, Z., Ma, Y., Wang, H., 2023. Thermal stability of limestone calcined clay cement (LC3) at moderate temperatures 100–400 °C. Cement and Concrete Composites 135, 104832. https://doi.org/10.1016/j.cemconcomp.2022.104832

Dhandapani, Y., Sakthivel, T., Santhanam, M., Gettu, R., Pillai, R.G., 2018. Mechanical properties and durability performance of concretes with Limestone Calcined Clay Cement (LC3). Cem Concr Res 107, 136–151. https://doi.org/10.1016/j.cemconres.2018.02.005

Dhandapani, Y., Santhanam, M., 2017. Assessment of pore structure evolution in the limestone calcined clay cementitious system and its implications for performance. Cem Concr Compos 84, 36–47. https://doi.org/10.1016/j.cemconcomp.2017.08.012

Dixit, A., Du, H., Dang, J., Pang, S.D., 2021. Quaternary blended

limestone-calcined clay cement concrete incorporating fly ash. Cement and Concrete Composites 123, 104174. https://doi.org/10.1016/j.cemconcomp.2021.104174
Ez-zaki, H., Marangu, J.M., Bellotto, M., Dalconi, M.C., Artioli, G., Valentini, L., 2021. A Fresh View on Limestone Calcined Clay Cement (LC3) Pastes. Materials 14, 3037. https://doi.org/10.3390/ma14113037
Franco Zunino, F.M., and Karen Scrivener, 2021. Limestone Calcined Clay Cements (LC3). ACI Materials Journal 118. https://doi.org/10.14359/51730422
Guo, M., Gong, G., Yue, Y., Xing, F., Zhou, Y., Hu, B., 2022. Performance evaluation of recycled aggregate concrete incorporating limestone calcined clay cement (LC3). Journal of Cleaner Production 366, 132820. https://doi.org/10.1016/j.jclepro.2022.132820
Hay, R., Celik, K., 2023. Effects of water-to-binder ratios (w/b) and superplasticizer on physicochemical, microstructural, and mechanical evolution of limestone calcined clay cement (LC3). Construction and Building Materials 391, 131529. https://doi.org/10.1016/j.conbuildmat.2023.131529
Hay, R., Li, L., Celik, K., 2022. Shrinkage, hydration, and strength development of limestone calcined clay cement (LC3) with different sulfation levels. Cement and Concrete Composites 127, 104403. https://doi.org/10.1016/j.cemconcomp.2021.104403
He, C., Osbaeck, B., Makovicky, E., 1995. Pozzolanic reactions of six principal clay minerals: Activation, reactivity assessments and technological effects. Cement and Concrete Research 25, 1691–1702. https://doi.org/10.1016/0008-8846(95)00165-4
Hou, M., Li, V.C., 2023. Tailoring crack width control of LC3-based engineered cementitious composites (ECC) via fiber hybridization: From micromechanics design to macro investigation. Materials & Design 235, 112433. https://doi.org/10.1016/j.matdes.2023.112433
Hu, Y., Xiong, L., Yan, Y., Geng, G., 2024. Performance of limestone calcined clay cement (LC3) incorporating low-grade marine clay. Case Stud. Constr. Mater. 20. https://doi.org/10.1016/j.cscm.2024.e03283
Huang, H., Li, X., Avet, F., Hanpongpun, W., Scrivener, K., 2021. Strength-promoting mechanism of alkanolamines on limestone-calcined clay cement and the role of sulfate. Cement and Concrete Research 147, 106527. https://doi.org/10.1016/j.cemconres.2021.106527
Huang, X., Jiao, Z., Xing, F., Sui, L., Hu, B., Zhou, Y., 2024. Performance assessment of LC3 concrete structures considering life-cycle cost and environmental impacts. Journal of Cleaner Production 436, 140380. https://doi.org/10.1016/j.jclepro.2023.140380
Huang, Z., Huang, Y., Liao, W., Han, N., Zhou, Y., Xing, F., Sui, T., Wang, B., Ma, H., 2020. Development of limestone calcined clay cement concrete in South China and its bond behavior with steel reinforcement. J. Zhejiang Univ. Sci. A 21, 892–907. https://doi.org/10.1631/jzus.A2000163
Huang, Z., Liang, T., Chen, L., 2023. Experimental studies on durability performances of ultra-lightweight low-carbon LC3 cement composites against chloride ingression and carbonation. Construction and Building Materials 395, 132340. https://doi.org/10.1016/j.conbuildmat.2023.132340
Ibrahim, K.A., Van Zijl, G.P.A.G., Babafemi, A.J., 2023. Influence of limestone calcined clay cement on properties of 3D printed concrete for sustainable construction. Journal of Building Engineering 69, 106186. https://doi.org/10.1016/j.jobe.2023.106186
Ijaz, N., Ye, W., Rehman, Z.U., Ijaz, Z., 2022. Novel application of low carbon limestone calcined clay cement (LC3) in expansive soil stabilization: An eco-efficient approach. Journal of Cleaner Production 371, 133492. https://doi.org/10.1016/j.jclepro.2022.133492
Kafodya, I., Basuroy, D., Marangu, J.M., Kululanga, G., Maddalena, R., Novelli, V.I., 2023. Mechanical Performance and Physico-Chemical Properties of Limestone Calcined Clay Cement (LC3) in Malawi. Buildings 13, 740. https://doi.org/10.3390/buildings13030740
Kanagaraj, B., Anand, N., Johnson Alengaram, U., Samuvel Raj, R., Karthick, S., 2024. Limestone calcined clay cement (LC3): A sustainable solution for mitigating environmental impact in the construction sector. Resources, Conservation & Recycling Advances 21, 200197. https://doi.org/10.1016/j.rcradv.2023.200197
Kanagaraj, B., Anand, N., Samuvel Raj, R., Lubloy, E., 2023. Techno-socio-economic aspects of Portland cement, Geopolymer, and Limestone Calcined Clay Cement (LC3) composite systems: A-State-of-Art-Review. Construction and Building Materials 398, 132484. https://doi.org/10.1016/j.conbuildmat.2023.132484
Kim, G., Cho, S., Moon, J., Suh, H., Her, S., Sim, S., Bae, S., 2024. Investigation of the hydrate formation and mechanical performance of limestone calcined clay cement paste incorporating nano-CaCO3 and nano-SiO2 as partial limestone substitutes. Construction and Building Materials 418, 135335. https://doi.org/10.1016/j.conbuildmat.2024.135335
Li, H., Yang, J., Wang, L., Li, L., Xia, Y., Köberle, T., Dong, W., Zhang, N., Yang, B., Mechtcherine, V., 2023. Multiscale assessment of performance of limestone calcined clay cement (LC3) reinforced with virgin and recycled carbon fibers. Construction and Building Materials 406, 133228. https://doi.org/10.1016/j.conbuildmat.2023.133228
Li, Q., 2019. THE MICROSTRUCTURE AND MECHANICAL PROPERTIES OF CEMENTITIOUS MATERIALS COMPRISED OF LIMESTONE, CALCINED CLAY AND CLINKER. Ceramics - Silikaty 356–364. https://doi.org/10.13168/cs.2019.0031
Li, X., Dengler, J., Hesse, C., 2023. Reducing clinker factor in limestone calcined clay-slag cement using C-S-H seeding – A way towards sustainable binder. Cement and Concrete Research 168, 107151. https://doi.org/10.1016/j.cemconres.2023.107151
Lin, R.-S., Han, Y., Wang, X.-Y., 2021. Macro–meso–micro experimental studies of calcined clay limestone cement (LC3) paste subjected to elevated temperature. Cement and Concrete Composites 116, 103871. https://doi.org/10.1016/j.cemconcomp.2020.103871
Lin, R.-S., Oh, S., Du, W., Wang, X.-Y., 2022. Strengthening the performance of limestone-calcined clay cement (LC3) using nano silica. Construction and Building Materials 340, 127723. https://doi.org/10.1016/j.conbuildmat.2022.127723
Liu, J., Zhang, W., Li, Z., Jin, H., Liu, W., Tang, L., 2021. Investigation of using limestone calcined clay cement (LC3) in engineered cementitious composites: The effect of propylene fibers and the curing system. Journal of Materials Research and Technology 15, 2117–2144. https://doi.org/10.1016/j.jmrt.2021.09.023
Liu, J., Zhang, W., Li, Z., Jin, H., Tang, L., 2022. Mechanics, hydration phase and pore development of embodied energy and carbon composites based on ultrahigh-volume low-carbon cement with limestone calcined clay. Case Studies in Construction Materials 17, e01299. https://doi.org/10.1016/j.cscm.2022.e01299
Long, W.-J., Lin, C., Tao, J.-L., Ye, T.-H., Fang, Y., 2021. Printability and particle packing of 3D-printable limestone calcined clay cement composites. Construction and Building Materials 282, 122647. https://doi.org/10.1016/j.conbuildmat.2021.122647
Long, W.-J., Wu, Z., Khayat, K.H., Wei, J., Dong, B., Xing, F., Zhang, J., 2022. Design, dynamic performance and ecological efficiency of fiber-reinforced mortars with different binder systems: Ordinary Portland cement, limestone calcined clay cement and alkali-activated slag. Journal of Cleaner Production 337, 130478. https://doi.org/10.1016/j.jclepro.2022.130478
Luan, C., 2023. Synergic effect of triethanolamine and C-S-H seeding on early hydration of the limestone calcined clay cement in UHPC. Construction and Building Materials 400. https://doi.org/https://doi.org/10.1016/j.conbuildmat.2023.132675
Maraghechi, H., Avet, F., Wong, H., Kamyab, H., Scrivener, K., 2018. Performance of Limestone Calcined Clay Cement (LC3) with various kaolinite contents with respect to chloride transport. Mater Struct 51. https://doi.org/10.1617/s11527-018-1255-3
Marangu, J.M., 2020. Physico-chemical properties of Kenyan made calcined Clay -Limestone cement (LC3). Case Studies in Construction Materials 12, e00333. https://doi.org/10.1016/j.cscm.2020.e00333
Martinez, D.M., Horvath, A., Monteiro, P.J.M., 2023. Comparative environmental assessment of limestone calcined clay cements and typical blended cements. Environ. Res. Commun. 5, 055002. https://doi.org/10.1088/2515-7620/acccd8
Mishra, G., Emmanuel, A.C., Bishnoi, S., 2019. Influence of temperature on hydration and microstructure properties of limestone-calcined clay blended cement. Mater Struct 52. https://doi.org/10.1617/s11527-019-1390-5
Musbau, K.D., Kolawole, J.T., Babafemi, A.J., Olalusi, O.B., 2021. Comparative performance of limestone calcined clay and limestone calcined laterite blended cement concrete. Clean. Eng. Technol. 4. https://doi.org/10.1016/j.clet.2021.100264
Nair, N., Mohammed Haneefa, K., Santhanam, M., Gettu, R., 2020. A study on fresh properties of limestone calcined clay blended cementitious systems. Constr Build Mater 254. https://doi.

org/10.1016/j.conbuildmat.2020.119326
Nguyen, Q.D., Afroz, S., Castel, A., 2020. Influence of clay calcination method on the mechanical properties and chloride diffusion resistance of limestone calcined clay cement (LC3) concrete. J. Mar. Sci. Eng. 8. https://doi.org/10.3390/JMSE8050301
Nguyen, Q.D., Afroz, S., Zhang, Y., Kim, T., Li, W., Castel, A., 2022. Autogenous and total shrinkage of limestone calcined clay cement (LC3) concretes. Construction and Building Materials 314, 125720. https://doi.org/10.1016/j.conbuildmat.2021.125720
Page, M.J., McKenzie, J.E., Bossuyt, P.M., Boutron, I., Hoffmann, T.C., Mulrow, C.D., Shamseer, L., Tetzlaff, J.M., Akl, E.A., Brennan, S.E., Chou, R., Glanville, J., Grimshaw, J.M., Hróbjartsson, A., Lalu, M.M., Li, T., Loder, E.W., Mayo-Wilson, E., McDonald, S., McGuinness, L.A., Stewart, L.A., Thomas, J., Tricco, A.C., Welch, V.A., Whiting, P., Moher, D., 2021. The PRISMA 2020 statement: an updated guideline for reporting systematic reviews. BMJ n71. https://doi.org/10.1136/bmj.n71
Parashar, A., Bishnoi, S., 2021. Hydration behaviour of limestone-calcined clay and limestone-slag blends in ternary cement. RILEM Tech Lett 6, 17–24. https://doi.org/10.21809/rilemtechlett.2021.134
Ram, K., Flegar, M., Serdar, M., Scrivener, K., 2022. Influence of Low- to Medium-Kaolinite Clay on the Durability of Limestone Calcined Clay Cement (LC3) Concrete. Materials 16, 374. https://doi.org/10.3390/ma16010374
Scrivener, K., Avet, F., Maraghechi, H., Zunino, F., Ston, J., Hanpongpun, W., Favier, A., 2018a. Impacting factors and properties of limestone calcined clay cements (LC3). Green Mater. 7, 3–14. https://doi.org/10.1680/jgrma.18.00029
Scrivener, K., Martirena, F., Bishnoi, S., Maity, S., 2018b. Calcined clay limestone cements (LC3). Cem Concr Res 114, 49–56. https://doi.org/10.1016/j.cemconres.2017.08.017
Sharma, M., Bishnoi, S., Martirena, F., Scrivener, K., 2021. Limestone calcined clay cement and concrete: A state-of-the-art review. Cem Concr Res 149. https://doi.org/10.1016/j.cemconres.2021.106564
Shoukry, H., Perumal, P., Abadel, A., Alghamdi, H., Alamri, M., Abdel-Gawwad, H.A., 2022. Performance of limestone-calcined clay cement mortar incorporating high volume ferrochrome waste slag aggregate. Construction and Building Materials 350, 128928. https://doi.org/10.1016/j.conbuildmat.2022.128928
Silva, M.R.C.D., Andrade Neto, J.D.S., Walkley, B., Kirchheim, A.P., 2024. Exploring sulfate optimization techniques in Limestone Calcined Clay Cements (LC3): limitations and insights. Cement and Concrete Research 175, 107375. https://doi.org/10.1016/j.cemconres.2023.107375
Sui, H., Hou, P., Liu, Y., Sagoe-Crentsil, K., Basquiroto de Souza, F., Duan, W., 2023. Limestone calcined clay cement: mechanical properties, crystallography, and microstructure development. Journal of Sustainable Cement-Based Materials 12, 427–440. https://doi.org/10.1080/21650373.2022.2074911
Tino Balestra, C.E., Garcez, L.R., Couto Da Silva, L., Veit, M.T., Jubanski, E., Nakano, A.Y., Pietrobelli, M.H., Schneider, R., Ramirez Gil, M.A., 2023. Contribution to low-carbon cement studies: Effects of silica fume, fly ash, sugarcane bagasse ash and acai stone ash incorporation in quaternary blended limestone-calcined clay cement concretes. Environmental Development 45, 100792. https://doi.org/10.1016/j.envdev.2022.100792
Wang, J., Huang, Y., 2023. Mechanical properties and hydration of ultra-high-performance seawater sea-sand concrete (UHPSSC) with limestone calcined clay cement (LC3). Construction and Building Materials 376, 130950. https://doi.org/10.1016/j.conbuildmat.2023.130950
Wang, Y., Chen, M., Zhang, T., Zhang, M., 2024. Hardening properties and microstructure of 3D printed engineered cementitious composites based on limestone calcined clay cement. Cement and Concrete Composites 152, 105641. https://doi.org/10.1016/j.cemconcomp.2024.105641
Wang, Y.-S., Meng, L.-Y., Chen, L., Wang, X.-Y., 2025. An innovative strategy for CO2 conversion and utilization: Semi-wet carbonation pretreatment of wollastonite to prepare carbon-fixing products and produce LC3. Cement and Concrete Composites 160, 106050. https://doi.org/10.1016/j.cemconcomp.2025.106050
Wang, Y.-S., Wang, X.-Y., 2023. Multi-characterizations of the hydration, microstructure, and mechanical properties of a biochar–limestone calcined clay cement (LC3) mixture. Journal of Materials Research and Technology 24, 3691–3703. https://doi.org/10.1016/j.jmrt.2023.04.033
Xuan, M., Bae, S.C., Kwon, S.-J., Wang, X.-Y., 2022. Sustainability enhancement of calcined clay and limestone powder hybrid ultra-high-performance concrete using belite-rich Portland cement. Construction and Building Materials 351, 128932. https://doi.org/10.1016/j.conbuildmat.2022.128932
Yu, Jing, Mishra, D.K., Hu, C., Leung, C.K.Y., Shah, S.P., 2021. Mechanical, environmental and economic performance of sustainable Grade 45 concrete with ultrahigh-volume Limestone-Calcined Clay (LCC). Resources, Conservation and Recycling 175, 105846. https://doi.org/10.1016/j.resconrec.2021.105846
Yu, J., Wu, H.-L., Leung, C.K.Y., 2020. Feasibility of using ultrahigh-volume limestone-calcined clay blend to develop sustainable medium-strength Engineered Cementitious Composites (ECC). Journal of Cleaner Production 262, 121343. https://doi.org/10.1016/j.jclepro.2020.121343
Yu, J., Wu, H.-L., Mishra, D.K., Li, G., Leung, C.K., 2021. Compressive strength and environmental impact of sustainable blended cement with high-dosage Limestone and Calcined Clay (LC2). J. Clean. Prod. 278. https://doi.org/10.1016/j.jclepro.2020.123616
Yu, K., Liu, C., Li, L., Tian, W., Yang, Y., Liu, Y., 2024. Carbon-negative heat-stored limestone calcined clay cement mortar containing form-stable phase change materials. Journal of Cleaner Production 437, 140703. https://doi.org/10.1016/j.jclepro.2024.140703
Yu, T., Zhang, B., Yuan, P., Guo, H., Liu, D., Chen, J., Liu, H., Setti Belaroui, L., 2023. Optimization of mechanical performance of limestone calcined clay cement: Effects of calcination temperature of nanosized tubular halloysite, gypsum content, and water/binder ratio. Construction and Building Materials 389, 131709. https://doi.org/10.1016/j.conbuildmat.2023.131709
Zhang, D., Jaworska, B., Zhu, H., Dahlquist, K., Li, V.C., 2020. Engineered Cementitious Composites (ECC) with limestone calcined clay cement (LC3). Cem Concr Compos 114. https://doi.org/10.1016/j.cemconcomp.2020.103766
Zhao, Y., Zhang, Y., 2023. A Review on Hydration Process and Setting Time of Limestone Calcined Clay Cement (LC3). Solids 4, 24–38. https://doi.org/10.3390/solids4010003
Zhou, Y., Gong, G., Xi, B., Guo, M., Xing, F., Chen, C., 2022. Sustainable lightweight engineered cementitious composites using limestone calcined clay cement (LC3). Composites Part B: Engineering 243, 110183. https://doi.org/10.1016/j.compositesb.2022.110183
Zhu, H., Yu, K., Li, V.C., 2021. Sprayable engineered cementitious composites (ECC) using calcined clay limestone cement (LC3) and PP fiber. Cement and Concrete Composites 115, 103868. https://doi.org/10.1016/j.cemconcomp.2020.103868
Zolfagharnasab, A., Ramezanianpour, A.A., Bahman-Zadeh, F., 2021. Investigating the potential of low-grade calcined clays to produce durable LC3 binders against chloride ions attack. Construction and Building Materials 303, 124541. https://doi.org/10.1016/j.conbuildmat.2021.124541
Zunino, F., Scrivener, K., 2021a. The reaction between metakaolin and limestone and its effect in porosity refinement and mechanical properties. Cem Concr Res 140. https://doi.org/10.1016/j.cemconres.2020.106307
Zunino, F., Scrivener, K., 2021b. Assessing the effect of alkanolamine grinding aids in limestone calcined clay cements hydration. Constr Build Mater 266. https://doi.org/10.1016/j.conbuildmat.2020.121293

**Sara Baradarandilmaghani,** PhD student at Budapest University of Technology and Economics. Doctoral research focuses on LC3 concrete. Master's degree thesis completed in geopolymer concrete/mortar and utilizing Machine-Learning algorithms for prediction, at University of Science Malaysia. Research interest: concrete technology, innovation and integration of computational technologies within civil engineering. 3D concrete printing. Member of the Hungarian ***fib*** Group.

**Sándor Sólyom,** Associate Professor at the Department of Construction Materials and Technologies, Faculty of Civil Engineering, Budapest University of Technology and Economics. Research interest: FRP (Fibre Reinforced Polymer), FRC (Fibre Reinforced Concrete), bond of reinforcement to concrete, 3D concrete printing, concrete technology and durability. He is deputy president of Hungarian Group of fib, secretary of *fib* Com 9 Dissemination of knowledge.

# PERFORMANCE AND REINFORCEMENT DETAILING OF COUPLING BEAMS UNDER SEISMIC LOADS - A COMPREHENSIVE REVIEW



https://doi.org/10.32970/CS.2026.1.7

Mariam Ibraheem M. Hussein - Mohammed M. Rasheed - Asma Mahdi Ali

*A coupled system, comprising coupling beams and a shear wall, is highly effective in resisting lateral forces in tall structures. It offers advantages such as enhanced stiffness, flexibility, energy dissipation, and is essential for transferring shear forces between walls. Strength and stiffness of coupling beams decline significantly under high earthquake stress, necessitating careful material and reinforcement considerations due to their structural importance. Research on the coupling system shows it can be reinforced either diagonally or conventionally based on the aspect ratio, yet notable gaps exist due to limited global studies and models examined. This study reviews previous research on coupling beams, addressing the coupled system's mechanism and coupling degree It discusses the importance of selecting appropriate reinforcement and confinement methods for coupled beams, highlights the effect of shear wall deflection on their performance, and provides key equations for assessing shear resistance, noting sudden shear failure as the main failure mode.*

**Keywords:** coupling beam, shear wall, diagonal reinforcement, conventional reinforcement, confinement

## 1. INTRODUCTION

In recent years, due to expanding populations and a notable increase in the need for urban space optimization, particularly in places at risk for earthquakes and with developments in material technology, structural design, and analysis have made it feasible to create high-rise structures that can resist severe loads such as strong winds and seismic motion (Freddia et al., 2021). Coupled shear walls are among the extensively utilized lateral force-counteracting solutions for mid and high structures (Paulay, 1971; Subedi, 1991; Cheng et al., 2014). This system is essentially made up of two structural walls or more joined by relatively deep beams with short span, also known as coupling beams. It is well known that coupling beams may serve as effective energy dissipation sources and enhance the lateral rigidity of a conventional coupled system. For understanding their behavior, researchers have been examining the reaction of coupling beams with different reinforcement patterns. Despite this, there are many questions about the internal mechanics and force paths produced by seismic pressure. Consequently, stronger reinforcement and detailed specifications are often needed for coupling beams. This frequently results in reinforcement congestion, which makes reinforcement design more challenging (Lequesne et al., 2013; Son et al., 2014; Ye, 2020). As buildings get taller and the requirement to manage construction costs increases, new technical solutions are needed as the existing ones become outdated.

There are many kinds of coupling beams, such as those with embedded steel plates. Although steel-embedded beams are powerful, their strength comes with a significant cost, and construction may become more challenging (Kuang & Baczkowski, 2006). In multistory building designs, structural walls have been used to sustain side loads like wind or repeated pressures. Coupled shear walls, which are made up of two vertical components joined by short and deep beams, are one example of such system. The lateral resistance capability of the building is increased by these connecting beams. The RC coupling beams are subject to shear stresses when exposed to extreme ground motion because they disperse seismic energy through significant inelastic deformation. The stiffness of the frame, which is made up of the wall piers and connection beams, differs significantly from the moment capacity of the independent wall piers. The frame rigidity in the coupled system is dependent on the axial stiffness of the piers of the coupled walls. In a coupled shear wall construction, the frame action of the connection beams, that is, the axial couple forces [T and C] across the piers of shear walls, results from the accumulated shear at the ends of connection beams over the height of the structure, which is usually more rigid than the flexural response of the individual wall piers (Harries, 2001; Shahrooz et al., 2018). However, traditional RC coupling beams are subjected to severe damage during earthquakes and may need to be replaced or repaired after the fact, which can be expensive.

Researchers have offered several alternative methods to address this problem, including steel corrugated plate coupling beams, replaceable steel connection beams, and self-centering steel coupling beams. Furthermore, the "fuse" idea has been adopted, whereby the middle section of the connection beam is intended to concentrate damage and release energy, making replacement simple in the event of a seismic action. These technologies aim to improve coupling beam performance while lowering the costs and problems associated with post-event maintenance or replacement (Sakr et al., 2023). Despite these solutions, concrete-coupled beams remain the most common; also, many designers are unaware of the importance of this structural part and how it behaves under load. Therefore, this paper presents an inclusive review of the behavior and conduct of connection beams when the reinforcement varied.

## 2. COUPLED SYSTEM BEHAVIOR

Shear walls, which can be either plain or reinforced concrete, help to stabilize a building laterally (European Committee for Standardization, 2004). Structural wall systems resemble wide beams aligned vertically and respond to lateral loads like a thin cantilever beam (Ocfaoa, 1987). At the base, shear walls are typically highly rigid, but as they rise in height, they progressively become more flexible (Nawy, 2008). Beams that span a doorway or other similar openings are sometimes used to link two shear walls. In both low-rise and high-rise construction, structural wall systems are commonly used to provide lateral drift (Ocfaoa, 1987).

Coupled wall constructions are excellent lateral load-resisting systems that distribute inelastic distortion between the connection beams and the shear wall piers in the vertical direction and the plane, in addition to lowering the disfigurement demands on the structure. When exposed to significant earthquake stresses, coupling beams may experience rapid deterioration in both strength and stiffness (Eljadei & Harries, 2014). The walls work as separate cantilevers when the connection beam stiffness is close to zero or as a single solid cantilever when the coupling beam stiffness is large (Wight & MacGregor, 2012). The coupled beams transfer shear forces between the coupled walls as shown in *Fig. 1*. As mentioned earlier, coupling beams between shear walls make the structure work as a cantilever, but there is a difference between shear walls and cantilever walls (James et al., 2014).

The base shear demand for the shear wall model is reduced with a little increase in the fundamental period. In contrast, the base shear requirement for the cantilever wall model rises with a little increase in the fundamental period. Furthermore, the shear wall models are less sensitive to changes in damping models than the cantilever wall models. Additionally, a change in damping coefficients causes a significant variation in base shear forces in the cantilever wall model but a slight difference in base shear forces in the shear wall model. Lastly, when using a constant damping model, the lack of mass in the cantilever model leads to a significantly lower base shear demand, but the shear wall models did not exhibit this effect (Harris & Wijanto, 2000; Metwally, 2019).

**Fig. 1:** Overturning coupled shear wall moment resistance (Wight & MacGregor, 2012)

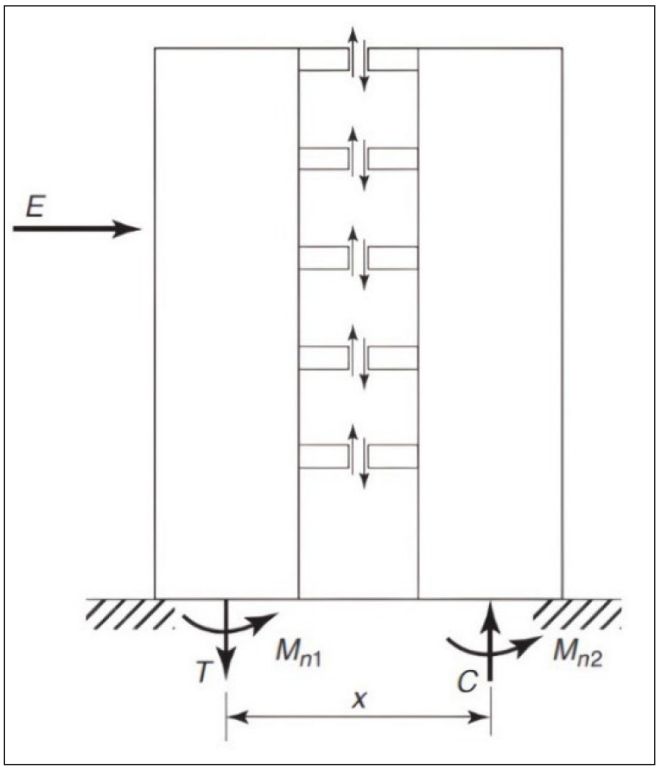


## 3. DEGREE OF COUPLING

In contrast to the displacement distribution, which is frequently governed by the basic lateral mode of vibration of the structures, the distribution of seismic force on a coupled system is usually dominated by higher lateral modes of vibration. A further dynamic impact occurs when the wall response changes from elastic to inelastic behavior (Rivard et al., 2019). In tall reinforced concrete buildings, coupled system constructions, as seen in *Fig. 2*, can provide an effective side load resistance mechanism toward the effects of wind and earthquakes. The axial bending moment T*l, which is the horizontal force T caused in the walls by the shear forces in the connection beams, multiplied by the distance between the neutral axes, and the primary moments Mn1 and Mn2 taken by the separate shear walls make up the total overturning moment of such structures under horizontal loading. One factor may be used to summarize the link between these two kinds of bending moments. The moment at the base of the building, given as a percentage of the whole overturning moment, defines the degree of connection (DoC) of the coupled system. However, the relationship between the average shear force, $Vb_{avg.}$, and the maximum shear force, $Vb_{max}$, in the essential connection beam and its position along the height of the building is known as the peak shear demand, or PSD. The degree of connection (DoC) and the peak shear demand (PSD) are two crucial factors in the blueprint of coupled systems (Hoenderkamp, 2012) Equations (1) and (2) can calculate these factors.

$$DOC = \frac{T.l}{M_{n1}+M_{n2}+T.l} \quad (1)$$

$$PSD = \frac{Vb_{max.}}{Vb_{avg.}} \quad (2)$$

where T is the total shear forces at the end of connection beams and l is the distance between the connection walls C/C. The degree of connection in typical coupled systems ranges from 0.3 to 0.5 (Wight & MacGregor, 2012).

**Fig. 2:** Lateral load resistance mechanism in coupled system (Hoenderkamp, 2012)

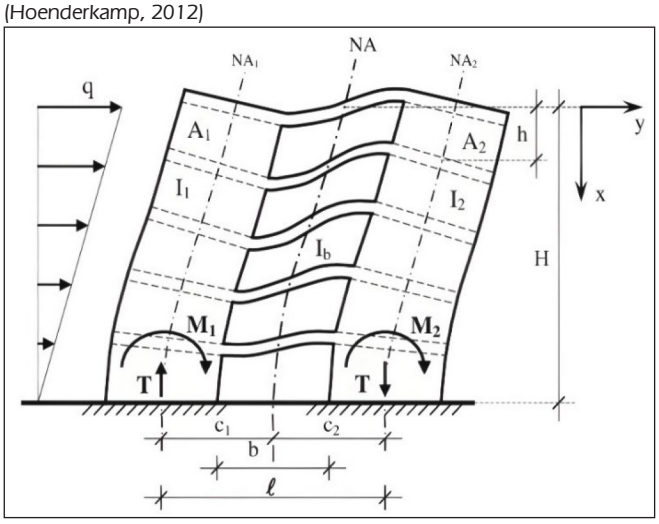

The most important variable influencing how coupled systems behave seismically is the degree of connection. If the degree of connection is too low, a connection wall system functions as a coupled wall; if it is too high, it functions as a pierced wall (Adhikari, 2015). For low- to mid-rise coupled walls, a degree of coupling of 0.25 to 0.4 is appropriate in order to optimize the energy dissipation capabilities. For high-rise linked wall systems, on the other hand, a degree of coupling of 0.5 to 0.6 is found to be ideal, providing both improved lateral load resistance and efficient energy dissipation during earthquakes (Adhikari, 2015). Seismic amplification of seismic shear forces diminishes with an increasing degree of coupling (Rivard et al., 2019).

## 4. REINFORCEMENT OF COUPLING BEAM

There are two methods of reinforcing connection beams: conventional and diagonal. During a large seismic action, connection beams can be subjected to large repeated reversals of shear distortion, which might quickly reduce their stiffness and shear strength. The inclined reinforcement shape depicted in *Fig. 3* transmits repeated load and enhanced member stiffness considerably better than conventional reinforcement composed of vertical stirrups and top and bottom longitudinal steel, according to tests of short coupling beams reported by Park and Paulay (1975). This diagonal steel creates forces Tu and Cu by functioning as a truss and transmitting a moment and shear, where:

$$T_u = C_u = \emptyset A_s f_y \tag{3}$$

$$V_u = 2T_u \sin\alpha = 2\emptyset A_s f_y \sin\alpha \tag{4}$$

$$M_u = (\emptyset A_s f_y \cos\propto)(h - 2d') \tag{5}$$

Depending on the ACI 318-19 Code Section 21.9.7.2, connection beams with aspect ratio less than 2 and with a design shear strength more than ($V_{limit}$) must utilize diagonal reinforcement like that shown in *Fig. 3*. While, coupling beams with aspect ratio more than 4 must be constructed as a bending element of an exceptional moment frame in accordance with ACI Code Section 21.9.7.1.

$$V_{limit} = 4\lambda\sqrt{f_c'}A_{cw} \tag{6}$$

where $A_{cw}$ is the coupling beam area b×h.

ACI Code Section 21.9.7.3 allows a designer to choose between conventional reinforcement and diagonal reinforcement, which are controlled by ACI Code Sections 21.5.2 through 21.5.4, as shown in *Fig. 3*.

For connection beams that are not covered by ACI Code Sections, the author supposed that a partnership of inclined and traditional reinforcement would be more useful than using only one or the other kind of reinforcement for connection beams with aspect ratios between 2 and 4, even though the ACI Code does not address a partnership of these draw up for such connection beams (Wight & MacGregor, 2012).

The construction of conventional connection beams is comparatively simpler than that of diagonally connection beams. Nevertheless, their capacity to dissipate energy is reduced. In conventional coupling beams, both top and

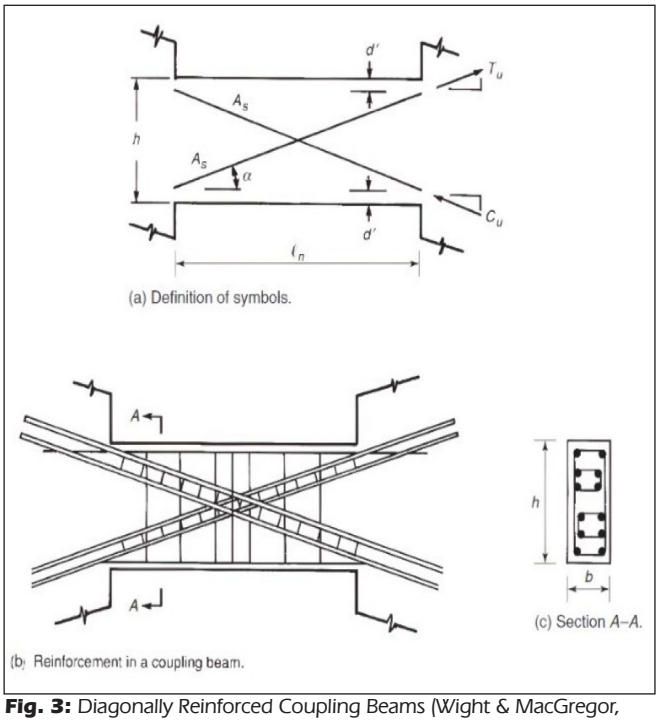


**Fig. 3:** Diagonally Reinforced Coupling Beams (Wight & MacGregor, 2012)

bottom bars may at the same time undergo tension due to inclined cracking; this results in the tendency for the beam to stretch. When the damage is minor to moderate, vertical cracks appear at the ends of the member. When combined with the observed beam elongation, these cracks constitute

**Fig. 4.** Conventional Reinforcing Coupling Beam. a) Reinforcing Layout (Boivin, 2006), b) General Crack Pattern (Harries, 2001)

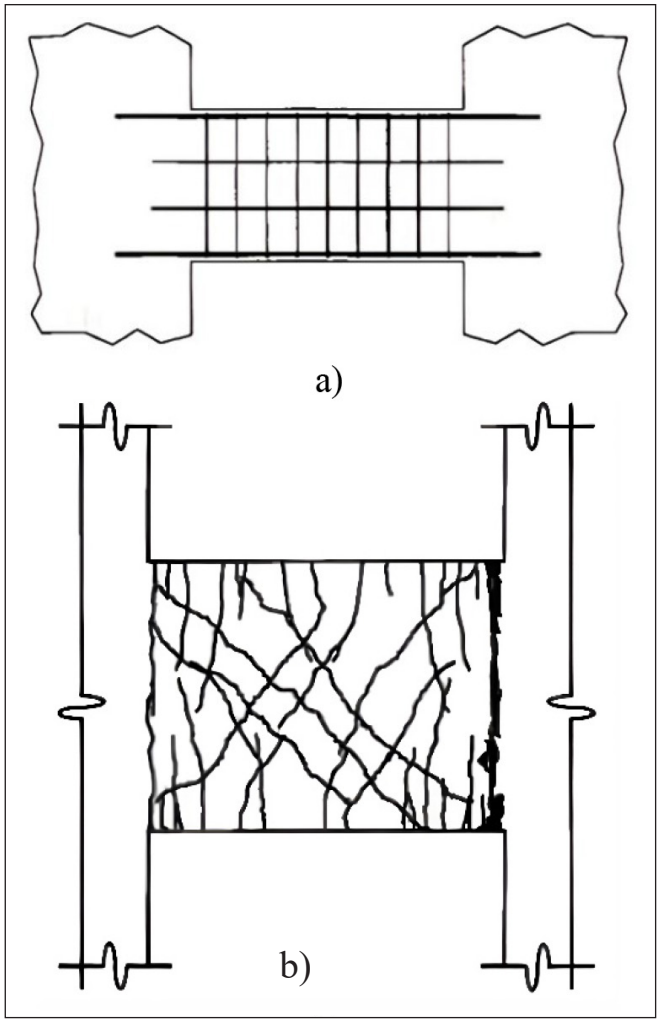

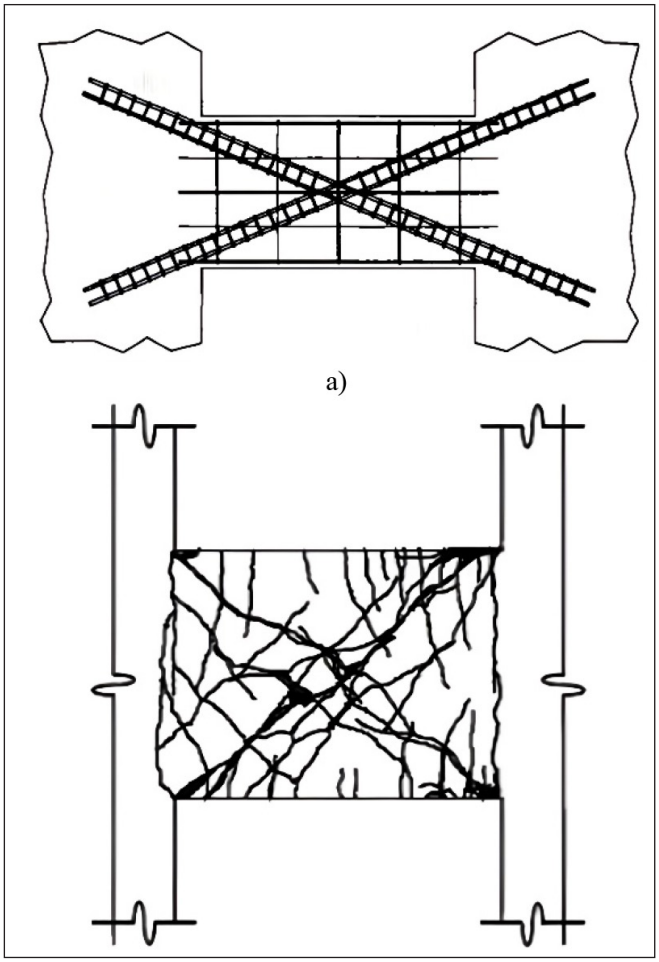


**Fig. 5:** *Diagonal Reinforcing Coupling Beam. a) Reinforcing Layout (Boivin, 2006), b) General Crack Pattern (Harries, 2001)*

a potential sliding plane (Harries, 2001). However, concrete deterioration along these vertical cracks at high damage levels results in a sliding collapse. The energy dissipation resistance of the beam is limited by this failure, which can happen at very low levels of ductility(FEMA, 1998). The crack pattern for conventional and diagonal connection beams are shown in *Fig. 4-5*, respectively.

When compared to conventional beams, deep coupling beams function differently. Following cracking, they behave more such as a truss, with a rotating inclined concrete strut that causes horizontal elongation. At the beam-wall joints, shear-sliding failure may result from increased shear reinforcement, even while shear-tension failure may be suppressed. Similarly, restricting axial elongation can raise the shear capacity but eventually results in a more brittle failure (Zhao et al., 2004).

## 5. CONFINEMENT IN COUPLING BEAMS

Section 21.9.7.4 in ACI Code permits engineers to confine diagonal reinforcement using one of two methods. The diagonals work alternately in tension and compression when a connection wall system responds to seismic motion caused by earthquakes. Section 21.9.7.4 (c) provides specific guidelines for placing shear steel bars along the diagonal bars as shown in *Fig. 3*. Similar to what is needed for columns, the purpose of this transverse reinforcement is to contain a set of diagonal bars (at least four diagonal bars) (Wight & MacGregor, 2012). Section 21.9.7.4 (d) of the ACI Code provides an alternative method for confining the diagonal

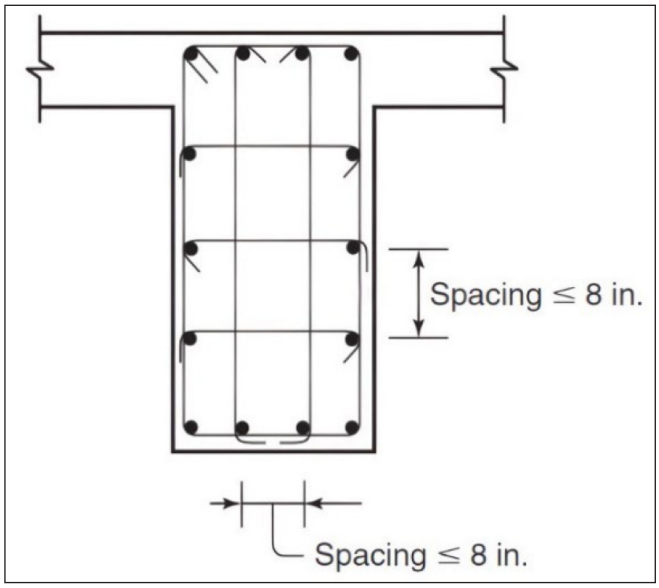


**Fig. 6:** *An Alternative Method for Reinforcing Confinement in connection Beams (Wight & MacGregor, 2012)*

bars by using shear steel bars to contain the whole connection beam section, as shown in *Fig. 6*. It is necessary to supply this transverse reinforcement in both vertical and horizontal orientations. Because of the construction challenges of putting confinement bars immediately around each group of the inclined bars, several structural engineers have expressed a behavior for this second solution (Wight & MacGregor, 2012). Excellent ductility and energy dissipation are provided by coupling beams when they are diagonally strengthened and include appropriate confinement to offer sufficient stability (Hindi & Hassan, 2004).

## 6. ADVANTAGES OF COUPLED SYSTEM

The coupled system has many advantages such as:

1. Increase the lateral rigidity (Daniel & Joel, 2022).
2. Facilitate shear force transfer (Daniel & Joel, 2022).
3. Enhance ductility to absorb and dissipate the energy induced by side displacement (Daniel & Joel, 2022).
4. Produce a structural framework that is feasible from an architectural standpoint (Thambi & Prabha, 2017).
5. The coupling effect provides increased strength (Thambi & Prabha, 2017).
6. Since the axial loads help to resist a portion of the base-overturning moment, foundation restraint is easier to apply than for comparable isolated walls (Thambi & Prabha, 2017).
7. Connection beams serve as an effective means of dissipating energy along the structure height, reducing concentration at the base while maintaining the structural integrity of the shear walls (Thambi & Prabha, 2017).
8. Specifying a reasonable degree of deformation in the connection beams might help balance the expenses of building and maintenance after seismic (Thambi & Prabha, 2017).

## 7. DEFLECTIONS IMPACT OF COUPLED WALLS ON THE FORCES IN THE CONNECTION BEAM

Shear wall structures should meet the requirements of a

"strong coupling wall with a weak coupling beam," depending on the ductility design assumptions. In an earthquake, a structure with this arrangement will be sufficiently stiff to keep the shear wall from collapsing first (Zhang et al., 2017). As shown in *Fig. 7*, when the linked shear wall deformities, the axes of each coupled wall components at A and A' rotate at an angle and deflect laterally. This leads to make deformations in the connection beams linking the two coupled walls. The angle that the coupling beam must go through at its wall connection is reduced when the beam-to-wall connection breaks locally. The assumed connection point is often moved from the wall face by roughly $h_b / 2$, where $h_b$ is the connection beam height, to reflect the impact of these localized deformations and decreased the connection beam stiffness (MacLeod, 1971). Consequently, assuming the two walls are linked by connection beams spanning from B, the downward deformation (longitudinal displacement) of point B:

$$\Delta_B = \left(\frac{b_w}{2} - \frac{h_w}{2}\right) \tan \propto \tag{7}$$

The lateral displacement in walls causes shears and moments in the connection beams, as shown in *Fig. 7*. A schematic of a free body that crosses the connection beams between the internal side of the two coupled walls shows that each coupling beam has shear forces $V_{bi}$. Additionally, lateral forces are applied to the connection beams. To achieve vertical force balance, the axial forces in the walls must be subjected to an axial tension $T_\circ$ at the centroid of wall 1 from the bottom and a lateral compression $C_\circ$ at the center of wall 2 from the bottom so that this factor can be calculated by (Eljadei & Harries, 2014):

$$T_\circ = C_\circ = \sum_{i=1}^{n} V_{bi} \tag{8}$$

The following formula is used to calculate the whole moment at the base of the connected system. The distance between both forces $T_\circ$ and $C_\circ$ is denoted by (Eljadei & Harries, 2014).

$$M_\circ = M_1 + M_2 + T_\circ . l \tag{9}$$

The upright axis indicates the slenderness ratio of the connection beam, or $h_b/l_b$, where $h_b$ and $l_b$ stand for the height and span of the coupling beam, respectively. In this case, the beam slenderness serves as an evaluate of the stiffness of the connection beam. The wall moments are divided proportionately to the ratio of the wall stiffnesses since a coupling beam with $h_b/l_b$ equal to zero has no flexural stiffness, as stated as follows (Eljadei & Harries, 2014):

$$M_1 = M_\circ \frac{l_1}{l_1 + l_2} \tag{10}$$

$$M_2 = M_\circ \frac{l_2}{l_1 + l_2} \tag{11}$$

The shears in the coupling beams increase with their flexural stiffness. This leads to an asymptotic growth in the proportion of the overturning moment resistedby $T_\circ$.l (Wight & MacGregor, 2012). One of the primary impacts of the coupling beam is the reduction of the moments M1 and M2 at the bases of each connection walls. This makes it easier for wall reactions to be transmitted to the foundation. Furthermore, the lateral deflections are reduced by the connecting beams (Wight & MacGregor, 2012). Nonetheless,

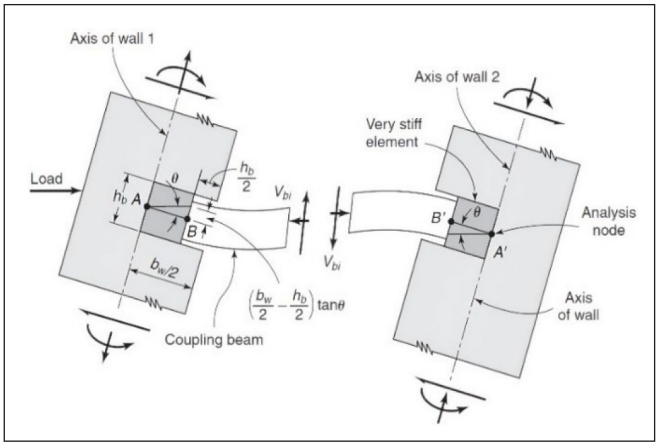


**Fig. 7:** *Deflections impact of coupled walls on the forces in the connection beam (MacLeod, 1971)*

the vertical components should yield after the connection beams (Nouri et al., 2016).

# 8. SHEAR CAPACITY OF COUPLING BEAMS

The NZS code (2006) states that the deflection at one end of a diagonal coupling beam from a line drawn normally to the deflected shape of the coupled wall at the other end of the connection beam should be divided by the clear length of the connecting beam in order to evaluate the shear deformation in that beam, which corresponds to the deflected shape. The following formula determines the overstrength shear capacity:

$$V_{os} = 2\emptyset_\circ A_{sd} f_y \sin \propto + N_{oc} \tan \propto \tag{12}$$

where $A_{sd}$ is the area of diagonally bar, α is the angle the inclination sustains with the x-axis of the beam, ∅ is the overstrength factor equal to 1.35, and $N_{oc}$ is the axial force calculated by:

$$N_{oc} = \emptyset_\circ f_y A_{sf} \tag{13}$$

where $A_{sf}$ is the bar area side-by-side to the direction of the wall.

In the ACI code, 2019 (American Concrete Institute, 2019) the shear stress of connection beam is evaluated by:

$$V_n = 2A_v f_y \sin \propto \leq 0.83\sqrt{f_c'} A_w \tag{14}$$

where $A_v$ is the area of cross section of the diagonal bars for each group ($mm^2$), fy is the yield stress of the inclined bar (MPa), α is the angle between the inclined steel reinforcement and the longitudinal axis of the connection beam, and $A_w$ is the cross-section area of connection beam ($mm^2$). However, the following equation may be used to evaluate the shear resistance of conventional connection beams:

$$V_n = A_{cv}\left(\propto_c \lambda \sqrt{f_c'} + \rho_t f_{yt}\right) \leq 0.67 A_{cv} \sqrt{f_c'} \tag{15}$$

where $A_{cv}$ refers to the area of concrete, fc' is the concrete compressive resistance, $\rho_t$ is the ratio of the shear reinforcement, $f_{yt}$ is the yield stress of the horizontal bar, ⅄ is the correction factor which is depending on the unit weight

of concrete. The factor ∝c difference is based on the value of the span to depth ratio. Particularly, when clear span to depth ratio less than 1.5, αc equal to 0.25, when clear span to depth ratio more than 2, αc=0.17, and when clear span to depth ratio between 1.5 and 2, it transitions linearly between 0.25 and 0.17 (Metwally, 2019).

Additionally, $\emptyset V_n$ refers to the designed shear resistance, where for inclined reinforced connection beams, ∅=0.85 for shear. For conventionally reinforced connection beams, ∅=0.75 for shear and ∅=0.9 for flexure (Paulay & Binney, 2011). In contrast to the shear capacity of conventional connection beams, the shear capacity of steel RC coupling beams (SRCC beams) is calculated differently.

In order to prevent crushing concrete at the web zone, the ACI 318 code (2019) limits the maximum shear as shown in Eq. (16) to is intended for beams with the standard arrangement. However, the presence of diagonal bars eliminates the need for this restriction because they significantly increase the shear capacity of connection beams.

Gong and Shahrooz (2001) calculated the predicted shear capacity formula. The equation is influenced by both the steel beam and the reinforced concrete enclosure.

$$V_n \le 0.83\sqrt{f_c'}\,b_h \tag{16}$$

$$V_n = 1.6\left[0.6f_y\left(d-2t_f\right)t_w + \frac{\sqrt{f_c'}}{6}b_c d_c + \frac{A_v f_y d_c}{s}\right] \tag{17}$$

where $f_y$ is the minimum yield stress of steel structure, $d_f$, $t_f$ and $t_w$ are the depth, thickness of flange and thickness of web of steel member. $b_c$ and $d_c$ are the effective depth and width of concrete. $A_v$, $f_y$ and s are the area, yield stress and distance between shear bars.

Equation (17) was modified by S. Tawil, et al. (2010) as shown below:

$$V_n = 1.1\frac{f_{ye}}{f_y}\left(0.6f_y d t_w\right) + 1.56\left[\frac{\sqrt{f_c'}}{6}b_c d_c + \frac{A_v f_y d_c}{s}\right] \tag{18}$$

where $f_{ye}$ is the expected yield stress of steel structure.

Design specifications for steel reinforcing concrete composite connection beams with shear walls are provided by the «AISC Seismic Provisions for Structural Steel Buildings» (Taranath, 2016). Different shear capacity equations are proposed by AISC recommendations based on whether the boundary walls are conventional or special structural walls. The ASCE-recommended anticipated shear capacity of SRCC beams for regular structural walls is determined as follows:

$$V_n = \frac{f_{ye}}{f_y}\left(0.6f_y d t_w\right) + \left[\frac{\sqrt{f_c'}}{6}b_c d_c + \frac{A_v f_y d_c}{s}\right] \tag{19}$$

According to research by E. Lim, et al. (2016) the shear capacity contribution of inclined compression bars may be interpreted as their yielding strength, but the shear capacity contribution of diagonal tension reinforcement should consider an overstrength factor Ω to exhibit the strain hardening impact. There are two possible causes of the overstrength factor: 1) the variation between the yield strength that was stated and the real yield resistance; and 2) the strain hardening impact. If the designated yield strength is utilized, ACI 318 suggests Ω = 1.25. The mean ratio of the required yield strength to the actual yield strength was around 1.13. Therefore, if the real yield stress is utilized, the overstrength factor may be calculated as 1.25/1.13 = 1.10 (Gregor et al., 1983).

In the conventional flexural approach [35], the «Whitney Stress Block» is used to determine the maximum shear resistance that corresponds to the moment capacity based on the following two formula:

$$V_{nf} = \frac{2M_n}{l_n} \tag{20}$$

$$M_n = 1.25\left(f_{yt}A_{st} + f_{yd}A_{sd}\cos\gamma\right)\left(d - \frac{c_d}{2}\right) \tag{21}$$

where $V_{nf}$ is the nominal shear resistance, $M_n$ is the nominal moment, $l_n$ clear length of the connection beam, $f_{yt}$ is the yield resistance of top bars, $A_{st}$ is the top steel area, $f_{yd}$ is the yield resistance of inclined reinforcement, $A_{sd}$ is the area of diagonal reinforcement, γ is the angle of inclined bar, $d$ is the effective depth, and $c_d$ is the depth of block.

However, overestimating the shear strength of diagonally reinforced connection beams may negatively impact the seismic performance of connected shear wall systems. For coupling beams to operate properly during earthquakes, accurate estimations of their shear strength must be used in their development (Gregor et al., 1983).

Whan et al. (2016) evaluated a study to predict the shear capacity of coupling beams. Following their research, they concluded that the equation suggested in the ACI code was the most effective, thus they made the following changes to make it more precise:

$$V_n = \gamma V_s + V_{ACI} \tag{22}$$

where γ is the contribution of shear reinforcement and can be calculated as follows:

$$\gamma = 1.6524(\rho_t)^{-0.3112}\left(\frac{l_n}{h}\right)^{-1.167} \tag{23}$$

is the shear resistance of shear reinforcement and can be determined by:

$$V_s = \frac{A_v f_y d}{s} \tag{24}$$

is the shear capacity of connection beam according to ACI code obtained through Eq. (14).

In 2017, B. Mihaylov and R. Franssen developed a unique mechanical model for the shear flexure interaction at the critical end sections of short conventional connecting beams (Mihaylov & Franssen, 2017). By achieving a balance between accuracy and simplicity, the model assesses resistance against sliding shear and inclined compression collapse. The shear resistance of a typically reinforced connection beam is determined using the same methods as in Equation (20) of the Mihaylov and Franssen model. Eq. (23), however, determines the comparable flexural strength.

$$M_n = \varepsilon_s A_{st}(d - \lambda z) \tag{25}$$

where $\varepsilon_s$ represents the strain in the tension bars. The quantity z is derived from the balance of the forces in the flexural tension bar and the inclined strut, according to Eq. (26).

$$z = \frac{\varepsilon_s A_{st}}{\lambda \eta f_c' b_w cos^2 \theta_c} \quad (26)$$

A progressive procedure is needed to determine z. The constants λ and η stand for the stress block properties, whereas θc indicates the angle of the strut concerning the longitudinal axis of the beam.

A shear resistance model for short and moderately connected beams with adequately developed flexural bars was developed by Park et al. (2020).

Equation (27) describes how the model considers not just the contributions of inclined and longitudinal bars but also the shear resistance that the concrete offers (Park et al., 2020).

$$V_n = 0.2 f_c' A_{cw} + 2 f_{yt} A_{st} \sin\gamma + 2 f_{yd} A_{sd} \sin\gamma \quad (27)$$

assuming that the failure angle γ is the same for the longitudinal and diagonal reinforcement.

Yang et al. (2022) used the «Softened Strut-and-Tie Model» (SSTM), created Hwang and Lee, (2002), to forecast the shear resistance of deep connection beams, despite the fact that it was initially created for deep beams, corbels, squat walls, and the joints between beam and column. Yang observed that the inclined reinforcing bar contribution and the diagonal concrete compressive strut contribution are the two components of the shear strength equation, and they are described as follows:

$$V_n = K \xi f_c' A_{str} \sin\theta_s + 2 f_{yd} A_{vd} \sin\gamma \quad (28)$$

Where $A_{str}$ is the cross-section area of the concrete strut, K is the constant that denotes the strut-and-tie index based on the orthogonal shear reinforcement, and $\xi$ is the coefficient of softening determined by:

$$\xi = \frac{335}{\sqrt{f_c'}} \leq 0.52 \quad (29)$$

P. Chetchotisak et al. (2024) created a unique strut-and-tie model (STM) that incorporates shear–flexure interaction (SFI) to predict shear collapse in deep connection beams. Data from experiments confirmed the accuracy. The following formula was used:

$$V_n = V_{nc} + V_w + V_h + V_d \quad (30)$$

$$V_{nc} = \frac{1}{\left(\frac{1}{1.25 f_c' b_w c_b \sin\theta_s}\right) + \left(\frac{1}{3.08 f_{yt} A_{st} \tan\theta_s}\right)} \quad (31)$$

$V_{nc}$, which refers to the shear resistance from the strut mechanism, should be equal to or less than the value from Eq. (32).

$$0.85 f_c' b_w c_b \sin\theta_s \quad (32)$$

$C_b$ indicates the flexural compression zone's depth, and θs represents the inclined compression inclination angle of the strut. The two equations below can be used to calculate both:

$$c_b = \frac{1.25 f_{yt} A_{st}}{0.85 f_c' b_w} \quad (33)$$

$$\tan\theta_s = \frac{h - c_b}{l_n} \quad (34)$$

$V_w$ is the shear resistance from stirrups:

$$V_w = 0.29 f_{yv} A_v \quad (35)$$

$V_h$ is the shear resistance from horizontal bars:

$$V_h = f_{yh} A_h \tan\theta_s \quad (36)$$

$V_d$ is the shear resistance from diagonal bars:

$$V_d = 2 \times 0.89 f_{yd} A_{vd} \sin\gamma \quad (37)$$

# 9. TYPES OF COUPLING BEAMS

There are several types of coupling beams, depending on the method of distributing the reinforcing steel and the added materials, that can be summarized as follows:

## 9.1. Diagonal and conventional connection beams

The seismic and shear resistance of conventional reinforced concrete connection beams are challenged by strong earthquakes and wind stresses, respectively (Chetchotisak et al., 2024).

Kwan and Zhao (2002) studied the cyclic behavior of short connection beams. They improved test technique that can properly replicate the boundary conditions of connection beams in coupled wall constructions which were used to evaluate six half-scale samples of connection beams with aspect ratios < 2·0 under repeated load. The first model was diagonally reinforced, while the other five were conventionally reinforced. The primary structural factors under investigation were the aspect ratio and the steel bars arrangement. The deep traditionally reinforced connection beams performed quite differently from the regular beams in frame systems, according to test data. Shear collapse was more likely to happen in general. Furthermore, bending strength may be further increased by the extra longitudinal reinforcing bars (those positioned close to the centroidal axis), which would raise the shear demand. However, for deep coupling beams, the normally reinforced coupling beams' measured drift ratios nevertheless reached 3·6% to 5·7%, which is not insignificant. Nonetheless, it was discovered that the addition of inclined reinforcement greatly enhanced the ability of the connection beam to dissipate energy and fundamentally altered the load-resisting mechanism. Even so, it did not affect the deformability of the connection beam.

Naish and Wallace, (2010) examine the testing of inclined connection beams as part of their investigation by utilizing different detailed choices, analyzing popular modeling techniques, and determining how reinforced and post-tensioned slabs affect the load-deformation response of beams. Three specimens were built using slabs that were 4" thick and had an aspect ratio of 2.4. Without post-tensioning strands, one model had a reinforced slab with bars on the upper and lower in a transverse direction and the other had just at the top in a longitudinal direction. Also, two specimens had a comparable reinforced, but they were additionally strengthened with strands that were post-tensioned distributed longitudinally on the slab. The model with full confinement and a stress slab had the peak shear resistance. The shear capacity of the connection beam is increased by around 15%

to 20% when a reinforced concrete slab is added. The test findings show that, in comparison to confinement around the diagonal bars according to ACI 318-05, entire section confinement according to ACI 318-08 offers excellent, if not improved, performance. Nevertheless, they concluded that beams detailed by the new ACI 318-08 provision, which permits full section confinement, perform better in terms of resistance and ductility than beams detailed by the previous ACI 318-05 provision, requiring the confinement of the diagonal bar groups.

O. TAHA, (2013) presented a study about the impact of inclined reinforcement on the connection beams. Three models were tested with the same dimensions and with varied types of reinforcement. One model included diagonal bars enclosed by spiral stirrups, while the other two had diagonal bars free of stirrups, and the third had a steel plate. In comparison to other specimens, the results of the connection beam reinforced with diagonal bars and spiral stirrups demonstrated a high shear capacity resistance. The coupling beam with diagonal reinforcement alone demonstrated a high performance comparable to that of the spiral stirrups, while the third specimen of the coupling beam with steel plate demonstrated a weak ability to dissipate the shear stresses.

Han, et. al, (2019) investigated how the seismic performance of inclined reinforced concrete coupling beams was affected by transverse reinforcement. Seven specimens with varying transverse reinforcement levels and aspect ratios were used in static cyclic testing. Four specimens had span to depth ratio equal to 2, while the other three had span to depth ratio equal to 3.5. They found that the cyclic performance of connection beams, including failure modes, was significantly influenced by the amount of transverse reinforcement. The cyclic behavior of specimens improved as the quantity of transverse reinforcement increased. Regardless of the number of transverse bars, all specimens with span to depth ratio equal to 2 generated shear strengths Vu greater than the shear strength determined using the ACI 318 shear strength equation. However, the degree of overstrength (Vu/VACI) increased as the quantity of transverse reinforcement increased. Observations were comparable for specimens with span to depth ratio equal to 3.5. This suggests that the degree of transverse reinforcement has a significant impact on the shear strength of specimens.

Ameen, et. al, (2020) presented research on diagonal connection beams with high resistance steel reinforcement (grade 60 and 120). Four specimens were tested under repeated loads to study the effect on diagonal reinforcement, shear stress, and longitudinal reinforcement details (either extending to the wall reinforcement or being cut at the wall face). The compressive strength ranged from 41 MPa to 50 MPa. The results showed that grade 120 diagonal reinforcement could be a suitable substitute for grade 60 diagonal reinforcement. Specimens with grades 60 and 120 inclined bars had chord rotation capabilities of 7.1% and 5.1%, respectively. However, the initial effective stiffness was reduced by around 40%, and the hysteretic energy dissipation and residual chord rotation (for chord rotations between 3% and 5%) were reduced by 50% when the grade 60 to 120 bars changed. Localized damage was seen at the beam-wall interface in coupling beams with non-diagonal longitudinal reinforcement cutoff close to the wall face; damage was more evenly distributed across the beam span when those bars were extended into the end blocks. Deformation capabilities were unaffected by this variation in detailing, most likely because, regardless of the non-diagonal longitudinal reinforcing detail, diagonal bar buckling occurred at similar chord rotation loads.

## 9.2. Fiber coupling beam

Building connection beams with inclined reinforcement may be challenging and laborious, particularly if the inclined bars at the edges of neighboring shear walls must be threaded through dense confinement steel. As demonstrated by recent studies of connection beams made of high-performance fiber-reinforced concrete (high performance denoting a strain-hardening behavior in tension), the percentage of the moment and shear attributed to the inclined reinforcement can be greatly decreased, and the requirement for its confinement can be eliminated. In order to successfully contain the decreased quantity of diagonal reinforcement, high-performance fiber-reinforced concrete (HPFRC) reacts with a minimal amount of transverse reinforcement and operates similarly to confined concrete. When coupling beams are subjected to significant cyclic reversals of shear deformations, the HPFRC also helps to increase their shear resistance and stiffness (Wight & MacGregor, 2012; Son et al., 2024). The use of fibers in the coupling beams significantly increases their shear resistance (Afsin et al., 2004).

J. Kuang and B. Baczkowski, (2006) studied the shear resistance of steel fibers RC connection beams. This study focused on understanding the shear behavior and shear resistance of large-scale steel fiber reinforced concrete coupling beams under monotonic loading. Three large-scale coupling beams were made. The span-to-depth ratios of the specimens vary, but their cross-sectional characteristics are the same. Three values of aspect ratio were used: 1, 1.5, and 2. The flexural mode of failure has been prevented by providing longitudinal reinforcement of 1.05% at the top and bottom of the beams and a transverse reinforcement ratio of 1.0% in the form of stirrups. The water-to-cement ratio is 0.45, and fly ash replaces around 25% of the cement. Cube compressive strength is 48.4 MPa. Every cubic meter of concrete has an addition of about 80 kg of steel fiber. The findings indicated that the shear capacity of the SFRC connection beam with a low span/depth ratio is higher than that with a higher span/depth ratio. According to the testing, the shear behavior of concrete components may be significantly enhanced by even small additions of steel fibers. It has been demonstrated that steel fiber significantly improves the shear strength of conventional concrete. The shear capacity of the SFRC coupling beams is considerably higher than that of the traditional reinforced concrete ones.

Jang, et al., (2015) investigated the viability of simplifying the reinforcement details of critical members using high-performance steel fiber reinforced concrete. The impact of a 1.5% steel fiber content on the shear behavior of an inclined RC connection beam without extra stirrups was examined in order to simplify intricate reinforcing details for the confinement of inclined bar groups in the whole section. The compressive resistance was 60 MPa and 100 MPa and span to depth ratio equal to 2. According to the test results, adding steel fibers had a major impact on the mechanical characteristics of the high-performance coupling beam. In comparison to inclined RC connection beams (CCB) with full section confinement details, the addition of 1.5% steel fiber content, HPC coupling beam produces comparable cracking and structural behaviors for a diagonally reinforced coupling

beam (SFRCCB) without additional transverse reinforcement. Nevertheless, CCB had more ductility than SFRCCB. When 1.5% steel fibers were added to 60MPa and 100MPa HPC, the modulus of rupture increased by a maximum of 42.3% and 30.0%, respectively, in comparison to HPC without steel fibers. However, deformed steel fibers can be used instead of minimum shear reinforcement where hooked-end steel fiber volume fractions of 1.2% and 1.5% are adequate to meet the flexural performance requirements outlined in ACI318-08S5.6.6. More tiny fractures are dispersed throughout the SFRC coupling beam as a result of the crack-bridging effect of steel fibers. Shear distortion is lessened as a result of fine fractures.

A. Irizarry, (2016) evaluated the behavior of the coupling beam under cyclic loading with varied types of steel fibers (varied properties and dosage) without diagonal reinforcement. Tests were conducted on eight specimens of coupling beams with aspect ratio equal to 2 and 3 under lateral displacement reversals. A precast, rectangular coupling beam was attached to two large rectangular pieces representing the end sections of two walls being linked to create each coupling beam specimen. Three fiber volume fractions were employed (1.0%, 1.25%, and 1.5%). Tested coupling beams with an aspect ratio can demonstrate stable behavior and obtain drift capabilities of at least 5.0% flexural dominated behavior when exposed to large deformation reversals. Nevertheless, a hardening behavior under direct strain and a noticeable deflection hardening under bending were the outcomes of using steel fibers at a 1.5% volume fraction. The portion at the interface of the dowel reinforcement and the connection beam-to-wall contact is a crucial area that needs to be considered when evaluating the resistance of the coupling beam.

Jang, et al., (2018) examined how the seismic behavior of inclined reinforced connection beams made of normal- and high-resistance concrete was affected by the use of steel fibers as shear reinforcement. Quasi-static reversed cyclic loading was used to manufacture and test four different kinds of coupling beams. Following ACI 318-14, a reinforced concrete connection beam with a compressive strength of 40 MPa was built with full confinement. To evaluate the impact of strength, a second RC connection beam specimen was also constructed using identical reinforcing details and concrete with a compressive resistance of 80 MPa. Additionally, an effort was made to simplify the intricate features of transverse reinforcements for diagonally reinforced concrete connection beams by utilizing steel fiber. This was achieved by using two fiber volume fractions for 40 MPa and 80 MPa steel fiber-reinforced concrete (SFRC) connection beams, respectively, of 1.0% and 1.25%. According to test results, when the compressive strength grew, so did their shear strength. In contrast, the ordinary- and high-resistance concrete RC connection beams had comparable energy dissipation capacities. Further, this study discovered that adding steel fiber gave the diagonal steel rebar greater transverse reinforcement and prevented it from buckling. The SFRC coupling beams performed similarly to the traditional concrete connection beams in terms of resistance, stiffness degradation, and energy dissipation capacity. The use of steel fiber makes it possible to simplify the transverse reinforcement construction details for inclined reinforced coupling beams, according to comparisons between the traditional concrete and SFRC beam specimens.

## 9.3. Steel and composite coupling beams

The seismic resistance of connection beams can be increased by using steel, concrete as encasing, steel fiber concrete, diagonal reinforcement, and HPFRC materials (Paulay & Binney, 2011). Researchers tried a different design using steel material to enhanced the seismic performance of connection beams and overcome the shortcomings of inclined RC connection beams in construction. This is because steel link beams offer exceptional ductility and energy dissipation.

Harries et al., (1985) used steel coupled beams inserted in reinforced concrete walls. Two full-scale connection beams under cyclic stress made up the specimens. According to the test findings, using steel coupling beams offered superior energy absorption and ductility. Coupling beams performed similarly to coupled beams in eccentrically braced frames for small and medium aspect ratios.

Gong and Shahrooz (2001), carried out more research on steel and composite connection beams and proposed the steel-concrete composite connection beam as a workable option for connection beams. The study concentrated on the impacts of the encasement around the coupling beams as well as the repeated response of composite connection beams. According to the trial results, encasing steel coupling beams improved their capacity to prevent web buckling and reduced the need for web stiffeners. For the first time, Subedi, (1989) suggested using steel plate composite beams. Tests confirmed that steel plate concrete composite beams perform better in shear loads than regular beams. Lam et al., (2005) investigated coupling beams with or without shear studs that had a steel plate implanted vertically throughout the span. The findings demonstrated that coupling beams' strength and stiffness might be increased by including steel plates. The usage of steel tubular beams filled with concrete was initially suggested by Teng et al., (1999). An experimental investigation revealed that the steel pipe's lower tensile zone failed and cracked.

To improve the seismic behavior of reinforced concrete (RC) connection beams, embedded steel plate reinforced concrete (PRC) coupling beams have recently been added to the coupling beam family. However, the efficiency of this combination is significantly diminished by the brittle crushing and spalling of concrete in these composite elements, which significantly lowers their deformation behavior and energy-dissipating capacity (Hou et al., 2019).

W. Hou, et al., (2019) suggested a new kind of composite connection beams called steel plate reinforced high toughness concrete (PRHTC) connection beams in response to this significant drawback. This innovative component replaced the traditional reinforced concrete with high-toughness concrete (HTC), a type of quasi-strain-hardening cementitious mixture with quasi-ductile properties. The seismic stability of PRHTC deep connection beams (span-to-depth ratio equal to 1.5) with different steel plate reinforcement ratios is the primary focus of their study. According to the test results, the PRHTC coupling beams have a ductile flexural failure mechanism and a high capacity for energy dissipation. Multiple cracking patterns are displayed by the high-tough concrete in this composite part, which also retains the desired integrity. All specimens demonstrated outstanding stiffness and strength retention capacities, achieved high-level ductility factors above 5.5, and withstood significant rotations ranging from

0.064 to 0.078 rad. However, it is demonstrated that the steel plate ratio between 4.31% and 6.47% is suitable and efficient for preserving the excellent ductility and rotation deformity of the PRHTC connection beams.

## 10. CONCLUSIONS

Coupled systems support and protect the structure from lateral loads, making them excellent earthquake-resistant systems. Shear walls and cantilever walls differ in base shear requirements and damping models. Cantilever wall models have a slight increase in fundamental period, while shear walls are less sensitive to changes in damping coefficients. The degree of connection significantly influences seismic behavior in coupled systems, with low coupling causing a coupled wall and high coupling causing a pierced wall. For coupling beams that are not covered by ACI Code, a amalgamation of inclined and conventional reinforcement would be more useful than using only one. Increased shear reinforcement can lead to shear-sliding failure in beam-wall joints, while suppressing shear-tension failure. However, restricting axial elongation can increase shear capacity but ultimately result in brittle failure. Shear wall structures should have a strong coupling wall and a weak coupling beam, ensuring stiffness during earthquakes to prevent the shear wall from collapsing first. Moreover, the new ACI 318 provision, which allows full section confinement, outperforms the previous ACI 318 provision, which necessitates di-agonal bar group confinement. After reviewing previous research, the most effective factors affecting the performance of connecting beams were identified: the arrangement of reinforcement, span/depth ratio, cross-section dimension, and detailing of confinement. Recent studies show that high-performance fiber-reinforced concrete can significantly reduce the moment and shear of inclined reinforcement, getting rid of the need for confinement and operating similarly to confined concrete. Because of brittle crushing and spalling, embedded steel plate reinforced concrete connection beams are less effective. High-toughness concrete is an innovative solution for this problem, offering a ductile failure mechanism and high energy dissipation capacity, replacing traditional reinforced concrete.

## NOTATIONS

| | |
|---|---|
| $A_{cv}$ | Area of concrete |
| $A_s$ | Area of steel |
| $A_{str}$ | Cross section area of concrete strut |
| $C_u$ | Compression force |
| $d$ | Effective depth of coupling beam |
| $DOC$ | Degree of coupling |
| $E$ | Earthquake force |
| $f'_c$ | Compressive strength |
| $f_y$ | Yield strength |
| $l_n/h$ | Clear span/depth ratio |
| $M_{n1}$ | Base moment of wall 1 |
| $M_{n2}$ | Base moment of wall 2 |
| $M_o$ | Total moment |
| $N_{oc}$ | Axial force |
| $PSD$ | Peak shear demand |
| $t_f$ | Thickness of flange |
| $T_u$ | Tension force |
| $t_w$ | Thickness of web |
| $V_{bi}$ | Shear force at each end of coupling beam |
| $V_u$ | Ultimate shear strength |
| $l$ | Distance between wall 1 and wall 2 C/C |
| Ø | Overstrength factor |
| α | Angle between inclined bar and X-axis |
| γ | Contribution of shear reinforcement |

**Author contributions:** Mariam Ibraheem M. Hussein: Conceptualization, Methodology, Investigation, Validation, Visualization, Writing – original draft, Writing – review & editing.

Mohammed M. Rasheed: Supervision, Validation, Visualization, Writing – review & editing.

Asma Mahdi Ali: Supervision, Validation, Writing – review & editing.

**Funding:** The authors declare that no funding was received for this study.

**Acknowledgments:** The authors express their gratitude to Mustansiriyah University in Baghdad, Iraq (www.uomustansiriyah.edu.iq) for their assistance with this work.

**Conflicts of interest:** The authors want to make it clear that publishing this work does not create a conflict of interest.

## REFERENCES

Afsin, B., Gustavo, J., & James, K. (2004). *Behavior of precast high-performance fiber reinforced cement composite coupling beams under large displacement reversals*. In *13th World Conference on Earthquake Engineering* (pp. 1–15). Canada.

Adhikari, R. (2015). *Optimum degree of coupling for the efficient seismic response of reinforced concrete coupled walls* (Thesis, pp. 1–68). Tokyo Institute of Technology.

Ameen, S., Lequesne, R., & Lepage, A. (2020). Diagonally reinforced concrete coupling beams with Grade 120 (830) high-strength steel bars. *ACI Structural Journal, 117*(6), 199–210. https://doi.org/10.14359/51728067

American Concrete Institute. (2019). *Building code requirements for structural concrete (ACI 318-19) and commentary on building code requirements for structural concrete (ACI 318R-19)*.

Boivin, Y. (2006). *Assessment of the seismic performance of a 12-storey ductile concrete shear wall system designed according to the NBCC 2005 and the CSA A23.3 2004 standard* (Thesis, pp. 1–220). University of Sherbrooke.

Chetchotisak, P., Teerawong, J., & Hansapinyo, C. (2024). Strut-and-tie model including shear–flexure interaction for predicting shear capacity of reinforced concrete short coupling beams. *Structures, 66*, 1–11. https://doi.org/10.1016/j.istruc.2024.106791

Cheng, M., Fikri, R., & Chen, C. (2014). Experimental study of reinforced concrete and hybrid coupled shear wall systems. *Engineering Structures, 82*(1), 214–225. https://doi.org/10.1016/j.engstruct.2014.10.039

Daniel, T., & Joel, A. (2022). Experimental testing on the structural capacity of coupling beams with non-anchored longitudinal rebars. *MATEC Web of Conferences, 346*, 1–8. https://doi.org/10.1051/matecconf/202236404017

Eljadei, A., & Harries, K. (2014). Design of coupled wall structures as evolving structural systems. *Engineering Structures, 73*, 100–113. https://doi.org/10.1016/j.engstruct.2014.05.002

El-Tawil, S., Harries, K., Fortney, P., Shahrooz, B., & Kurama, Y. (2010). Seismic design of hybrid coupled wall systems: State of the art. *Journal of Structural Engineering, 136*(1), 755–769. https://doi.org/10.1061/(ASCE)ST.1943-541X.0000186

Eurocode 2. (2004). *Design of concrete structures – Part 1-1: General rules and rules for buildings* (pp. 82).

Federal Emergency Management Agency. (1998). *Evaluation of earthquake damaged concrete and masonry wall buildings* (FEMA 306). Washington, DC.

Freddia, F., Galassoa, C., Cremena, G., Astab, A., Sarnoc, L., Giaralisd, A., Urzuaa, F., Chuquitaypee, C., Mitoulisf, S.,

Petroneg, C., Sextosh, A., Sousai, L., Tarbalia, K., Tubaldic, E., Wardmanj, J., & Wook, G. (2021). Innovations in earthquake risk reduction for resilience: Recent advances and challenges. *International Journal of Disaster Risk Reduction, 60*, 102267, 1–31. https://doi.org/10.1016/j.ijdrr.2021.102267

Gong, B., & Shahrooz, B. (2001a). Concrete-steel composite coupling beams. I: Component testing. *Journal of Structural Engineering, 127*(6), 625–631. https://doi.org/10.1061/(ASCE)0733-9445(2001)127:6(625)

Gong, B., & Shahrooz, B. (2001b). Steel-concrete composite coupling beams—Behavior and design. *Engineering Structures, 23*(11), 1480–1490. https://doi.org/10.1016/S0141-0296(01)00042-6

Gregor, J., Mirza, A., & Ellingwood, B. (1983). Statistical analysis of resistance of reinforced and prestressed concrete members. *ACI Journal Proceedings, 80*(3), 167–176. https://doi.org/10.14359/10715

Han, S., Kim, S., & Kim, T. (2019). Effect of transverse reinforcement on the seismic behavior of diagonally reinforced concrete coupling beams. *Engineering Structures, 196*, 1–15. https://doi.org/10.1016/j.engstruct.2019.109307

Harries, K. (2001). Ductility and deformability of coupling beams in reinforced concrete coupled walls. *Earthquake Spectra, 17*(3), 457–478. https://doi.org/10.1193/1.1586184

Harries, K., Cook, W., Mitchell, D., & Redwood, R. (1995). *The use of steel beams to couple concrete walls*. In *7th Canadian Conference on Earthquake Engineering*. Montreal, Canada. Harris, M., & Wijanto, S. (2000). Some differences between coupled wall and cantilever wall structures. In *12th World Conference on Earthquake Engineering* (pp. 1–8). Auckland, New Zealand.

Hindi, R., & Hassan, M. (2004). Effect of confinement on the behavior of diagonally reinforced coupling beams. In *13th World Conference on Earthquake Engineering* (pp. 1–14). Canada.

Hoenderkamp, J. (2012). Degree of coupling in high-rise mixed shear walls structures. *Sadhana, 37*(4), 481–492. https://doi.org/10.1007/s12046-012-0087-z

Hou, W., Xu, S., Ji, D., Li, Q., & Zhang, P. (2019). Seismic performance of steel plate reinforced high toughness concrete coupling beams with different steel plate ratios. *Composites Part B: Engineering, 159*(15), 199–210. https://doi.org/10.1016/j.compositesb.2018.09.100

Hwang, S., & Lee, H. (2002). Strength prediction for discontinuity regions by softened strut-and-tie model. *Journal of Structural Engineering, 128*(12), 1519–1526. https://doi.org/10.1061/(ASCE)0733-9445(2002)128:12(1519)

Irizarry, A., & Montesinos, G. (2016). *Evaluation of seismic behavior of coupling beams with various types of steel fiber reinforced concrete* (Research project report, pp. 1–120). University of Wisconsin–Madison.

James, M., Sullivan, T., & Beyer, K. (2014). Capacity design of coupled RC walls. *Journal of Earthquake Engineering, 18*(5), 735–758. https://doi.org/10.1080/13632469.2014.904255

Jang, S., Jeong, G., & Yun, H. (2018). Use of steel fibers as transverse reinforcement in diagonally reinforced coupling beams with normal- and high-strength concrete. *Construction and Building Materials, 187*(30), 1020–1030. https://doi.org/10.1016/j.conbuildmat.2018.08.063

Jang, S., Kang, D., Ahn, K., Park, W., Kim, S., & Yun, H. (2015). Feasibility of using high-performance steel fiber reinforced concrete for simplifying reinforcement details of critical members. *International Journal of Polymer Science, 2015*, 850562, 1–12. http://dx.doi.org/10.1155/2015/850562

Kuang, J., & Baczkowski, B. (2006). Shear capacity of steel fibre reinforced concrete coupling beams. In *Joint International Conference on Computing and Decision Making in Civil and Building Engineering* (pp. 3837–3846). Canada.

Kwan, A., & Zhao, Z. (2002). Cyclic behaviour of deep reinforced concrete coupling beams. *Structures & Buildings, 152*(3), 283–293.

Lam, W.-Y., Su, R.K.-L., & Pam, H.-J. (2005). Experimental study on embedded steel plate composite coupling beams. *Journal of Structural Engineering, 131*(8), 1294–1302. https://doi.org/10.1061/(ASCE)0733-9445(2005)131:8(1294)

Lequesne, R., Montesinos, G., & Wight, J. (2013). Seismic behavior and detailing of high-performance fiber-reinforced concrete coupling beams and coupled wall systems. *Journal of Structural Engineering, 139*(8), 1362–1370. https://doi.org/10.1061/(ASCE)ST.1943-541X.0000687

Lim, E., Hwang, S., Wang, T., & Chang, Y. (2016). An investigation on the seismic behavior of deep reinforced concrete coupling beams. *ACI Structural Journal, 113*(2), 1–10. https://doi.org/10.14359/51687939

MacLeod, L. (1971). *Shear wall-frame interaction* (Special Publication SP011.01D, pp. 62). Portland Cement Association.

Metwally, I. (2019). *Seismic design of cast-in-place concrete walls and coupling beams based on ACI 318-19 & ASCE 7-22* (pp. 1–54).

Mihaylov, B., & Franssen, R. (2017). Shear-flexure interaction in the critical sections of short coupling beams. *Engineering Structures, 152*, 370–380. https://doi.org/10.1016/j.engstruct.2017.09.024

Naish, D., & Wallace, J. (2010). Testing and modeling of diagonally reinforced concrete coupling beams. In *9th U.S. National and 10th Canadian Conference on Earthquake Engineering* (pp. 1–10). Canada.

Nawy, E. (2008). *Concrete construction engineering* (pp. 6). Taylor & Francis.

Nouri, H., Rouz, K., Taghavi, M., Shakib, M., & Mianaji, S. (2016). Analyzing the effect of international standards details of reinforced concrete buildings on ductility and energy absorption of structure (A case study of Nakhjavan Palace Project). *Modern Applied Science, 10*(10), 165–179. https://doi.org/10.5539/mas.v10n10p165

NZS-3101.1 & 3101.2 NZ Code. (2006). *New Zealand standard: Concrete structure standard Part 1 and 2* (pp. 11–17).

Ocfaoa, J. (1987). Seismic behavior of slender coupled wall systems. *Journal of Structural Engineering, 113*(10), 2221–2234. https://doi.org/10.1061/(ASCE)0733-9445(1987)113:10(2221)

Park, R., & Paulay, T. (1975). *Reinforced concrete structures* (pp. 1–783). John Wiley & Sons.

Park, W., Kang, T., Kim, S., & Yun, H. (2020). Seismic performance of moderately short concrete coupling beams with various reinforcements. *ACI Structural Journal, 117*(3), 141–154. https://doi.org/10.14359/51723501

Paulay, T. (1971). Coupling beams of reinforced concrete shear walls. *Journal of the Structural Division, 97*(3), 76–88. https://doi.org/10.1061/JSDEAG.0002848

Paulay, T., & Binney, R. (2011). Diagonally reinforced coupling beams of shear walls. *International Concrete Abstracts Portal, 21*(52), 579–598. https://doi.org/10.14359/17302

Rivard, G., Ambroise, S., & Paultre, P. (2019). Influence of the degree of coupling on shear amplifications due to higher modes effects in RC partially coupled wall structures. In *12th Canadian Conference on Earthquake Engineering* (pp. 1–8). Canada.

Sakr, M., Khalifa, T., Darwish, E., & Batsh, O. (2023). A review on coupling beam types in coupled shear wall. In *International Conference on Advances in Structural and Geotechnical Engineering* (pp. 1–12). Egypt.

Shahrooz, B., Fortney, P., & Harries, K. (2018). Steel coupling beams with a replaceable fuse. *Journal of Structural Engineering, 144*(2), 1–8. https://doi.org/10.1061/(ASCE)ST.1943-541X.0001939

Son, D., Choi, J., Song, S., Choi, C., & Bae, B. (2024). Inelastic behavior of diagonally reinforced coupling beams confined with steel fibers. *Structures, 65*(26), 1–11. https://doi.org/10.1016/j.istruc.2024.106733

Son, N., Li, B., & Beyer, K. (2014). Effective stiffness of reinforced concrete coupling beams. *Engineering Structures, 76*, 371–382. https://doi.org/10.1016/j.engstruct.2014.07.014

Subedi, N. (1991). RC-coupled shear wall structures. I: Analysis of coupling beams. *Journal of Structural Engineering, 117*(3), 667–680. https://doi.org/10.1061/(ASCE)0733-9445(1991)117:3(667)

Subedi, N.K. (1989). Reinforced concrete beams with plate reinforcement for shear. *ICE Proceedings, 87*, 377–399.

Taha, O. (2013). *Influence of diagonal reinforcement with spiral stirrups on shear capacity of coupling beam in shear wall* (Thesis, pp. 1–72). Universiti Teknologi Malaysia.

Taranath, B. (2016). *Seismic provisions for structural steel buildings, ANSI/AISC 341-16* (pp. 114–116). American Institute of Steel Construction.

Teng, J.G., Chen, J.F., & Lee, Y.C. (1999). Concrete-filled steel tubes as coupling beams for RC shear walls. In *Advances in Steel Structures* (Vol. 1, pp. 391–399). https://doi.org/10.1016/B978-

008043015-7/50046-4
Thambi, D., & Prabha, C. (2017). Coupled shear wall: A review. *International Journal of Science Technology & Engineering, 3*(11), 135–136.
Whan, H., Wook, K., & Hee, H. (2016). Shear strength equation for slender diagonally reinforced coupling beam. *Journal of Earthquake Engineering Society of Korea, 20*(6), 361–368. https://doi.org/10.5000/EESK.2016.20.6.361
Wight, J., & MacGregor, J. (2012). *Reinforced concrete: Mechanics and design* (pp. 984–1080). Pearson.
Yang, C., Chen, S., Yen, C., & Hung, C. (2022). Behaviour and detailing of coupling beams with high-strength materials. *Journal of Building Engineering, 47*(2), 1–17. https://doi.org/10.1016/j.jobe.2021.103843
Ye, L. (2020). Seismic response assessment of a hybrid coupled wall structure with novel self-centering steel truss coupling beams. *Bulletin of Earthquake Engineering, 18*(12), 2657–2680. https://doi.org/10.1007/s10518-020-00801-7
Zhang, Z., Ou, J., Li, D., & Zhang, S. (2017). Optimization design of coupling beam metal damper in shear wall structures. *Applied Sciences, 7*(2). https://doi.org/10.3390/app7020137
Zhao, Z., Kwan, A., & He, X. (2004). Nonlinear finite element analysis of deep reinforced concrete coupling beams. *Engineering Structures, 26*(1), 13–25. https://doi.org/10.1016/j.engstruct.2003.08.014

**Mariam Ibraheem M. Hussein (1997):** is a PhD student in the Department of Civil Engineering, Faculty of Engineering, Mustansiriyah University. She holds an M.Sc. and a B.Sc. in Civil Engineering. Her research interests focus on structural analysis, seismic analysis, reinforced concrete structures, shear walls, and coupling beams. mariamib@uomustansiriyah.edu.iq

**Mohammed M. Rasheed (1972):** is an Assistant Professor in the Department of Civil Engineering, College of Engineering, Mustansiriyah University, Baghdad, Iraq. He obtained his Ph.D. and M.Sc. degrees in Structural Engineering from the University of Baghdad, and his B.Sc. degree in Civil Engineering from Al-Anbar University. His academic and research interests focus on structural engineering, earthquake engineering, reinforced concrete design, structural dynamics, and building construction. mmrk72@uomustansiriyah.edu.iq

**Asma Mahdi Ali (1983):** is a lecturer in the Department of Civil Engineering, College of Engineering, Mustansiriyah University, Baghdad, Iraq, since 2009. She obtained her Ph.D. and M.Sc. degrees in Civil Engineering with specialization in Building Materials Engineering from Mustansiriyah University, and her B.Sc. degree in Civil Engineering from the same university. Her academic and research interests focus on building materials, concrete technology, and construction engineering. asmaaali_civil@uomustansiriyah.edu.iq

# Workshop Aims and History

**AIMS:** Collaboration of prestigiuos associations **ACI, *fib* and RILEM** aimed to harmonize design rules and **jointly develop future code specifications** in the emerging fields of FRC and UHPFRC.

**HISTORY:** RILEM has been already active at the beginning of 1990'-ies in FRC. Since 2010, the *fib* and ACI have been collaborating to strengthen ties between their technical communities. Their first focus area was Fibre Reinforced Concrete (FRC), where both organizations had active committee: **ACI Commissions 544, 239, 549** and ***fib* Task Group T4.1.** These collaborations has led to a series of successful international workshops in the field of *Fibre Reinforced Concrete – From Design to Structural Applications:*

- **FRC 2014, Montreal, Canada,** *Fibre Reinforced Concrete – From Design to Structural Applications*, Polytechnique Montreal. Proceedings published in **ACI SP-310** and ***fib* Bulletin 79** (Editors: Bruno Massicotte, J-Philippe. Charron, G. Plizzari, Barzin Mobasher).
- **FRC 2018, Desenzano, Italy, Fibre** *Reinforced Concrete – From Design to Structural Applications* – Proceedings published in **ACI SP-343** and ***fib* Bulletin 95** (Editors: Bruno Massicotte, Fausto Minelli, Barzin Mobasher, Giovanni Plizzari).
- **FRC 2023, Tempe, Arizona, USA, Fibre** *Reinforced Concrete – From Design to Structural Applications* – Publications forthcoming (Editors: B. Massicotte, B. Mobasher, G. Plizzari).

The foundation for these workshops date back to **2004** with the first International Workshop on Advances in Fibre Reinforced Concrete held in **Bergamo, Italy**, organized by Giovanni Plizzari and Marco di Prisco during BEFIB 2004. This event, supported by ACI, focused on developing structural design methodologies for FRC (Editors: S. Ahmad, Marco di Prisco, Christian Meyer, Giovanni Plizzari, Surendra Shah).

- **Catania, Italy, 2007** – FRAMCOS 6 Workshop, chaired by Carpinteri, Ferro, and Giovanni Plizzari. Published in *Materials & Structures* (2009, Special Issue).
- **Budapest, Hungary, 1999** – Early conference on FRC, organized by György L. Balázs, bringing together international researchers *on Fibre Reinforced Concrete – from research to practice* http://fib.bme.hu/konyvek/szalerositesu_betonok.pdf

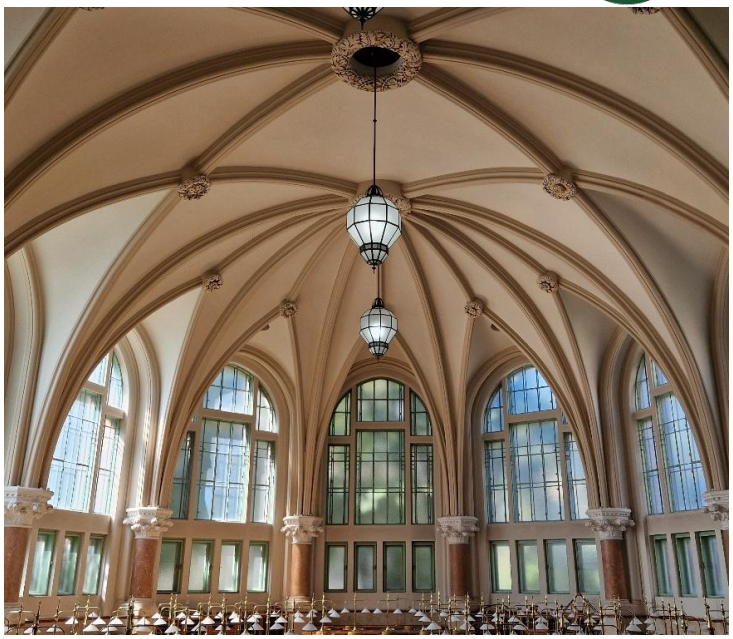

**Library of the Budapest University of Tecnology and Ecconomics**

# Venue – BME Budapest

Budapest University of Technology and Economics was founded in 1782 and it has been regarded as Hungary's number one technical higher education institution for more than 240 years.

Budapest, resting gracefully along the Danube, harmonizes centuries of history with a vibrant present. Landmarks like Buda Castle and Matthias Church echo tales of the past, while District VII's lively atmosphere embodies modern creativity in its eclectic bars and cafes. Art and culture thrive here, from the grandeur of the Hungarian State Opera House to the avant-garde exhibitions at the Ludwig Museum.

# Topics

1. Design specifications for applications
   - A. *fib* Model Code 2020
   - B. Standards and design specifications
   - C. Enhanced material behaviour and modelling
   - D. Enhanced structural behaviour and modelling in reinforced and in prestressed concrete members
2. Structural applications
   - A. Buildings, Bridges, Foundations
   - B. Tunnels
   - C. Prefabrication
   - D. Concrete industrial floors
3. Sustainability, Durability, Serviceability
   - A. Design aspects for sustainability and durability. Life Cycle Assessment.
   - B. Serviceability aspects: cracking, ~~first crack,~~ crack pattern, spacing of cracks, crack widths, increase of crack width
4. Design aspects for long term and extreme loads
   - A. Long term behaviour and modelling for shrinkage, creep, fatigue
   - B. FRC under fire, impact or blast loading.
5. Retrofitting and strengthening of existing structures
6. Fibres in new types of concretes and in 3D printed concretes

# Sponsorship opportunities

We offer levels of sponsorship: Diamond (8,000 EUR), Gold (5,000 EUR), Silver (2,500 EUR), and Standard (1,000 EUR). Diamond and Gold sponsors receive exhibition space (larger for diamond). Diamond, Gold and Silver receive complimentary workshop registrations (4 for Diamond, 3 for Gold and 2 for Silver). All sponsors will have their logo displayed and name acknowledged during the opening and closing ceremonies, in the workshop proceedings, and on-site materials such as flyers and roll-ups. To become a sponsor, please provide your company details, and the sponsorship fee must be transferred prior to the workshop.

Additionally a Platinum sponsorship level is also considerded and prize is assigned on special topic proposed by the Sponsor.

# Joint publication

The Workshop will conclude by a joint publication being part of the fib Series Proceedings (that is going to index by Scopus) as well as a Special Publication by ACI. We are also looking for a Summary of results for RILEM.

# Contact information

Official website:

**https://frcworkshop2026.bme.hu**

Műegyetem 3, Budapest, H-1111 Hungary

**frcworkshop2026@emk.bme.hu**

## Scientific Committee

György L. Balázs (HU), Chairman, BME
Sándor Sólyom (HU), Co-Chairman, BME
Kálmán Koris (HU), Co-Chairman, BME

**Advisory Board members of the Scientific Committee**

Marco di Prisco (IT), Politecnico di Milano
Giovanni Plizzari (IT), Università di Brescia
Bruno Massicotte (CA), Polytechnique Montréal
Jean-Philippe Charron (CA), Polyt. Montréal
Fausto Minelli (IT), Università di Brescia
Barzin Mobasher (US), Arizona State Univ

**Members**

Alejandro Perez Caldentey (ES)
Ana Elisabete P.G.A. Jacintho (BR)
Antoine Naaman (US)
Atef Daoud (TN)
Avraham Dancygier (IL)
Billy Boshoff (ZA)
Brecht Vandevvere (BE)
Bryan Barragan (FR)
Christian U. Grosse (DE)
David Fernandez-Ordoñez (CH)
Dirk Schlicke (AT)
Ekkehard Fehling (DE)
Elena Vidal Sarmiento (BE)
Éva Lublóy (HU)
Filippo Medeghini (DE)
Frank Dehn (DE)
Gabriele David Bocchino (IT)
Gábor Csorba (HU)
Gonzalo Ruiz López (ES)
Gustavo Parra Montesinos (US)
Gyorgy Farkas (HU)
Ildiko Merta (AT)
Imre Kovács (HU)
Ingrid Lande (NO)
István Sajtos (HU)
István Völgyi (HU)
Jan Cervenka (CZ)
Jan Vorel (CZ)
Jean Michel Torrenti (FR)
Joaquim Barros (PT)
Juan Navarro Gregori (ES)
Hans Beushausen (ZA)
Károly Péter Juhász (HU)
Klaus Holschemacher (DE
Liberato Ferrara (IT)
Lin Wan-Wendner (BE)
Lucie Vandewalle (BE)
Luis Segura (UY)
Matteo Colombo (IT)
Marek Salamak (PL)
Naser Alimrani (CA)
Nemy Banthia (CA)
Nicola Buratti (IT)
Nicola Tosic (ES)
Nilufer Ozyurt (TR)
Norbert Randl (AT)
Oliver Fenyvesi (HU)
Paolo Martinelli (IT)
Pedro Serna Ros (ES)
Peter Mark (DE)
Péter Schaul (HU)
Pierre Rossi (FR)
Raul Luis Zerbino (AR)
Ralf Winterberg (DE)
Ravindra Gettu (IN)
Robert Németh (HU)
Roman Wan-Wendner (BE)
Rutger Vrijdaghs (BE)
Salem G. Nehme (HU)
Sébastien Wolf (LU)
Sherif Abdel Aziz Yehia (AE)
Silvia Ientile (FR)
Stefan Bernard (AU)
Tamás Kovács (HU)
Tamon Ueda (JP)
Terje Kanstad (NO)
Todd Clarke (AU)
Tor Arne Martius-Hammer (NO)
Viktor Gribniak (LT)
Viktor Hlavicka (HU)
Vincent Oettel (DE)
Yuri Karinski (IL)
Zoltán Orbán (HU)

MŰEGYETEM 1782

## Organizer

Budapest University of Technology and Economics (BME),
Faculty of Civil Engineering

## Supported by:

ACI - https://www.concrete.org

*fib* - www.fib-international.org

RILEM - https://www.rilem.net

## Dates

| | |
|---|---|
| December 15, 2025 | Submission of abstracts |
| January 10, 2026 | Extended Abtract deadline |
| January 15, 2026 | Acceptance of abstracts |
| March 31, 2026 | Full paper submission |
| May 31, 2026 | Full paper review |
| July 1, 2026 | Full paper acceptance |

## Registration fee

| | |
|---|---|
| Early / regular | 600 / 700 EUR |
| Student / PhD student | 300 EUR |
| Banquet | 100 EUR |
| Early bird ends | July 15, 2026 |

Registration fee includes: Welcome cocktail, Coffee breaks, Lunches and Pre-Proceedings. It is required for every presentation to have a separate registration.

## Organizing Committee

Sándor Sólyom (HU), Chairman, BME
Kálmán Koris (HU), Co-Chairman, BME
György L. Balázs (HU), Co-Chairman, BME
János Czirják (HU)
Ahmed Seyam (UK) Adrienn Für-Kovács (HU) Jorge Luis Campoverde (HU)
András Bíró (HU) Tibor Mihucz (HU) Katalin Kopecskó (HU)
Bálint Somlai (HU) Csaba Miklós (HU) Marie Reymond (CH)
Corinne Bottollier Depois (CH), Ronny Ramiro Almeida Vasquez (HU)
Hatem Affez (HU) László Polgár (HU) László Sipos (HU) Szabolcs Szinvai (HU)

# ACI-*fib*-RILEM FRC-UHPFRC Workshop

*„Fibre Reinforced Concrete – From Design to Structural Applications"*

**Sept. 28 to 30, 2026 Budapest, Hungary**

ACI-*fib*-RILEM FRC WORKSHOP BUDAPEST 2026

**Steel fiber reinforced concrete thin shell structure**
Oceanographic Park Restaurant. *City of Arts and Sciences*, Valencia (2002)
Based on blueprint of Felix Candela, by: A. Domingo, C. Lázaro, P. Serna